Stratification at Ocean Fronts

Leah Johnson

A dissertation

submitted in partial fulfillment of the

requirements for the degree of

Doctor of Philosophy

University of Washington

2018

Reading Committee:

Craig M. Lee, Chair

Eric A. D'Asaro

Leif N. Thomas

Program Authorized to Offer Degree:

Oceanography

University of Washington

Abstract

Stratification at Ocean Fronts

Leah Johnson

Chair of the Supervisory Committee:
Dr. Craig M. Lee
Oceanography

The large-scale changes of temperature and salinity in the ocean are not smooth and continuous, but comprise many smaller, sharper gradients. In regions of strong lateral density contrasts, sharp density fronts can slump, transforming potential energy into kinetic energy, and converting horizontal buoyancy gradients into vertical ones. The surface ocean is populated with such fronts, suggesting their cumulative impact is a leading order contribution to the upper ocean energy and buoyancy budgets.

Chapter 1 takes a global approach to assess the importance of frontal slumping on springtime restratification. Observations from the global Argo database are contrasted with predictions from a 1D mixed layer model to assess where lateral processes influence mixed layer evolution. Enhanced stratification from frontal tilting occur in regions of strong horizontal density gradients, with a small fraction in regions of deep mixed layers. These patterns are

discussed in the context of instabilities and frictional effects to understand the large-scale implications of these small-scale dynamics.

Chapters 2 and 3 focus on a highly detailed process study of one surface intensified submesoscale front. A Lagrangian float was deployed in a small mixed layer front within the California Current System as part of the Assessing the Effects of Submesoscale Ocean Parameterizations (AESOP) program. Its trajectory was tracked acoustically, allowing the region surrounding the drifting float to be surveyed intensely by a ship towing a Triaxus profiler. Initially, downfront winds incite mixing and the float repeatedly traverses the boundary layer. As winds relax and vigorous mixing subsides, the the system enters a different dynamical regime as the front develops an overturning circulation associated with large vertical velocities that ultimately tilt isopycnals over and stratify the upper ocean within a day. Chapter 2 details the observations and the kinematics of the system to reveal the importance of the submesoscale in transferring energy to smaller scales. Chapter 3 combines the observations with idealized models to evaluate the importance of wind forcing and turbulent adjustment on the evolution of stratification in the mixed layer.

TABLE OF CONTENTS

List of Figures iv

List of Tables x

1 Introduction 13

2 Chapter 1: Observational Evidence of Lateral Springtime Restratification 17

  2.1 Introduction 17

    2.1.1 Stratification by one-dimensional processes 20

    2.1.2 Stratification by lateral slumping 20

    2.1.3 Lateral slumping by mixed layer eddies 21

  2.2 Stratification: Model simulations vs. observations 24

    2.2.1 Data processing 24

    2.2.2 Case studies 27

    2.2.3 Global studies 28

  2.3 Signatures of isopycnal tilting 30

    2.3.1 Data analysis 30

    2.3.2 Case studies 31

    2.3.3 Global studies 31

  2.4 Stratification from MLEs 33

    2.4.1 Global pattern of Q_{MLE} vs. lateral slumping induced stratification 33

    2.4.2 Global distributions 36

    2.4.3 Horizontal buoyancy gradients vs. mixed layer depths 38

2.5 Regional studies 41
  2.5.1 Mid-latitude 41
  2.5.2 High latitudes 43
  2.5.3 Equatorial 44
2.6 Alternative hypotheses 44
  2.6.1 Wind dynamics 44
  2.6.2 Mesoscale dynamics 47
  2.6.3 Unresolved processes 48
2.7 Conclusions 50
3 Chapter 2: A Stratifying Submesoscale Front, Part I - Kinematics 52
3.1 Introduction 52
3.2 Data collection 53
3.3 Scale resolution 60
3.4 Frontal evolution 62
  3.4.1 Vertical shear and thermal wind (im)blanace 66
  3.4.2 Stratification 68
  3.4.3 Horizontal buoyancy gradient, strain, vorticity, and divergence 71
  3.4.4 Vertical velocity 75
  3.4.5 Potential vorticity 79
3.5 Buoyancy flux scalings 82
3.6 Conclusions 84
4 Chapter 3: A Stratifying Submesoscale Front, Part II - Dynamics 86

4.1 Introduction ... 86

4.2 Model set-up ... 87

4.3 1D: Surface buoyancy and momentum ... 88

4.4 2D: Friction, inertial motions, turbulent mixing ... 91

4.4.1 Compare 2D and 1D+ ... 93

4.4.2 Effects on stratification ... 100

4.4.3 Frontogenetic tendency ... 102

4.4.4 Potential vorticity ... 104

4.5 Along front variability ... 106

4.6 Vertical structure of stratification ... 109

4.7 Conclusion ... 111

5 CONCLUSIONS ... 113

Bibliography ... 116

LIST OF FIGURES

Fig. 1.1. Schematic of ocean processes in terms of length and temporal scales.............. 14

Fig. 1.2. Schematic of how slumping fronts convert horizontal stratification into vertical ones. 15

Fig. 2.1. (a) Schematic of a mixed layer density front during winter. Surface winds and deep convection keep the upper ocean vertically homogenous, yet lateral changes in bouyancy are retained. Horizontal changes in bouyancy comprise gradients of temperature and salinity (I) . (b) One-dimensional model. During spring, the upper ocean stratifies as a result of freshwater input and solar warming at the ocean surface. (c) Slumping model. Stratification at a front can occur without bouyancy input at the surface. As surface forcing weakens, the nearly vertical isopycnals in (a) begin to tilt as light water is advected over heavy water. In this scenario, the horizontal denisty gradient is being transformed into a vertical stratification. Horizontal temperature and salinity gradients become vertical gradients. Grey shaded areas in b,c represent the 50–90% depth range used in this analysis. (d) Gradients of TS provide insight into the mechanisms that stratify the upper ocean in the springtime transition. 18

Fig. 2.2. (a) Mean stratification at Ocean Weather Station Papa (48°–52°N, 213°–217°E) in 50–90% of the ML from model simulations (2006–2010) and float observations (2002–2013). Data were normalized to t_{QNET0} for each year, then 15-day means (lines) were plotted along with 2*stdev (shaded) for observations (green) and model (orange). Individual data points from obervations are plotted as dots (green). (b) Probability density function (PDF) of Turner angle at Ocean Weather Station Papa projected onto θ–S_A space. For each vector, the angle is determined using eq. 2.7 and eq. 2.8 for model (orange), observations (green), and horizontal density structure (purple). The length of each line is weighted to the magnitude of the PDF for the Turner angle. Here, observations match the 1D model as in Fig. 2.1b, d. (c) Same as (a) for the Icelandic Basin 58°–62°N, 336°–340°E. (d) Same as

(b) for the Icelandic Basin. Here, observations match the horizontal density gradient model as in Fig. 2.1c, d. 27

Fig. 2.3. (a) Ratio of observed stratification from Argo floats to modeled stratification using PWP (R_{N2}) for the month before t_{QNET}>0. (b) Error in R_{N2}. Contours of Q_{MLE} at 65 W m^{-2} (solid), 35 W m^{-2} (dashed), 20 W m^{-2} (dotted). 29

Fig. 2.4. (a) Δ Tu determined as | Tu_H–Tu_V| for the month before t_{QNET}>0. Tu_H is derived from MIMOC and Tu_V from Argo data using eq. 2.7 and eq. 2.8. (b) Error in Δ Tu. Contours of Q_{MLE} at 65 W m^{-2} (solid), 35 W m^{-2} (dashed), 20 W m^{-2} (dotted). Note the change in colorbar. In (a), orange represents low values to indicate observed Tu is similar to that of the horizontal gradient. In (b) the colorbar is inverted to highlight regions with large error. 32

Fig. 2.5. (a) Q_{MLE} (W m^{-2}) for the month before t_{QNET}>0 calculated from eq. 2.5 using MIMOC. Contours of Q_{MLE} at 65 W m^{-2} (solid), 35 W m^{-2} (dashed), 20 W m^{-2} (dotted). (b) Same as (a) for MIMOC MLD and (c) MIMOC derived ∇hb. Both MLD and ∇b have been binned and smoothed similar to Q_{MLE} (see section 2.4a). 34

Fig. 2.6. W_{NT} – *Weighted* R_{N2} * *Weighted* ΔTu. Higher values of W_{NT} are stronger signatures of increased R_{N2} and smaller values of ΔTu, both of which indicate lateral slumping induced stratification. Contours of Q_{MLE} at 65 Wm^{-2} (solid), 35 Wm^{-2} (dashed), 20 Wm^{-2} (dotted). Black boxes refer to the following observational studies. OWS Papa (145°W, 150°N); SPICE (140°W, 25°N; Ferrari and Rudnick 2000), LATMIX (65°W, 37°N; Shcherbina 2013), (150°W, 30°N; Hosegood 2006), NAB08 (20°W, 60°N; Mahadevan et al. 2012), OSMOSIS (48°N, 16°W), POMME (18°W, 42°N; Karleskind et al. 2011), SOSCEX (10°N, 42°S; Swart 2013). (b) Error in W_{NT}. 35

Fig. 2.7. PDFs of (a) ∇b, (b) mixed layer depth, (c) Q_{MLE}, (d) eddy kinetic energy, ... 37

Fig. 2.8. Latitudinal relationships between W_{NT} with R_{N2}, ΔTu, γ_W, and Q_{MLE}; Q_{MLE} with R_{N2} and ΔTu; ∇hb with MLD. Positive (negative) values suggest that the two variables are correlated (anti-correlated) within that latitude bin. Here, correlation coefficients between variables were computed in zonal sections of 5° latitude bins. Dotted lines represent 95% confidence intervals. 39

Fig. 2.9. PDF relating surface density gradients (∇b) and mixed layer depths (H). Contours are $QMLE \propto \nabla hb2H2f$ (eq. 2.3). (a) Northern Hemisphere (>10°N) summer (August). (b) Northern Hemisphere (>10°N) late winter (February), (c) Southern Hemisphere (>10°S) summer (February). (d) Southern Hemisphere (>10°S) late winter (August). The summertime relationship between ∇b and H suggests MLEs do not have a dominant role in setting upper ocean stratification. Wintertime H increases, but appears to be restrained by ∇hb. This restraint is shown as most regions of the worlds oceans are on a Q_{MLE} contour O(100 W m^{-2}), consistent with the significance of MLEs on the upper ocean......... 40

Fig. 2.10. (a) log(γ_W) negative values suggest that frontal processes dominate upper ocean stratification, while negative values suggest that wind processes are important. (b) Ekman buoyancy flux (EBF) in W m^{-2}. Positive values suggest that EBF is stratifying the upper ocean, while negative values indicate winds maintain the front working against MLEs. Contours of Q_{MLE} at 65 W m^{-2} (solid), 35 W m^{-2} (dashed), 20 W m^{-2} (dotted)......... 42

Fig. 2.11. Eddy kinetic energy EKE $(m/s)^2$ derived from AVISO geostrophic velocity anomalies. Contours of Q_{MLE} at 65 Wm^{-2} (solid), 35 Wm^{-2} (dashed), 20 Wm^{-2} (dotted)............ 48

Fig. 2.12. Observed Turner angle is compared with modeled vertical and horizontal Turner angles (see Fig. 2.1). Descriptions of each of these categories is summarized in (b), where agreement is set at a threshold of ΔTu<30. (A) ΔTu_{OM}<30, (B) ΔTu<30, ... 49

Fig. 3.1. a) Detail of sea surface temperature (SST) and mesoscale survey (white). Lagrangian float track (black dots) and ship track colored with ship underway temperature. b) SST off the California Coast on 4 August 2006 from the Group for High Resolution SST (GHRSST - https://podaac.jpl.nasa.gov). Contours are AVISO mean sea level anomaly. White dots outline the mesoscale survey ship track. Block dots outline the Lagrangian survey ship track. Both tracks are during the restratifying phase. 54

Fig. 3.2. a) Example of loops from underway data. A plane is fit to each loop, e.g. n–1, n, and n+1. Results from each loop are averaged together to form a single value for n. b) Example plane fit. 57

Fig. 3.3. Lagrangian analysis at depth. x distance is the cross frontal distance in the reference frame of the float trajectory toward the end of the survey (i.e., after the turn). Dashed line is the ship track, where each zigzag in time represents one loop. Colored lines are dxf

integrated with shear from Triaxus. At yd=216.7 dxf implies that flow at 20 m is no longer true to the Lagrangian reference set at the beginning of the survey. 59

Fig. 3.4. Objective maps of near surface σ for mesoscale survey (16 m, background), and Lagrangian survey (4 m, foreground). Contours outline isopycnals every 0.1 kg m^{-3}. Grey dots track the float location. x-axis and y-axis are distance in km. 61

Fig. 3.5. Initial transect used to identity the front before placement of the float. Top: cross frontal σ [kg m^{-3}] from the ship flow through system. Bottom, cross frontal σ [kg m^{-3}] from Triaxus. Black lines are contours of σ= 0.1 kg m^{-3} and the dark black line is $\sigma = 24.4$ kg m^{-3}. 63

Fig. 3.6. – Scalars and velocity of the front underneath the float throughout the Lagrangian survey. a) σ and float depth (grey dots); b) N^2; c) along front wind stress (green) and across front wind stress (purple), Q_{NET} (grey); d) salinity; e) u velocity; f) shear u_z; g) temperature; h) v velocity; and i) shear v_z. Dashed grey lines denote the three stages outlined in section 3.4... 65

Fig. 3.7. Raw Triaxus data salinity during a) stage 1, yd 216.1 and b) stage 3, yd 216.8. Black dashed lines are 0.1 σ contours and solid line marks the 24.3-kg m^{-3} contour. Circles denote the position of the float within $\pm$15 min of the transect and are colored in average salinity of the float sensors. 66

Fig. 3.8. Geostrophic shear, ageostrophic shear, and total shear for a) u_{af} at 8 m, b) u_{xf} at 8 m, c) u_{af} at 16 m, d) u_{xf} at 16 m. All terms have been rotated to align with ∇b at 4 m (section 3.2). Shaded regions are error (ϵ)... 67

Fig. 3.9. Objective map of σ at 4 m. Map has been rotated to follow the float trajectory (blue dots) during stages 2 and 3. The grey scale lines denote the 24.4 contour at different depths. 69

Fig. 3.10. From top to bottom: a) N^2, b) ΔT, c) ΔS at 8 m. Black lines are observations, purple lines are integrated values from eq. 3.4. Blue dashed lines are the difference between the observations and integrated values. Purple line in a) is N^2 from eq. 3.5 using $\partial Th \partial z$ and $\partial Sh \partial z$. Green line in b) is $\partial Th \partial z$. Scaled float depth is included in a) for reference. Shaded regions are error (ϵ). 71

Fig. 3.11. (a) δ/f, (b) α/f, (c) ζ/f , and (d) ∇hb plotted against time at depths 8–20 m. Float depth scaled by x10^{-3}. (b) Included to provide reference for frontal evolution. Shaded regions are error (ϵ). 72

Fig. 3.12. a) ∇bs calculated along track from the ship underway. b) example of a cross front transect of σ resolved by the underway (purple) and Triaxus at 4 m (blue)............ 73

Fig. 3.13. Frontogenetic tendency as a function of time F at z = 8. Shaded regions are error (ϵ). 75

Fig. 3.14. a) Circles denote float location and are color coded in salinity. Arrows at surface are float velocity vectors. Each float location and velocity vector is connected by a thin grey line. b) vertical velocity estimated directly from float (purple) and from Triaxus (green). 76

Fig. 3.15. a) Cross frontal distance of float as it downwelled under the front during I–IV. b) TS diagram during downwelling events III. Float and Triaxus represent the TS of the vertical stratification, while the ship underway provides TS of the horizontal stratification. 77

Fig. 3.16. Potential vorticity (black line) and its components (vertical – blue, horizontal – red) for a) 4 m and b)16 m. Both plots also include planetary PV (purple) and thermal wind balance (black dashed lines). Shaded regions are error (ϵ)... 80

Fig. 3.17 $w'b'$ scalings estimated from observationally derived parameters.................. 83

Fig. 4.1. a) 1DPWP N^2. Grey dots are PWP ML. b) 2D N^2. Grey dots are KPP boundary layer depth. c) OBS N^2. Grey dots are float depth. d) 1DPWP U, e) 2D U, f) OBS U, g) 1DPWP U_z, h) 2D U^z, i) OBS U_z, j) Q_{NET}, k) along front wind stress (grey) and cross front wind stress (black), l) KPP viscosity κv. Dashed lines in a, b, c, j, k, and l separate the three stages.. 89

Fig. 4.2. Vertical gradients of b (a), T (b), and S (c) calculated from 1DPWP (purple), the float (blue), and Triaxus at 4 m (orange) and 12 m (yellow)... 90

Fig. 4.3. a) Along front (blue) and cross front (purple) winds stress. b) Plan view Hovmöller plot of surface ρ in 2D, grey lines are isopycnals, black dots are cross front distance of the float trajectory overlay for reference. c-e) Velocity components for 2D, solution to eq. 4.1, eq. 4.22, and OBS. 91

Fig. 4.4. Cross front density structure in ship underway (red) during the initial frontal transect, and in 2D (black) at yd 217. Density from ship underway during the first 4 hr of the survey (grey). 92

Fig. 4.5. (a–d) Cross front u_z. (e-h) Along front u_z. (a, e) 2D, (b, f) 1DCN, (c, g) IDCN with no κv, (d, h) IDCN with no Y_i. Grey lines denote float location in OBS for reference. 96

Fig. 4.6. (a) IDCN u_z initialized with OBS, (b) IDCN v_z initialized with OBS, (c) u_z from OBS, and (d) v_z from OBS 97

Fig. 4.7. (a) u_z. (b) v_z, rotated such that along front shear is positive (i.e., $-v_z$ in OBS). Each plot includes shear from 2D (grey), 2D ADV (red), 2D DIFF (teal), 1DCN (purple), and OBS (orange). 98

Fig. 4.8. Hodographs of shear at (a) 15–25 m, and (b) 40–50 m. 2D (purple), 1DCN$_{2D}$ (blue), OBS (orange), and 1DCN$_{OBS}$ (green). Shading represents time, beginning at onset of stage 2 (light shade) until the end of stage 3 (dark shade). Black borders represent time that float subducts in OBS. 100

Fig. 4.9. N^2 normalized to Ri_B. N^2 for the OBS (dark green). $NINT2$ in 2D (dark purple), and for the IDCN solutions to the OBS (light green) and 2D (light purple). Solutions to ADJ (orange) and TTW (yellow). 101

Fig. 4.10. Frontogenetic tendency terms calculated from the OBS (Ch. 3.), 2D F_{sa} (purple) and F_{kv} (yellow), and for 1DCN$_{2D}$ (blue) 103

Fig. 4.11. PV and its components from 2D at 4 m (a) and 16 m(b). q_V (red), q_H (blue), and q (black). N^2_{INT} is used to estimate the advective contribution to q_V (red dash) and q_H (black dash). Thermal wind balance, M^4f^{-2}, (small black dash) and float depth (scaled x10^{-9}) are added for reference. 105

Fig. 4.12. Top: N^2 from OBS. Bottom: N^2 from eq. 4.20 108

Fig. 4.13. Ri_b for OBS (a) and 2D (b). 109

Fig. 4.14 Vertical structure of N^2 in terms of Ri_b. 110

LIST OF TABLES

Table 3.1. Values for scalars, velocities, and their gradients resolved at different observational scales 60

Table 3.2. Description of processes that may influence stratification at a front.............. 82

ACKNOWLEDGMENTS

This work would not be possible without the funding provided by ONR Grants N00014-15-1-2296, N00014-13-1-0478, N00014-16-1-3131, N00014-09-1-0266, N00014-10-1-0308, N00014-10-1-0311, and NSF Grants PLR-1022472, OCE-0628379. I wish to also acknowledge the tremendous support of the University of Washington graduate community, providing stimulating conversation and enthusiastic company throughout the years.

DEDICATION

This work is dedicated to those who inspire me most, Jake Mann and Sarah Johnson.

1 INTRODUCTION

The large-scale circulation of the ocean is driven by buoyancy flows set by the input of heat and freshwater and momentum input from atmospheric wind patterns. Together, this sets the basin wide structure of density and currents, which are the largest reservoir of potential energy in the oceans. These mean currents undergo instabilities to create a vigorous mesoscale O(100 km) eddy field that contains 90% of the kinetic energy of the oceans (Ferrari and Wunsch 2009). The advective timescales of largescale and mesoscale flows implies their dynamics are constrained by the Earth's rotation (i.e., Rossby number (Ro) = $Uf/L \ll 1$), where U and L are characteristic advective and length scales and f is the Coriolis parameter. As such, these currents and eddies tend to be in thermal wind balance and can be examined analytically in the 2D, non-divergent framework of Geostrophic Turbulence (QG; Charney 1971) governed by interior potential vorticity (PV) dynamics. This framework experiences an inverse cascade of energy back into large scales through eddy–eddy interaction, pivoting at about 100 km. It follows that there would be a significant decrease in vorticity, kinetic energy, and vertical velocity at smaller scales. Therefore, classical QG falls short at describing a rich abundance of submesoscale O(1 km) features found to be ubiquitous in the upper ocean (Rudnick and Ferrari 1999; Hosegood et al. 2006; Mahadevan et al. 2012; Thompson et al. 2016).

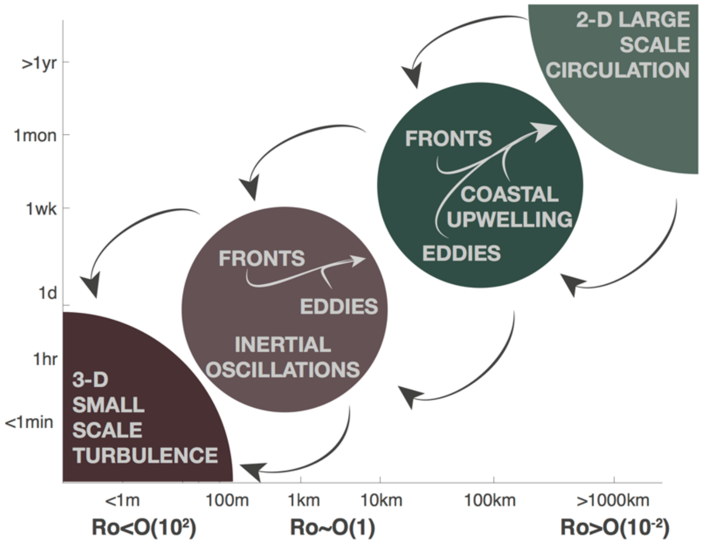

Fig. 1.1. Schematic of ocean processes in terms of length and temporal scales.

The existence of submesoscales is more accurately represented by a surface quasigeostrophy (sQG) framework set by the buoyancy structure at the surface instead of interior PV (Lapeyre and Klein 2006). This allows gradients near the surface to be stirred by the energetic geostrophic field into sharp fronts and filaments that evolve on a timescale of days. While it is convenient to categorize submesoscales in terms of a length scale, a more dynamical designation can be recognized in both their fast advective timescale and their near surface environment. The near surface intensification of these features suggests they are exposed to high vertical and lateral shear with *Ro* (defined here as $\frac{\zeta}{f}$) (O(1)), weak stratification (i.e., Richardson number (*Ri*) $\frac{N^2}{{U_z}^2} = 1$) and diabatic and frictional forcing. This parameter space hosts a range of dynamics that interact with the front to further transfer energy and tracers to smaller scales in route to dissipation (Fig. 1.1). A suite of processes (Thomas et al. 2008; McWilliams 2016) may occur at ML fronts. In particular, this dissertation will focus on processes that decrease the available potential energy (APE) stored in a front by turning horizontal stratification into a vertical one (Fig. 1.2).

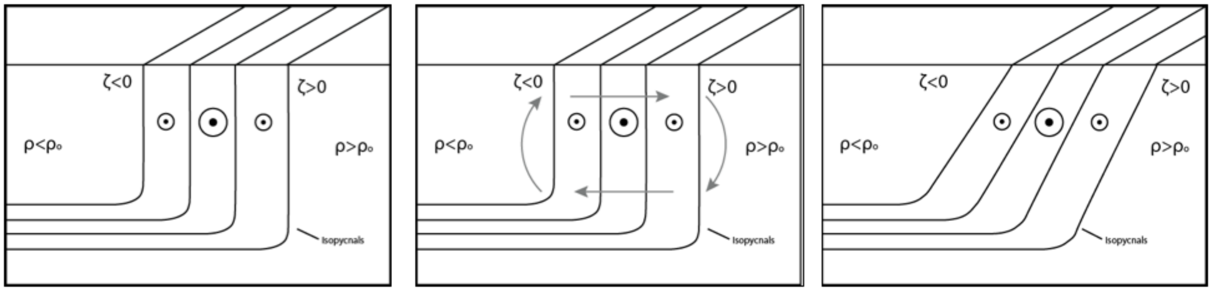

Fig. 1.2. Schematic of how slumping fronts convert horizontal stratification into vertical ones.

The evolution of stratification in the upper ocean has been a keystone in oceanography as it regulates the depth of the well-mixed surface layer with direct implications for air-sea heat and gas exchange, ocean biogeochemistry, and general ocean circulation (Belcher et al. 2012; Sverdrup 1953; Worthington 1958). Traditionally, stratification of the surface ocean can be represented as top down effects of buoyancy input from solar warming and freshwater that act to increase stratification, and mixing from convective overturning and wind that can erode it (Kraus and Turner 1967; Price et al. 1986; Large et al. 1994), a view that neglects lateral processes that advect buoyancy and alter the stratification of the upper ocean. This traditional '1D' assumption is appropriate when considering the insignificant lateral effects of slow, large-scale currents that do not advect buoyancy fast enough to compete with surface inputs of momentum and buoyancy at the surface. This dissertation reinforces the failure of this assumption in the presence of strong lateral density fronts as dynamics and flows slump isopycnals and transform horizontal changes in buoyancy into vertical ones on a timescale that competes with surface forcing. Chapter 1 takes a global approach to assess the importance of frontal slumping on springtime restratification (Johnson et. al. 2016). Chapters 2 and 3 focus on a highly detailed process study of one surface intensified submesoscale front. Chapter 2 details the observations and the kinematics of the system to reveal the importance of the submesoscale in transferring energy to smaller scales. Chapter 3 combines the observations with idealized models to evaluate the importance of wind forcing and turbulent adjustment on the evolution of stratification in the mixed layer.

2 CHAPTER 1: OBSERVATIONAL EVIDENCE OF LATERAL SPRINGTIME RESTRATIFICATION

2.1 INTRODUCTION

The mixed layer (ML) of the upper ocean evolves in response to momentum input from winds and buoyancy fluxes (e.g., surface heat flux, inputs of fresh water and salt). Wintertime cooling and strong winds at the ocean surface drive convective overturning and mixing that homogenize the upper ocean, producing deep MLs. During the transition into spring, warmer, more buoyant waters cap the underlying wintertime ML, inhibiting deep mixing and stratifying the upper ocean. This springtime stratification has large impacts on upper ocean biogeochemistry (Sverdrup 1953), air–sea heat and gas exchange (Belcher et al. 2012), and water mass formation (Worthington 1958). One-dimensional dynamics describe springtime mixed-layer evolution as a competition between deepening by convective overturning and wind-mixing, and shoaling due to buoyancy input from increased solar warming (Fig. 2.1). The ML shallows as increasing net surface heat flux overcomes mixing and convection. This one-dimensional view, however, neglects lateral processes that can advect buoyancy and alter the stratification of the upper ocean.

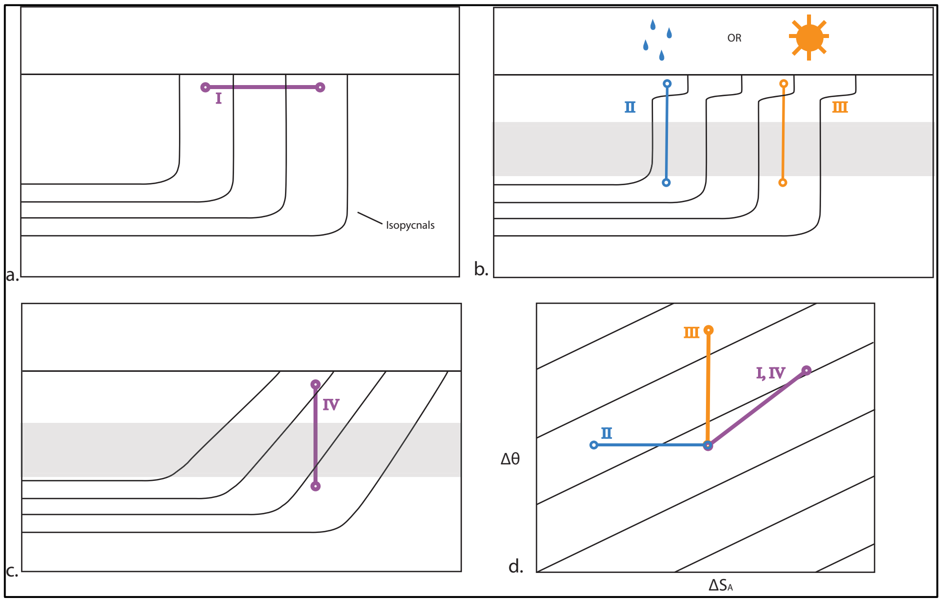

Fig. 2.1. (a) Schematic of a mixed layer density front during winter. Surface winds and deep convection keep the upper ocean vertically homogenous, yet lateral changes in bouyancy are retained. Horizontal changes in bouyancy comprise gradients of temperature and salinity (I) . (b) One-dimensional model. During spring, the upper ocean stratifies as a result of freshwater input and solar warming at the ocean surface. (c) Slumping model. Stratification at a front can occur without bouyancy input at the surface. As surface forcing weakens, the nearly vertical isopycnals in (a) begin to tilt as light water is advected over heavy water. In this scenario, the horizontal denisty gradient is being transformed into a vertical stratification. Horizontal temperature and salinity gradients become vertical gradients. Grey shaded areas in b,c represent the 50–90% depth range used in this analysis. (d) Gradients of TS provide insight into the mechanisms that stratify the upper ocean in the springtime transition.

Large-scale lateral density gradients within the ML are the net product of numerous, smaller, sharper gradients and fronts. Consider just one of these sharp fronts (Fig. 2.1); the upper ML is vertically homogenous, but the lateral structure reveals a sharp density difference. Slumping this small front transforms the horizontal density gradient into a vertical stratification (Fig. 2.1). This transformation rearranges the lateral density structure, suggesting that initial temperature–salinity (TS) horizontal gradients eventually constitute the vertical stratification. One small front stratifies the upper ocean locally, and a field of tilting fronts creates a large-scale stratification.

Recent work suggests that dynamics associated with submesoscale O(10–100 km) fronts are a leading order contributor of upper ocean stratification in the absence of solar warming. (Boccaletti et al. 2007; Thomas et al. 2008). During wintertime, surface cooling and wind-driven turbulent mixing act to keep the upper ocean vertically homogenous in the presence of sharp horizontal density contrasts (e.g., Fig. 2.1). These sharp gradients provide a source of available potential energy (APE). Dynamics that tap into this APE can result in baroclinic instabilities that grow into submesoscale eddies (ML eddies or MLEs). (Boccaletti et al. 2007) The flattening of isopycnals by MLEs is inhibited by wintertime wind mixing and cooling that work to maintain the vertical homogeneity of the ML. But theory and model simulations predict that frontal slumping has an important role in spring, when forcing by winds and surface cooling weaken, but before net solar warming dominates the vertical buoyancy of the upper ocean. MLEs could explain why one-dimensional mixed layer models fail to describe springtime upper ocean restratification accurately. (Boccaletti et al. 2007; Thomas and Ferrari 2008; Mahadevan et al. 2012).

This paper focuses on MLEs as the source of springtime restratification, yet there are other leading order frontal processes that modify stratification in the ML. In the absence of forcing, vertical isopycnals of a front will undergo geostrophic adjustment and tilt to a resting state as described by (Tandon and Garrett 1994). Frontogenetic flows induce ageostrophic secondary circulations that flatten isopycnals (Hoskins and Bretherton 1972). Additionally, frictional effects are shown to be as influential as MLEs at modulating ML stratification. Winds blowing up/down front have restratifying/destratifying effects on the upper ocean (Thomas and Lee 2005; Mahadevan et al. 2010).

This work takes a global approach to investigate the following: Why do one-dimensional mixed layer models fail to replicate ML evolution during the transition from winter to spring (2.2)? Can the observed stratification in excess of model predictions be attributed to lateral slumping of submesoscale fronts (section 2.3)? Does MLE theory explain patterns of stratification induced by lateral slumping (section 2.4)? After a regional discussion of the global results (2.5), alternate frontal processes that modify ML stratification are explored (section 2.6).

2.1.1 *Stratification by one-dimensional processes*

ML evolution has been described successfully using one-dimensional dynamics (Kraus and Turner 1967; Price et al. 1986; Large et al. 1994), balancing deepening by wind-mixing and convective overturning against shallowing by surface warming and surface freshwater input. Global simulations that use these parameterizations overestimate ML depth (Fox-Kemper et al. 2011). This study employs a one-dimensional model (Price, Weller and Pinkel 1986; PWP) to simulate upper ocean response to surface heat flux, winds stress, and freshwater input. Modeled vertical structure is compared with upper ocean observations collected by the global ARGO program (Roemmich et al. 2004) to assess where the spring transition cannot be explained by one-dimensional processes and pinpoint regions where lateral processes are likely influential. 2.2.1 provides details about the 1D model and data processing.

2.1.2 *Stratification by lateral slumping*

Adiabatic slumping of a front ultimately results in an upward transport of buoyancy as the lateral density gradients (e.g., Fig. 2.1b) are transformed into a vertical stratification (e.g., Fig. 1.1c). The rearrangements of isopycnals implies that lateral gradients of TS are rotated into vertical gradients. This relationship between vertical and horizontal TS will be used to isolate regions where adiabatic frontal tilting could account for the shortfall of PWP model simulations compared to Argo float observations and is discussed in 2.3.

2.1.3 *Lateral slumping by mixed layer eddies*

Boccaletti et al. (2007) and Fox-Kemper et al. (2008) propose that lateral slumping, and the resulting stratification of the ML, occurs via MLEs. As wintertime forcing weakens, vertical isopycnals begin to undergo adjustment. Direct slumping due to geostrophic adjustment results in a modest increase in ML stratification as isopycnals oscillate around a mean state (Tandon and Garrett 1994). However, at submesoscale fronts, the Rossby number approaches O(1) and geostrophy breaks down, allowing these oscillations (or other perturbations) to grow into baroclinic instabilities that develop MLEs (Boccaletti et al. 2007). These submesoscale instabilities draw upon the APE of the lateral density gradients, resulting in an eddy overturning circulation with large vertical velocities that redistribute density and flatten the initially nearly vertical isopycnals (Boccaletti et al. 2007; Fox-Kemper et al. 2008). The existence of submesoscale fronts during winter suggests that fields of MLEs could have an impact on large-scale stratification that is not captured by one-dimensional parameterizations of the upper ocean. Upper ocean buoyancy transport by the MLE overturning circulation competes with convection and wind mixing that act to destroy vertical stratification (Mahadevan et al. 2010).

Fox-Kemper et al. (2008) propose a parameterization for the slumping of a single submesoscale front into vertical stratification by a MLE. The overturning streamfunction is

$$\Psi_o = C_e \frac{\nabla_h b H^2 \times \boldsymbol{z}}{|f|} \mu(z) \,, \tag{2.1}$$

$$\mu(z) = \left[1 - \left(\frac{2z}{H} + 1\right)^2\right]\left[1 + \frac{5}{21}\left(\frac{2z}{H} + 1\right)^2\right], \tag{2.2}$$

where $b = -g\,\frac{\rho}{\rho_o}$ is buoyancy, H is ML depth, f is the Coriolis parameter, and C_e is 0.06–0.08.

The net effect is the transformation of horizontal density gradients into vertical stratification by an MLE; this process is potentially important for the ML buoyancy budget. Although MLEs are not a source of buoyancy, it is possible to express the overturning streamfunction Ψ_o in terms of an equivalent surface heat flux (Fox-Kemper and Ferrari 2008; Mahadevan et al. 2012)

$$Q_{MLE} = \frac{c_p \rho}{g \alpha_T} \frac{\mathrm{C}_e\, |\nabla_h b|^2 H^2}{|f|}, \tag{2.3}$$

where c_p is the specific heat capacity of water, and α_T is the thermal expansion coefficient.

Here, the stratifying effect of an MLE is stated as a surface heat flux equivalent, Q_{MLE}. This facilitates comparison with air–sea heat fluxes and formulates the impact of this three-dimensional process in a one-dimensional framework.

This parameterization (eq. 2.1) is designed for a single, resolved submesoscale front and is thus insufficient for larger-scale models. The resolution of global simulations (O(100 km)) cannot resolve the submesoscale lateral density gradients (O(1–10 km)). Modeled gradients (and observed large-scale gradients) must thus be scaled appropriately for use in the Fox-Kemper parameterization (eq. 2.1). Observational studies show that power spectra fall off at about k^{-2} for horizontal variance of velocity and tracers (Capet et al. 2008a) and potential density. Fox-Kemper et al. (2011) assume this and derived a relationship between large-scale density structure and small-scale gradients. This relationship extends the utility of (eq. 2.1) to coarser-scale models through a scale factor $\Delta s/L_f$(Fox-Kemper et al. 2011), where Δ is the grid resolution and

L_f is a typical width of a submesoscale front taken to be the maximum of three possible estimates:

$$L_f = max(\frac{NH}{|f|}, \frac{\nabla_h bH}{f^2}, L_{fmin}). \tag{2.4}$$

The first suggests that frontal width scales as the ML deformation radius (Hosegood et al. 2006). The second assumes that stratification in the ML before a MLE is a result of Rossby adjustment, which scales as $N^2f^2=\nabla_h b^2$ (Tandon and Garrett 1994). The third L_{fmin} is a tuned parameter for frontal width approximated to be 0.2–5 km (Fox-Kemper et al. 2011).

In global simulations, the scaling factor is applied to the overturning streamfunction (eq. 2.1) such that $\Psi = \frac{\Delta s}{L_f}\Psi_o$. Similarly, it is applied to eq. 2.3:

$$Q_{MLE} = \frac{\Delta s}{L_f} \cdot \left[\frac{c_p \rho}{g \alpha_T} \frac{C_e\, |\nabla_h b|^2 H^2}{|f|}\right], \tag{2.5}$$

Q_{MLE} represents the restratifying effects of MLEs and suggests MLEs will dominate upper ocean stratification when Q_{MLE} is comparable in magnitude to the destratifying effects of negative surface heat flux and wind mixing. This implies that observations in regions with MLEs would experience earlier onset of stratification than predicted by one-dimensional processes (Mahadevan et al. 2012). In this study, Q_{MLE} is used to explore where regions of lateral slumping can be attributed to MLEs.

Parameterizations of MLE-induced stratification have been integrated into global circulation models (GCM) on top of current one-dimensional ML parameterizations, e.g., CCSM4 (Danabasoglu et al. 2012) and ESM2 (Dunne et al. 2012), yet no observational study has assessed whether this parameterization is appropriate throughout the world's oceans. Mahadevan et al. (2012) use data and model simulations to show that increased ML stratification in the Icelandic Basin (IB) could be attributed to the influence of MLEs. Increased stratification was observed by autonomous gliders and is evident in climatological data from the region. The climatological signature of enhanced stratification, combined with the theoretical development of the MLE parameterization for GCMs, provide a large-scale fingerprint of the integrated effects of this small-scale process that could be observed on a global scale.

Here, global observations of vertical stratification and ML TS are used to identify regions of enhanced stratification produced by lateral slumping of horizontal density gradients. Results are compared with global maps of Q_{MLE} to assess where MLE theory can predict these patterns of observed stratification induced by lateral slumping. Similarities and discrepancies between these two distributions will be discussed in the context of other important ML processes.

2.2 STRATIFICATION: MODEL SIMULATIONS VS. OBSERVATIONS

2.2.1 *Data processing*

The one-dimensional PWP model (Price et al. 1986) predicts the time evolution of the vertical structure of temperature and salinity in the upper ocean. The model is forced with radiative (shortwave, longwave, latent and sensible heat) and freshwater fluxes from the National Centers for Environmental Prediction – National Center for Atmospheric Research reanalysis 2 (NNR2) and winds from the Cross Calibrated Multi Platform (CCMP). Model runs are initialized with a single profile of in situ temperature and salinity calculated from conservative temperature (θ) and absolute salinity (S_A) provided by the Monthly Isopycnal/Mixed-Layer Ocean Climatology (MIMOC; Schmidtko et al. 2012). Each model run starts in winter, when ML depths are assumed to be deepening (January 1st for the Northern Hemisphere, July 1st in the Southern Hemisphere). The model is then run for 250 days with 2-m vertical resolution and 6-h temporal resolution. Runs are performed throughout the global oceans at locations defined by NNR2 and initialized for five separate years between 2006 and 2010. This study also employs Argo float profiles from the program's global database (Roemmich et al. 2004) collected between 2002 and 2013 with a quality control flag of 2 or better. Hereinafter, analysis is conducted in terms of conservative temperature (θ) and absolute salinity (S_A) (Thermodynamic Equation of Seawater 2010).

This analysis focuses on the ML evolution from winter to spring, during the period before the ocean experiences significant surface heating, when lateral processes are theorized to have a large role in governing upper ocean stratification on timescales of days. Throughout, time is expressed relative to the day on which total radiative heat flux (Q_{NET}) changes sign from surface cooling (negative) to surface warming (positive), (t_{QNET0}). This allows all years of model output and observations to be collapsed onto a single time axis. Quantifying t_{QNET0} is complicated by fluctuations in radiative heat fluxes; sign change can be obscured by intermittent warming followed a period of cooling. Here, t_{QNET0} for each year is determined by identifying the minimum of the zero,phase, low-pass (length of 20 days) filtered, time-integrated Q_{NET} derived from NNR2. Both the integration and low-pass filter act to smooth the data. A 20-day filter was determined through visual inspection to be the most appropriate length to capture the minimum integrated Q_{NET}. A Monte Carlo error estimate for t_{QNET0} combines uncertainties in radiative heat flux provided by NNR2 with a range of low-pass filter lengths (7–30 days). Regions most sensitive to this calculation are the lower latitudes (<20 degrees) with a standard deviation of 5 days; standard deviation decreases to 3 days at higher latitudes. This range of error is propagated as background noise when calculating error in subsequent analyses (2.2.3 and 2.3.3). Regions lacking a minimum in integrated Q_{NET} (e.g., near the equator) were omitted from analysis.

Although spring stratification results in ML shoaling, defining the ML can be challenging, because small variations in ML definition can produce results that differ greatly (e.g., Sutherland et al. 2014). This study avoids this obfuscation by focusing on stratification in the upper ocean (Brunt–Väisälä frequency; $N^2 = -\frac{g}{\rho_o}\frac{\Delta\rho}{\Delta z}$). Differences between observed and modeled N^2 are used to identify regions where lateral processes may be important in the upper ocean buoyancy budget. Model simulations of MLEs show the majority of stratification occurs in the middle of the ML (Mahadevan et al. 2010; Thomas and Ferrari 2008), as has been confirmed in observations (Mahadevan et al. 2012). Here, the aim is to capture the evolution of stratification in the vertically homogenized wintertime upper ocean during the transition into spring. Choosing a depth range of focus is region specific, with a lower bound above the pycnocline and the upper limit sufficiently below the surface to minimize small diurnal fluctuations due to heat and wind. Therefore, N^2 values from model output and observations are calculated vertically using changes in density over a depth range defined by 50–90% of the MIMOC ML for the month before $t_{\_QNET0}$. Upper boundaries are capped at 10 m, which encompasses ~25% of the regions analyzed. The lower boundary accounts for uncertainties in the climatologically smoothed ML depth and provides a buffer from the stratified pycnocline. Argo quality control precision thresholds for temperature and salinity are used in a Monte Carlo error estimate, resulting in N^2 std $O(10^{-7}\ s^{-1})$. Salinity measurements from Argo profiling floats have an accuracy of 0.001 psu, therefore both modeled and observed profiles with a change in S_A less than 0.001 psu between the top and bottom bounds of the 50–90% ML depth range were excluded from subsequent analysis. Imposing this salinity threshold excludes profiles with very small values of N^2 and therefore limits the analysis to regions that exhibit stratification > $O(10^{-7}\ s^{-2})$, approximately the magnitude of error expected from Argo profile data.

2.2.2 *Case studies*

Previous studies used one-dimensional mixed layer parameterizations to describe ML evolution near Ocean Weather Station Papa (OWS-P; Gill and Niller 1973; Large et al. 1994; Emerson and Stump 2010). There is good agreement between OWS-P mean observed (2002–2013) and modeled (2006–2010) lower ML N^2 as a function of t_$_{\mathrm{QNET0}}$ (Fig. 2.2a), suggesting that one-dimensional dynamics are sufficient to describe the evolution of upper ocean stratification during the transition to spring, including the period prior to the onset of net surface warming.

In the wintertime IB, however, modeled N^2 underestimates consistently the observed N^2 (Fig. 2.2b), supporting the hypothesis that MLEs generate sporadic stratification throughout winter. Additionally, the observed N^2 increase before t_$_{\mathrm{QNET0}}$, consistent with the results reported by (Mahadevan et al. 2012).

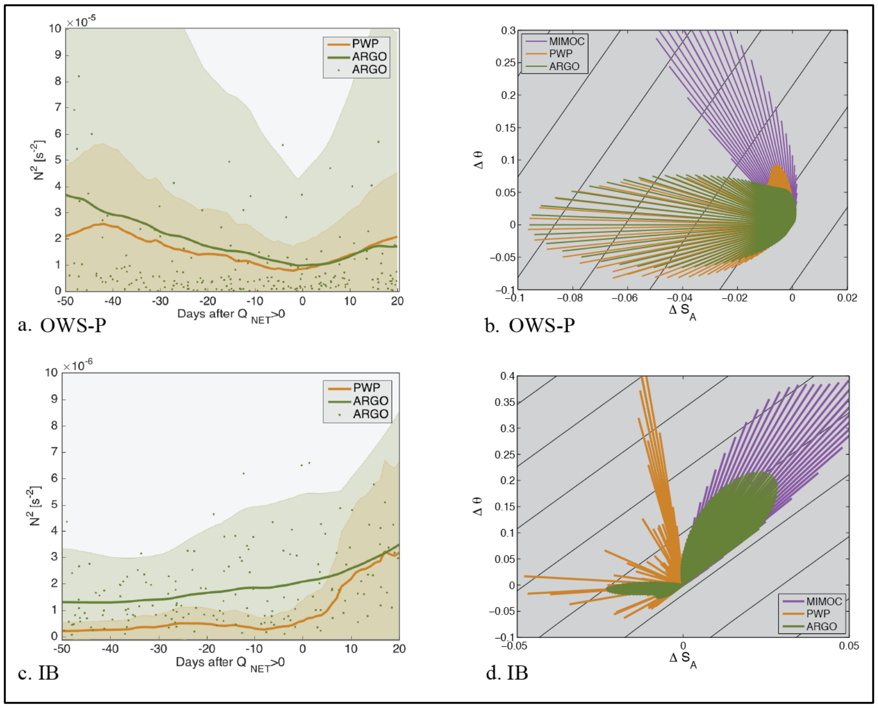

a. OWS-P

b. OWS-P

c. IB

d. IB

Fig. 2.2. (a) Mean stratification at Ocean Weather Station Papa (48°–52°N, 213°–217°E) in 50–90% of the ML from model simulations (2006–2010) and float observations (2002–2013). Data

were normalized to t_{QNET0} for each year, then 15-day means (lines) were plotted along with 2*stdev (shaded) for observations (green) and model (orange). Individual data points from obervations are plotted as dots (green). (b) Probability density function (PDF) of Turner angle at Ocean Weather Station Papa projected onto θ–S_A space. For each vector, the angle is determined using eq. 2.7 and eq. 2.8 for model (orange), observations (green), and horizontal density structure (purple). The length of each line is weighted to the magnitude of the PDF for the Turner angle. Here, observations match the 1D model as in Fig. 2.1b, d. (c) Same as (a) for the Icelandic Basin 58°–62°N, 336°–340°E. (d) Same as (b) for the Icelandic Basin. Here, observations match the horizontal density gradient model as in Fig. 2.1c, d.

2.2.3 *Global studies*

An analysis of the world's ocean follows a similar approach. Observed and modeled vertical profile data are binned spatially at 2 x 2 NNR2 data points, yielding grid resolution of 3.75° longitude and 3.78–3.81° latitude. Within each bin, depth averaged N^2 for 40–10 days before t_{QNET0} (total of 30 days) are used to create a non-parameterized probability density function (i.e., kernel distribution, PDF) that provides the mode of the N^2 distribution. The 10-day shift away from $t_{QNET0} = 0$ accounts for uncertainties in t_{QNET0} to ensure that the one-month window excludes the period after the net surface heat flux changes to warming. The mode provides a more robust representation of the stratification in a given region by minimizing the influence of spurious events and, in general, results in lower values of observed N^2 than mean or median based calculations. Regions where less than 10 ARGO profiles were available for the PDF were omitted from this analysis. Modeled and observed stratification are compared as a ratio of the two mode values (R_{N2}):

$$R_{N2} = \frac{N^2_{obs}}{N^2_{mod}} \tag{2.6}$$

where an $R_{N2} > 1$ implies a larger observed stratification than what is predicted by the 1D model.

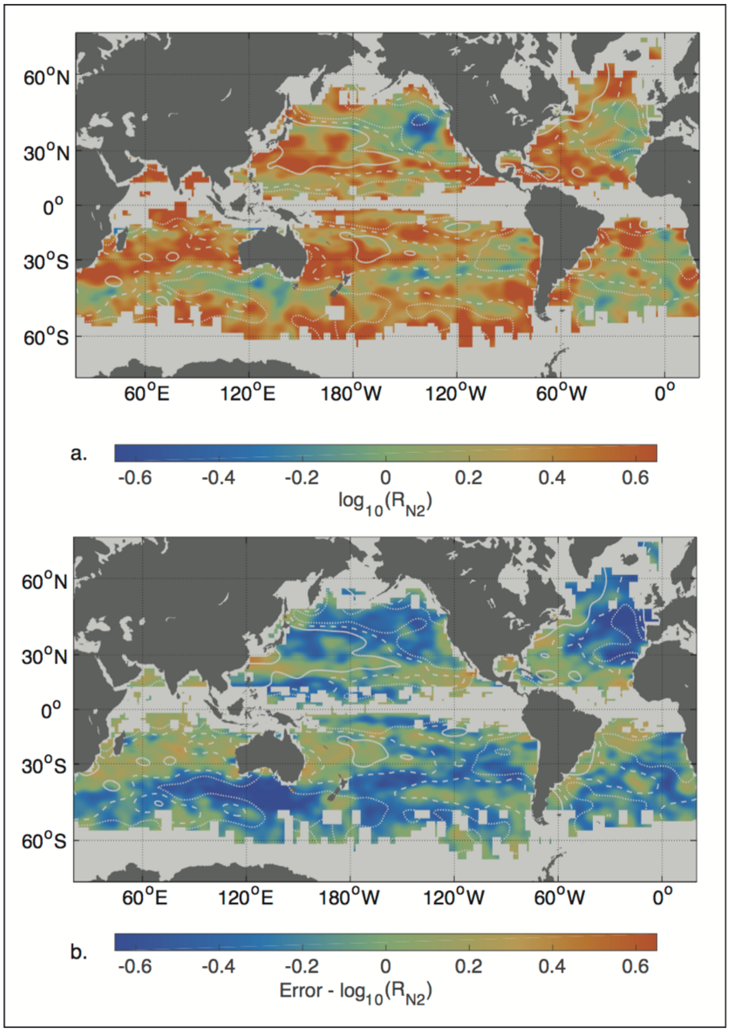

Fig. 2.3. (a) Ratio of observed stratification from Argo floats to modeled stratification using PWP (R_{N2}) for the month before t_{QNET}>0. (b) Error in R_{N2}. Contours of Q_{MLE} at 65 W m^{-2} (solid), 35 W m^{-2} (dashed), 20 W m^{-2} (dotted).

Global maps of R_{N2} identify regions where springtime stratification exceeds that predicted by the 1D model (Fig. 2.3a, orange highlights). R_{N2} error is estimated using a Monte Carlo approach, adding noise to t_{QNET0}, θ, and S_A for repeated calculations of mode N^2 (Fig. 2.3b). Following

Hosegood et al. (2006) the increase in stratification due to lateral slumping in relation to that expected from one-dimensional dynamics is $R_{N2} \approx 1.5$. Adopting this as a threshold yields an estimate that one-dimensional dynamics fail to reproduce observed springtime stratification in 75 ± 25% of the oceans analyzed in this study, where error is estimated using values shown in Fig. 2.3b. A more conservative threshold of $R_{N2} > 2$ suggests that 60 ± 25% of observed springtime stratification cannot be explained by one-dimensional dynamics.

2.3 SIGNATURES OF ISOPYCNAL TILTING

2.3.1 *Data analysis*

Adiabatic slumping of density fronts produces vertical stratification with a TS structure similar to that of the horizontal density gradient (e.g., Fig. 2.1). Therefore TS relationships will be used to isolate regions where excess stratification may result from tilted horizontal density gradients from regions where other processes are at work. Turner angle provides a metric to quantify the relative contributions of temperature and salinity to density. Turner angles for horizontal (Tu_H) and vertical (Tu_V) gradients are defined as

$$Tu_V = tan^{-1}\left(\alpha\frac{\partial\theta}{\partial z} - \beta\frac{\partial S_A}{\partial z}, \alpha\frac{\partial\theta}{\partial z} + \beta\frac{\partial S_A}{\partial z}\right), \tag{2.7}$$

$$Tu_H = tan^{-1}(\alpha\partial\theta - \beta\partial S_A, \alpha\partial\theta + \beta\partial S_A), \tag{2.8}$$

where ∂ is the difference between data points calculated across isopycnals, and α and β are the thermal expansion and saline contraction coefficients, respectively. Tu_V is determined for each Argo profile using eq. 2.7 by taking data points of θ and S_A at the upper and lower bounds of the 50–90% ML depth range. Tu_H is calculated using monthly MIMOC fields for each 0.5° grid point by fitting a plane to the surface density values at eight neighboring grid points. Surface θ

and S_A along the inclination of the fitted plane (i.e., across gradient) were used to calculate Tu_H using eq. 2.8.

2.3.2 *Case studies*

Turner angles support the inferences drawn from the comparison of one-dimensional simulations and float observations at OWS-P and the IB. To examine the relationship between θ and S_A 40–10 days before the heat flux changes sign, PDFs of Turner angle (Tu_V) are projected onto θ–S_A space with vector magnitudes normalized to the PDF maximum. At OWS-P (Fig. 2.2c) vectors of observed (green) and modeled (orange) θ–S_A lie atop each other, indicating that the model captures both the observed stratification and the observed θ–S_A structure. Neither observed nor modeled Tu_V exhibits any relationship to Tu_H of the surrounding horizontal density structure (purple), suggesting that lateral effects have no significant role.

In the IB, however, the model's inability to replicate observed Tu_V (Fig. 2.2d) corroborates the disagreement between modeled and observed stratification. Instead, observed Tu_V agrees with horizontal across-isopycnal Tu_H, indicative of the horizontal density gradients slumping to produce vertical stratification.

2.3.3 *Global studies*

Monthly values of Tu_H were binned as in 2.2.3 to estimate the TS structure of horizontal density gradients that would tilt to produce vertical stratification. MIMOC-derived Tu_H one month before t_{QNET0} were compared with Tu_V calculated from Argo profiles 40–10 days before t_{QNET0}. Differences in horizontal surface and vertical lower ML Turner angle ($\Delta Tu = |Tu_H - Tu_V|$) are plotted in Fig. 2.4a. Orange regions have TS structure in the stratifying ML consistent with horizontal density gradients (i.e., similar values of Tu_H and Tu_V). Note that the 10-day offset between the selected temporal ranges for Tu_H and Tu_V calculations may result in some Argo data being drawn from a different month than used to calculate Tu_H.

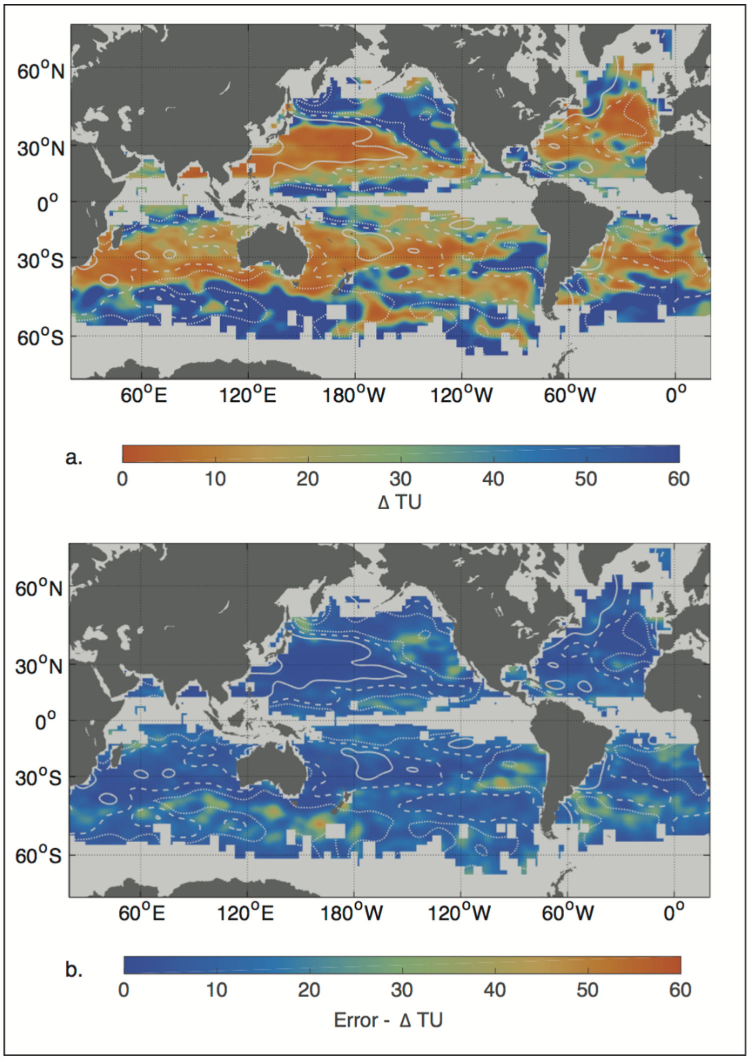

Fig. 2.4. (a) $\Delta\ Tu$ determined as $|\ Tu_H - Tu_V|$ for the month before $t_{QNET}>0$. Tu_H is derived from MIMOC and Tu_V from Argo data using eq. 2.7 and eq. 2.8. (b) Error in $\Delta\ Tu$. Contours of Q_{MLE} at 65 W m^{-2} (solid), 35 W m^{-2} (dashed), 20 W m^{-2} (dotted). Note the change in colorbar. In (a), orange represents low values to indicate observed Tu is similar to that of the horizontal gradient. In (b) the colorbar is inverted to highlight regions with large error.

While Tu_H fluctuates interseasonally (Johnson et al. 2012), monthly changes in Tu_H are relatively small (<15°) in most ocean basins, with large monthly changes in Tu_H occurring in the low latitudes (<20°), coastal regions, and near western boundary currents. Again, error for ΔTu is estimated with a Monte Carlo approach by adding noise to t_{QNET0}, θ, and S_A for repeated calculations of mode Tu (Fig. 2.4b). Of the ~75% of the oceans with $R_{N2} > 1.5$, 40 ± 25% have $\Delta Tu < 15$. Adopting these thresholds for R_{N2} and ΔTu suggests that ~30 ± 20% of the oceans analyzed in this study exhibit springtime stratification influenced by slumping of lateral density gradients.

2.4 STRATIFICATION FROM MLEs

2.4.1 *Global pattern of Q_{MLE} vs. lateral slumping induced stratification*

Maps of Q_{MLE} are created using climatological θ, S_A, and ML depth provided by MIMOC (Fig. 2.4a, b). The 0.5° resolution of MIMOC necessitates a scale factor, similar to what would be applied for coarse resolution models (eq. 2.5). c_p, ρ, and α are calculated for each MIMOC grid point. $|\nabla b|^2$ is calculated (Fig. 4c) for each grid point using neighboring values of ρ in both latitude and longitude to determine the horizontal density gradient:

$$|\nabla_h b| = \frac{-g}{\rho_o}\left(\rho_x{}^2 + \rho_y{}^2\right)^{\frac{1}{2}}. \tag{2.9}$$

L_f is calculated using eq. 2.4, where N are mode values calculated in section 2.2c, and $L_{fmin} = 1$ km. Regions of high Q_{MLE} (Fig. 2.5a; orange) are associated with both the strong lateral gradients of the subtropics and the edges of the deep ML regions of the North Atlantic (NA) and the Antarctic circumpolar current (ACC).

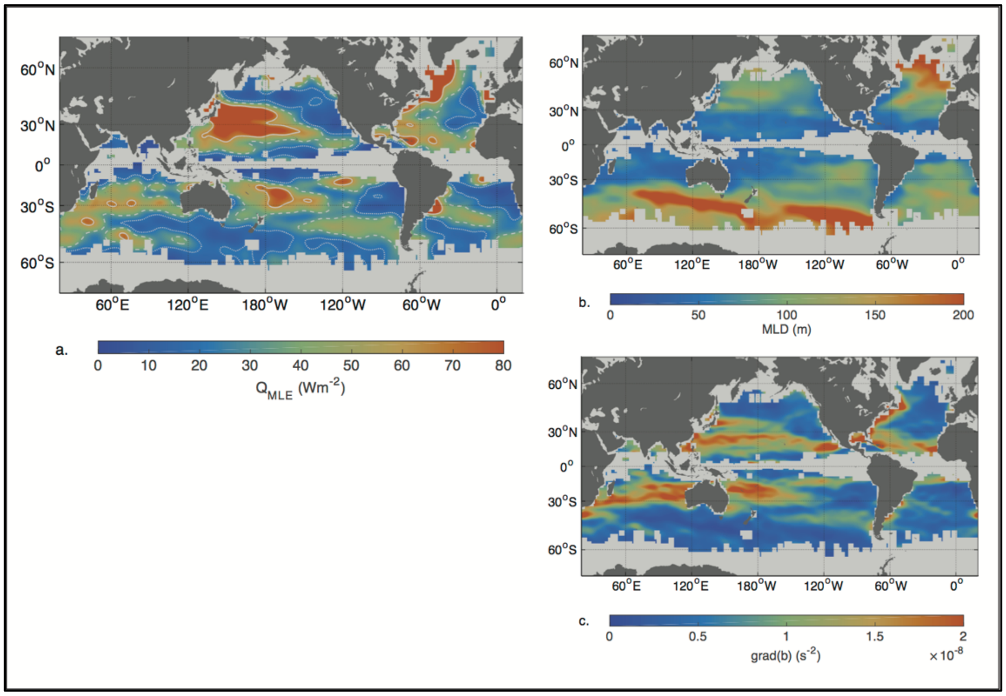

Fig. 2.5. (a) Q_{MLE} (W m^{-2}) for the month before t_{QNET}>0 calculated from eq. 2.5 using MIMOC. Contours of Q_{MLE} at 65 W m^{-2} (solid), 35 W m^{-2} (dashed), 20 W m^{-2} (dotted). (b) Same as (a) for MIMOC MLD and (c) MIMOC derived $\nabla_h b$. Both MLD and ∇b have been binned and smoothed similar to Q_{MLE} (see section 2.4a).

The metric used to compare signatures of R_{N2} and ΔTu (i.e., where enhanced stratification may result from tilting isopycnals) with Q_{MLE} is:

$$Weighted\ \Delta Tu = \frac{1}{1+\Delta Tu} \qquad (2.10)$$

$$Weighted\ R_{N2} = \begin{matrix} for\ R_{N2} > 1 & 1 - \frac{1}{R_{N2}} \\ for\ R_{N2} \leq 1 & 0 \end{matrix} \qquad (2.11)$$

For both, values closer to one indicate properties consistent with MLE induced stratification (e.g., high R_{N2} and ΔTu near 0).

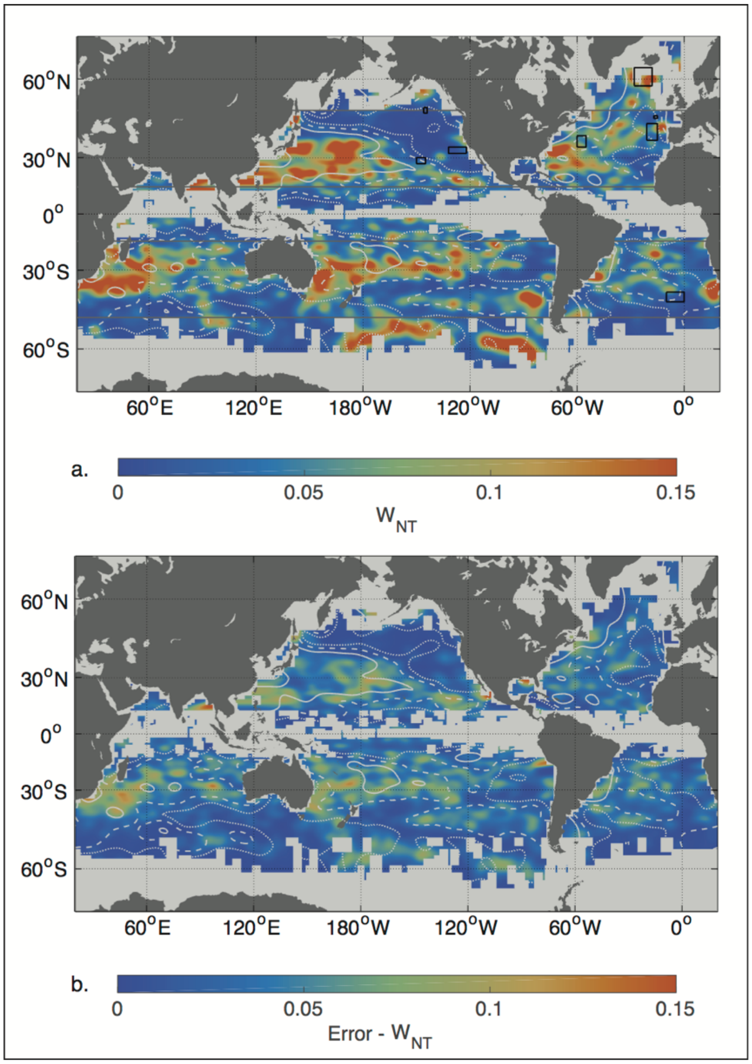

Fig. 2.6. W_{NT} – *Weighted* R_{N2} * *Weighted* ΔTu. Higher values of W_{NT} are stronger signatures of increased R_{N2} and smaller values of ΔTu, both of which indicate lateral slumping induced stratification. Contours of Q_{MLE} at 65 Wm^{-2} (solid), 35 Wm^{-2} (dashed), 20 Wm^{-2} (dotted). Black boxes refer to the following observational studies. OWS Papa (145°W, 150°N); SPICE (140°W, 25°N; Ferrari and Rudnick 2000), LATMIX (65°W, 37°N; Shcherbina 2013), (150°W, 30°N; Hosegood 2006), NAB08 (20°W, 60°N; Mahadevan et al. 2012), OSMOSIS (48°N, 16°W), POMME (18°W, 42°N; Karleskind et al. 2011), SOSCEX (10°N, 42°S; Swart 2013). (b) Error in W_{NT}.

Multiplying these weighted values

$$W_{NT} = Weighted\ \Delta Tu * \ Weighted\ \ R_{\mathrm{N2}}\ , \tag{2.12}$$

provides a single metric that describes where frontal slumping is likely responsible for excess upper ocean stratification (Fig. 2.6a). Error for W_{NT} (Fig. 2.6b.) is estimated by propagating error for R_{N2} and ΔTu (Fig. 2.3a,Fig. 2.4b).

The subtropical North and South Pacific, the subtropical southern Indian Ocean, and the eastern South Pacific exhibit high W_{NT} coincident with high Q_{MLE} (Fig. 2.6 and Fig. 2.5a). This relationship is not as discernable in the North and South Atlantic. Further discussions of these patterns are found in sections 2.5 and 2.6.

2.4.2 *Global distributions*

PDFs of ∇b, H, and Q_{MLE} (Fig. 2.7) describe the characteristics of high W_{NT} regions. PDFs of Q_{MLE} (Fig. 2.7c) for various thresholds of W_{NT} show that regions that exhibit lateral slumping induced stratification also tend toward higher values of Q_{MLE}. This reflects similarities in geographical patterns between Q_{MLE} and W_{NT} (Fig. 2.5a and Fig. 2.6) and suggests that regions of lateral slumping occur where theory predicts MLEs to be prevalent in stratifying the ML. 60 ± 10% of regions with a $W_{NT} > 0.5$ are also regions where $Q_{MLE} > 40$ W m^{-2} (i.e., the mode of the Q_{MLE} PDF for $W_{NT} > 0.5$, Fig. 2.7a) suggesting that MLEs may be responsible for enhanced stratification in 25 ± 15% of the world's oceans.

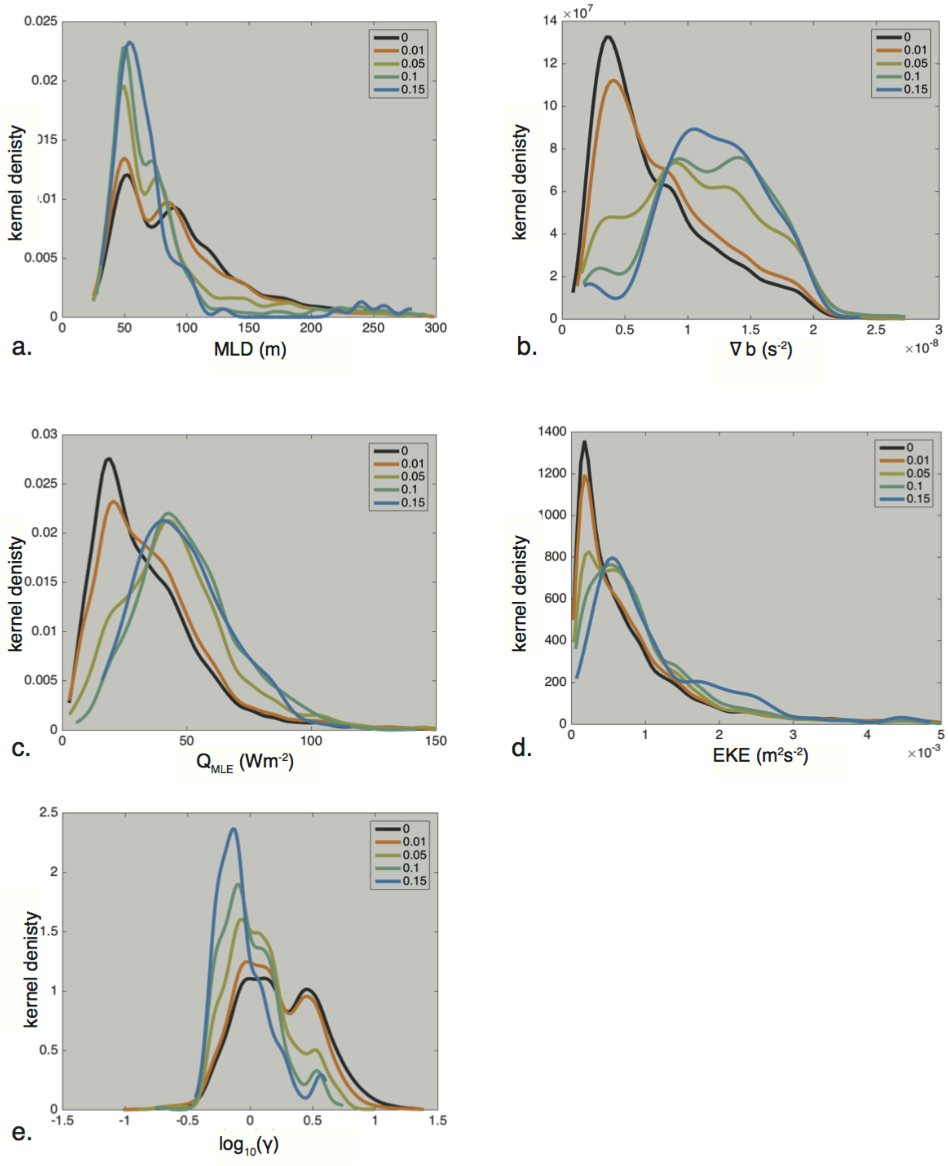

Fig. 2.7. PDFs of (a) ∇b, (b) mixed layer depth, (c) Q_{MLE}, (d) eddy kinetic energy, (e) log (γ_W). Black lines represent the distribution of all the oceans analyzed in this study. Colored lines represent distributions for regions of the ocean that exceed values of W_{NT} (0.01, 0.05, 0.1, 0.15). Higher values of W_{NT} correspond to increased evidence for lateral slumping. For all variables, shifts in the PDF between all regions analyzed (black) and regions exceeding 0.05 (yellow) are statistically significant.

Q_{MLE} is proportional to H^2 and $\nabla_h b^2$, suggesting that MLEs tend to occur in regions of deep MLs and strong lateral gradients. In regions of high W_{NT}, the mode of ∇b shifts towards higher values, yet the mode of H does not change. In fact, the distribution of H shifts away from the deepest ML and retains only a small portion of regions with MLD greater than 200 m. The shift in $\nabla_h b$ is intuitive; regions of strong lateral density gradients are theorized to have an abundance of submesoscale fronts to source the APE that allows MLEs to grow, slump vertical isopycnals, and stratify the upper ocean. A more subtle mechanism sets the PDF of H. These results suggest that the restratifying effects of lateral slumping by MLE limit the coexistence of strong lateral density gradients and deep MLs. The shift in PDFs of $\nabla_h b$ and H are consistent with signatures of high W_{NT} and high Q_{MLE} in the mid latitude regions of strong lateral density gradients that generally have shallower wintertime MLs. There is only a small signature of high W_{NT} and high Q_{MLE} in the high latitude regions of modest lateral density gradients and deep MLs. This may suggest that MLEs are acting to preferentially stratify deep MLs.

2.4.3 *Horizontal buoyancy gradients vs. mixed layer depths*

The definition of Q_{MLE} (eq. 2.3) implies that regions with strong horizontal density contrasts and deep MLs restratify due to differential lateral advection of buoyancy, thereby reducing the ML depth and the horizontal gradient. Regions with these conditions should be unstable and rare. This relationship manifests as a negative correlation (~ –0.6) between H and $\nabla_h b$ in the mid latitudes (Fig. 2.8) and is visually apparent by comparing maps of wintertime H and $\nabla_h b$ (Fig. 2.5b, c).

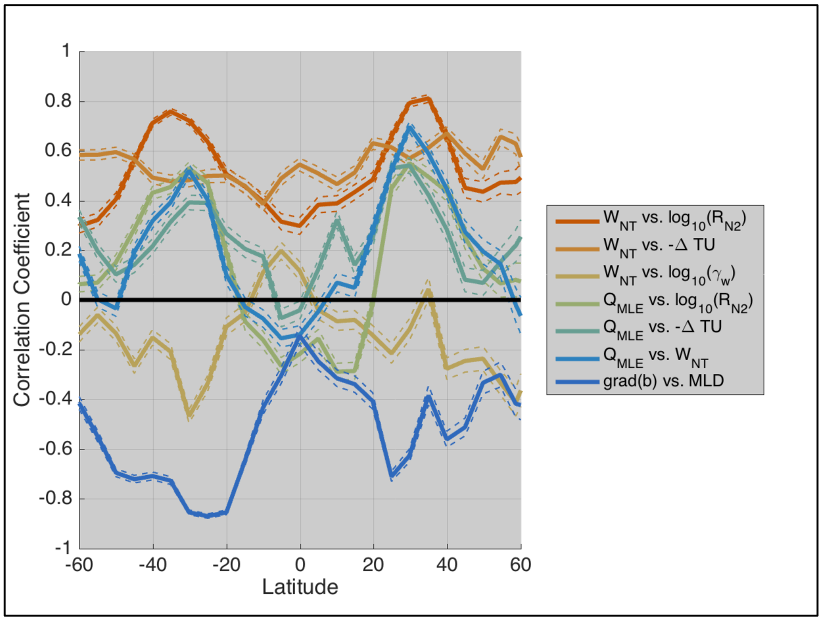

Fig. 2.8. Latitudinal relationships between W_{NT} with R_{N2}, ΔTu, γ_W, and Q_{MLE}; Q_{MLE} with R_{N2} and ΔTu; $\nabla_h b$ with MLD. Positive (negative) values suggest that the two variables are correlated (anti-correlated) within that latitude bin. Here, correlation coefficients between variables were computed in zonal sections of 5° latitude bins. Dotted lines represent 95% confidence intervals.

Climatological relationships between H and $\nabla\nabla_h$ during winter and summer provide additional evidence (Fig. 2.9). Summer ML depths are generally shallow despite the magnitude of lateral buoyancy gradients, pointing to the importance of surface heating in setting stratification and ML depth (Fig. 2.9a, c) during this time. Wintertime surface forcing drives deep MLs (Fig. 2.9b, d) yet $\nabla_h b$ appears to set an upper bound on mixed layer depth. The slope of this relationship corresponds to a Q_{MLE} O(100) W m^{-2} (Fig. 2.9), comparable to values inferred by Mahadevan et al. (2012). This wintertime relationship between H and $\nabla_h b$ is consistent with the idea that the maximum winter ML depth is set by a competition between processes that deepen the ML (e.g., wind and convective mixing) and MLEs that shallow it (Fox-Kemper and Ferrari 2008; Mahadevan et al. 2012).

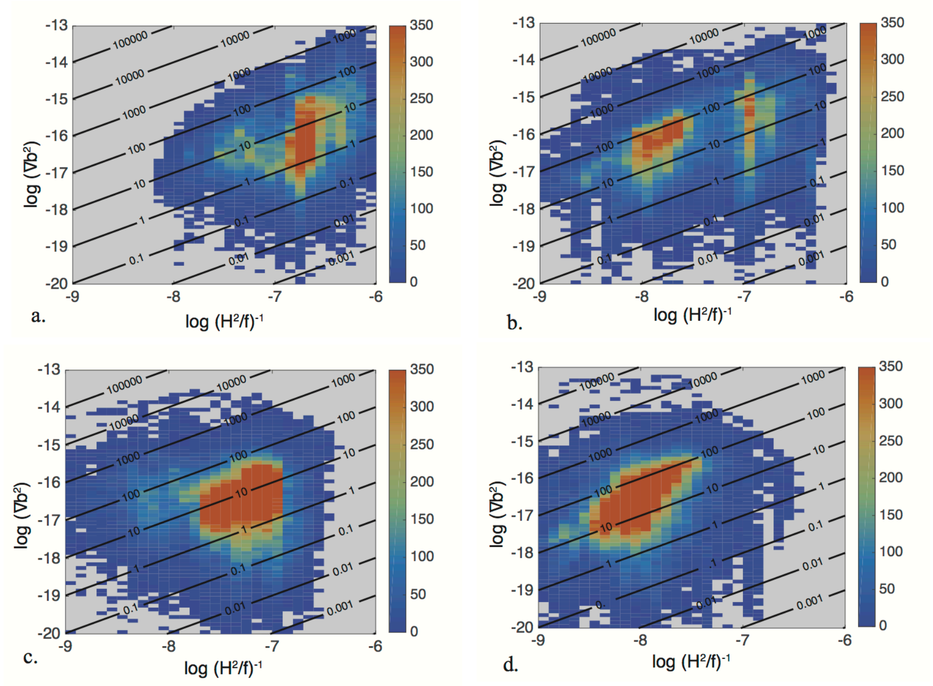

Fig. 2.9. PDF relating surface density gradients (∇b) and mixed layer depths (H). Contours are $Q_{MLE} \propto {}^{\nabla_h b^2 H^2}/_{f}$ (eq. 2.3). (a) Northern Hemisphere (>10°N) summer (August). (b) Northern Hemisphere (>10°N) late winter (February), (c) Southern Hemisphere (>10°S) summer (February). (d) Southern Hemisphere (>10°S) late winter (August). The summertime relationship between ∇b and H suggests MLEs do not have a dominant role in setting upper ocean stratification. Wintertime H increases, but appears to be restrained by $\nabla_h b$. This restraint is shown as most regions of the worlds oceans are on a Q_{MLE} contour O(100 W m^{-2}), consistent with the significance of MLEs on the upper ocean.

2.5 REGIONAL STUDIES

W_{NT}, Q_{MLE}, R_{N2}, and ΔTu exhibit latitudinal-dependent correlations (Fig. 2.10) that provide a framework for closer examination of regional patterns of MLE influence. Correlations between W_{NT} and Q_{MLE} are largest at mid-latitudes, and drop off near the equator and higher latitudes, with a small increase in the high latitude Southern Ocean. This discussion considers the results presented in Fig. 2.3, Fig. 2.4, Fig. 2.7, and Fig. 2.8 in the context of Q_{MLE} (Fig. 2.5.).

2.5.1 *Mid-latitude*

High W_{NT} coincides with high Q_{MLE} in regions associated with subtropical gyres and convergent flows throughout most ocean basins. This geographic distribution is consistent with PDF shifts (Fig. 2.7) that suggest the majority of lateral slumping is occurring in regions with strong gradients and shallower MLs, and can be seen in the midlatitude correlation between W_{NT} and Q_{MLE} (Fig. 2.8). The band of W_{NT} extending from Japan to Mexico coincides with the sharp gradients of the North Pacific convergence zone and subtropical front (Fig. 2.5c). Wintertime observations from this region (Hosegood et al. 2006, 2008; Shcherbina et al. 2009) reveal submesoscale dynamics of lateral slumping and possible ML and symmetric instabilities, which are predecessors to fully developed MLEs that drive stratification through lateral slumping (Thomas and Ferrari 2008; Boccaletti et al. 2007). The signal of high W_{NT} is patchy and fills the western subtropical NA. Here, values of R_{N2} are large in the west and decrease eastward, consistent with patterns of Q_{MLE}.

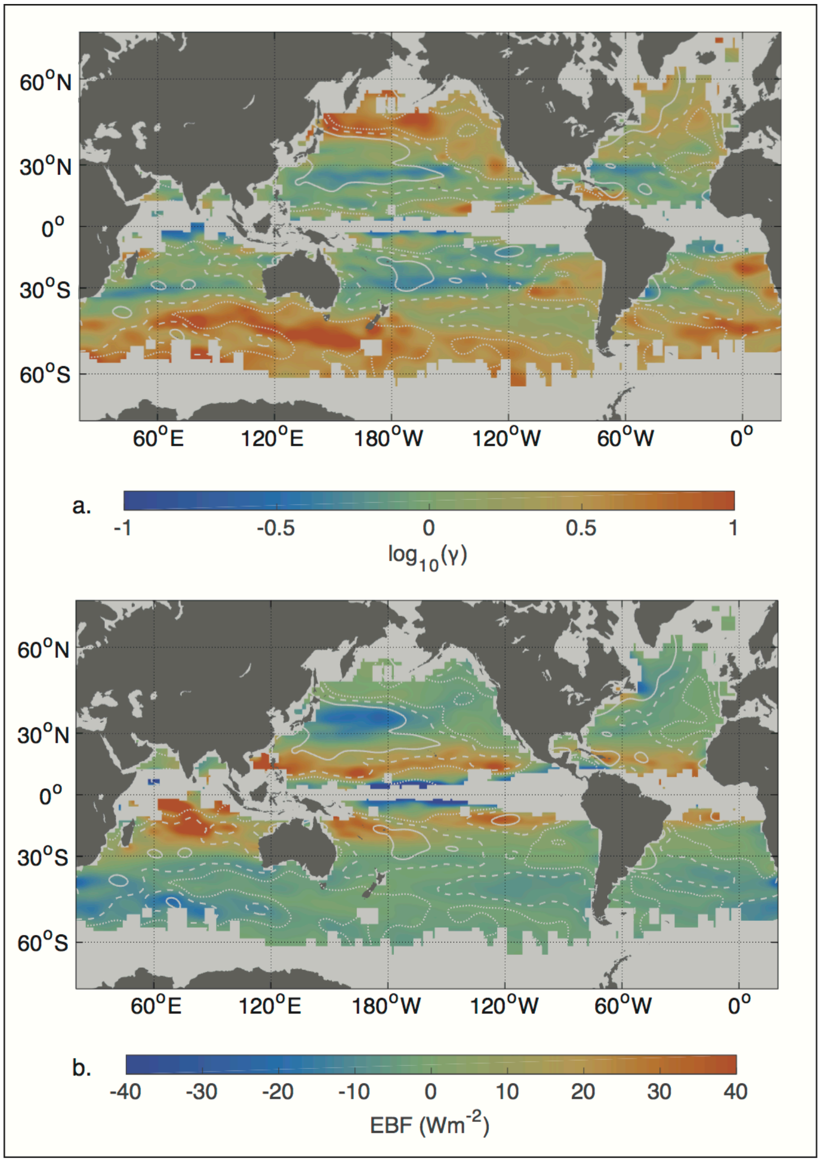

Fig. 2.10. (a) log(γ_W) negative values suggest that frontal processes dominate upper ocean stratification, while negative values suggest that wind processes are important. (b) Ekman buoyancy flux (EBF) in W m^{-2}. Positive values suggest that EBF is stratifying the upper ocean, while negative values indicate winds maintain the front working against MLEs. Contours of Q_{MLE} at 65 W m^{-2} (solid), 35 W m^{-2} (dashed), 20 W m^{-2} (dotted).

In the Southern Hemisphere, elevated W_{NT} extends east off the southern tip of Africa and continues through the subtropical gyre to the west coast of Australia. This pattern also exists in the South Pacific as wedges extending eastward off the coast of Australia and another extending westward off the archipelagos of southern Chile.

2.5.2 *High latitudes*

Q_{MLE} at the high latitude tends to be a result of deep MLs and modest gradients. Note that Q_{MLE} estimates are not largest in regions of the deepest MLs associated with the ACC and NA (Fig. 2.5a–c), largely because these regions have weak lateral density gradients. Instead, Q_{MLE} appears in the transition away from deepest MLs, but where MLs, deeper than those found in subtropical fronts, and lateral buoyancy gradients can co-exist. Q_{MLE} associated with these deep MLs agrees with W_{NT} in the subpolar NA, where gradients extend from the tip of Newfoundland towards Iceland, but disagrees south of Greenland where ΔTu values are large. The W_{NT} signal in the IB is consistent with the case study (Fig. 2.2b, d) and with results reported by Mahadevan et al. (2012).

In the Southern Hemisphere, large Q_{MLE} associated with deep MLs suggests springtime stratification driven by MLEs, conflicting with W_{NT} patterns that do not show the expected relationship between vertical and lateral TS structure. The existence of high Q_{MLE} in the southern Indian Ocean around 50°S does not agree with low values of W_{NT} that result from the large ΔTu. In the South Pacific, the story is opposite, with high W_{NT} accompanied by low Q_{MLE} in a region that extends east from the New Zealand coast towards the southern tip of Chile.

2.5.3 *Equatorial*

The correlation between W_{NT} and Q_{MLE} falls off near the equator (Fig. 2.8) as patchy signals of high W_{NT} rarely coexist with regions of high Q_{MLE} below 20° latitude. There is no strong signal between W_{NT} and Q_{MLE} in the Arabian Sea or the Bay of Bengal, which may be attributed to monsoonal dynamics and freshwater fluxes that may dominate the lateral processes here. Fox-Kemper et al. (2008) discuss the implications of Ψ at low latitudes, where the tendency for rapid restratification is accompanied by an increase in eddy growth rates. Near the equator, Rossby adjustment occurs faster and may be important for lateral slumping (Tandon and Garrett 1994). Additionally, the lack of signal in the equatorial regions may reflect uncertainties associated with defining $t\_{}_{QNET0}$ in tropical regions that exhibit weak or non-existent seasonal cycles in $Q_{NET.}$

2.6 ALTERNATIVE HYPOTHESES

Lateral slumping is ubiquitous where fronts are present and MLEs may be a leading order mechanism that slumps fronts, but other lateral processes also modify upper ocean stratification.

2.6.1 *Wind dynamics*

Winds interacting with fronts can induce ageostrophic secondary circulations that interact with the effects of MLEs. Winds blowing up/down front have restratifying/destratifying effects on the upper ocean (Thomas and Ferrari 2008; Mahadevan et al. 2010), and can sharpen fronts to trigger symmetric instabilities that impact stratification (Taylor and Ferrari 2010; D’Asaro et al. 2011).

Thomas and Ferrari (2008) assess the relative importance of boundary layer dynamics on upper ocean stratification by deriving estimates for the differential advection in the ML resulting from frontal processes vs. frictional processes due to wind stress and geostrophic stress. Studies that estimate the global importance of geostrophic stress (Wenegrat and McPhaden 2016) indicate this process may be influential at low latitudes, but do not fully explain patterns of W_{NT}. Here, the discussion focuses on wind stress where the ratio for differential advection is:

$$\gamma_{wind} = \frac{\Delta v_{wind}}{\Delta v_{front}} = \frac{(\tau/\rho)^{1/2} Ro^{-1}}{\nabla b H f^{-1}} \tag{2.13}$$

Ro is the Rossby number, taken here as $Ro = 0.1$ following Thomas and Ferrari (2008). γ_{wind} is computed following the methods used to compute Q_{MLE} (section 2.4a), with wind data from CCMP, and ρ, ∇b from MIMOC (Fig. 2.10a). Positive values imply wind to be dominant and negative values imply frontogenetic effects to be dominant. It is evident that winds have an influence on upper ocean stratification where Q_{MLE} is weak. The magnitude of this scaling depends on the choice of Ro. At the submesoscale, Ro approaches O(1), decreasing γ_{wind} by an order of magnitude and therefore decreasing the number of regions where wind effects are dominant. Nonetheless, the geographic distribution of γ_{wind} would remain the same and some conclusions may be drawn from these patterns. Correlation between log(γ_{wind}) and W_{NT} is opposite that of Q_{MLE} (Fig. 2.8) with high negative correlation in the mid latitudes, consistent with where frontogenetic dynamics dominate wind. Correlation falls at high latitudes and near the equator. The absence of strong positive correlation between log(γ_{wind}) and W_{NT} suggests that wind effects do not describe patterns of frontally enhanced stratification consistently. Similarly, PDFs of log(γ_{wind}) shift towards lower values for regions of high W_{NT}, consistent with the idea that frontogenetic processes are responsible for observed signatures of frontal slumping.

The competing effects of winds on a front can be described as an Ekman buoyancy flux (EBF; Thomas and Lee 2005; D'Asaro et al. 2010).

$$EBF = \frac{1}{\rho_o}\frac{\tau \cdot \nabla_h b}{f} \tag{2.14}$$

Downfront winds drive Ekman transport that moves waters from the dense (cold) side of fronts over less dense waters on the warm side, producing negative EBF that drives vertical mixing and acts to maintain the front. Upfront winds move light (warm) waters over dense (cold), producing positive EBF that drives frontolysis, slumping the front to create vertical stratification. Stratification resulting from positive EBF will have a signature similar to that driven by MLEs and other processes that adiabatically slump horizontal gradients. Observational and numerical evidence of local wind–front interactions illustrate the impact of EBF on the evolution of fronts (Thomas and Lee 2005; D'Asaro et al. 2010; Mahadevan, Tandon and Ferrari, 2010). Some cases find the buoyancy budget driven by EBF, rather than MLEs (Haney et al. 2012; Thomas et al. 2016), illustrating the importance of considering these effects when discussing global estimates of frontally modulated stratification. EBF can be represented as an equivalent heat flux by multiplying (eq. 2.1) by $\left(\frac{c_p \rho}{g \alpha_T}\right)$ to obtain Q_{EBF}. It is assumed that the effects of EBF and MLE are linear, therefore Q_{MLE} and Q_{EBF} are comparable. Here, wind data from CCMP, and ρ and ∇b from MIMOC are processed similar to Q_{MLE} as described in section 2.2c, yielding a global distribution of climatological Q_{EBF} during the transition into spring (Fig. 2.10b). This climatological view of Q_{EBF} reveals strong destratifying effects of the westerlies on the Kuroshio (D'Asaro *et al.*, 2010), Gulf Stream (Thomas et al. 2016), and Antarctic polar front and strong restratifying effects in the presence of trade winds.

High latitude regions lack W_{NT} (Fig. 2.6), even in the presence of high Q_{MLE} (Fig. 2.5a), evident in the fall off in correlation between Q_{MLE} and W_{NT} (Fig. 2.8). This discrepancy occurs in the presence of both negative Q_{EBF} (Fig. 2.10b) and $\gamma_{wind} > 1$ (Fig. 2.10a), implying that wind dynamics dominate over frontal effects in setting upper ocean stratification in these regions. This comparison must be taken with the caveat that large-scale monthly climatologies of winds and density gradients likely misrepresent the impact of EBF on localized fronts, as the instantaneous orientation of winds and fronts will differ from those derived from averages taken over larger spatial and temporal spans. Furthermore, an asymmetry of downfront vs. upfront winds implies these values cannot be represented by climatological forcing. Thus the data and analysis tools employed here may be insufficient to accurately assess the localized role of EBF.

2.6.2 *Mesoscale dynamics*

Eddy kinetic energy (EKE = u^2+v^2) is calculated from AVISO geostrophic velocity anomalies (http://www.aviso.altimetry.fr/duacs/) and binned as described in 2.2. Patterns of high EKE (Fig. 2.11) coincide with high Q_{MLE} and high W_{NT}, particularly near western boundary currents and some sections of the ACC. EKE quiescent regions of the North Pacific, subtropical South Pacific, and in the South Indian Ocean south of Australia also coincide with low values of W_{NT}. The PDF shift of EKE (Fig. 2.7) also reflects the concurrence of high W_{NT} and EKE. This might be expected, as submesoscale flows and fronts can emerge from straining and stirring of the mesoscale. Yet, while mesoscale activity can transport buoyancy laterally, the majority of restratification is achieved through vertical transfer of buoyancy resulting from the overturning circulation induced by submesoscale instabilities (Fox-Kemper and Ferrari 2008).

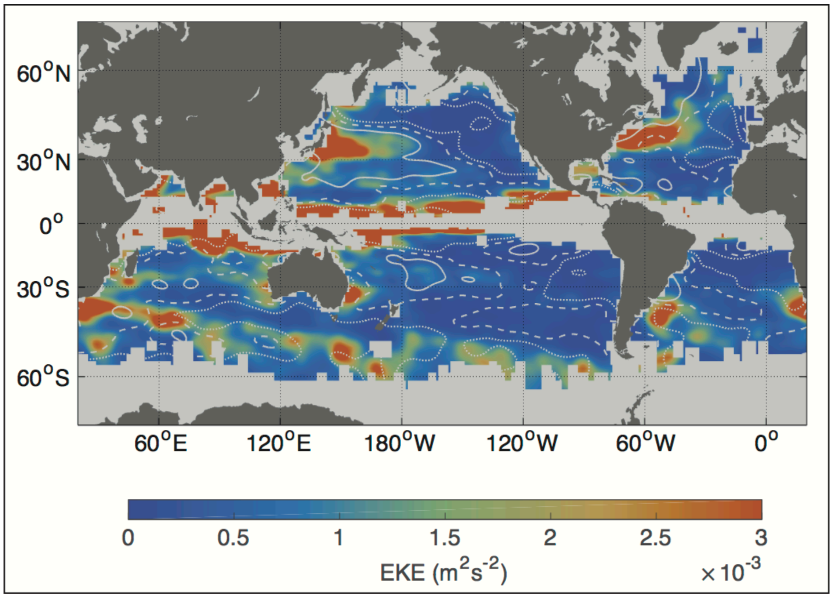

Fig. 2.11. Eddy kinetic energy EKE $(m/s)^2$ derived from AVISO geostrophic velocity anomalies. Contours of Q_{MLE} at 65 Wm^{-2} (solid), 35 Wm^{-2} (dashed), 20 Wm^{-2} (dotted).

2.6.3 *Unresolved processes*

Other causes may be responsible for the discrepancy between observed and modeled stratification during the transition into spring. Here, the discussion of Turner angle is extended to include modeled Turner angle, Tu_M, calculated using model output similar to Tu_V (eq. 2.7), and $\Delta Tu_{OM} = |Tu_M - Tu_V|$, similar to ΔTu (2.3.3). ΔTu_{OM} and ΔTu are used to partition the ocean into five categories (Fig. 2.12).

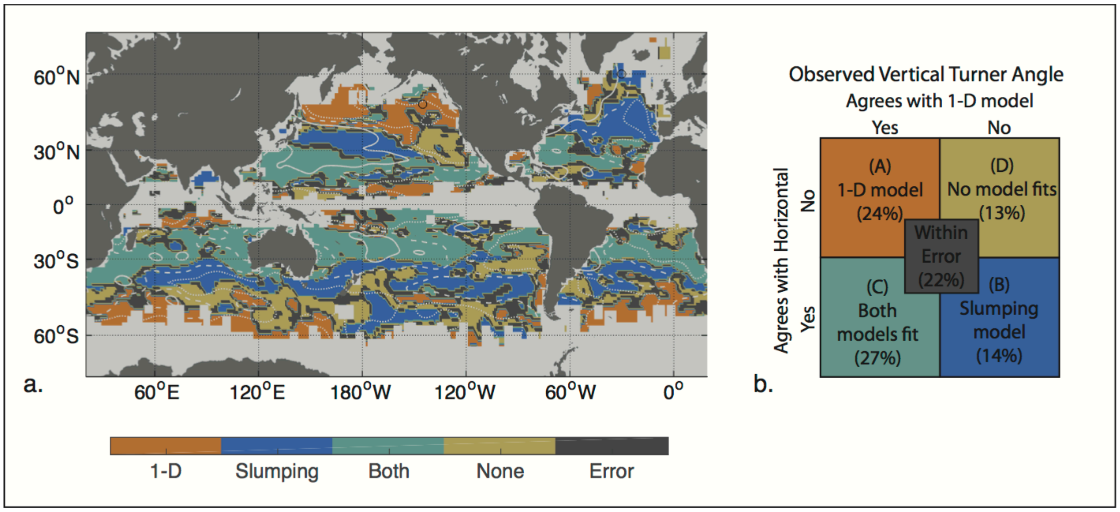

Fig. 2.12. Observed Turner angle is compared with modeled vertical and horizontal Turner angles (see Fig. 2.1). Descriptions of each of these categories is summarized in (b), where agreement is set at a threshold of $\Delta Tu<30$. (A) $\Delta Tu_{OM}<30$, (B) $\Delta Tu<30$, (C) both $\Delta \mathrm{T}u_{OM}<30$ and $\Delta Tu<30$, (D) both $\Delta Tu_{OM}>30$ and $\Delta Tu>30$. Contours of Q_{MLE} at 65 W m^{-2} (solid), 35 Wm^{-2} (dashed), 20 Wm^{-2} (dotted).

While diagnosing all possible dynamics is beyond the scope of this analysis, some general conclusions can be inferred from this representation (Fig. 2.12). Category (A) are regions consistent with vertical mixing. These account for 24% of the oceans analyzed and is most prominent in the subpolar North Pacific. Category (B) are regions consistent with lateral slumping and account for 14% of oceans analyzed in this study. Category (C) includes regions where observations agree with both vertical mixing and lateral slumping and accounts for 27% of the oceans analyzed. Note that (C) characterizes regions within the subtropics, where horizontal density gradients are strong, Q_{MLE} is high, and EBF is positive. Category (D) are regions where observations do not agree with vertical mixing or frontal slumping. This accounts for 13% of the regions analyzed and may point to the importance of other lateral processes. For example, category (D) characterizes regions of the ACC. While MLEs are thought to be leading order on time scales shorter than most large-scale geostrophic flows, this may not be true for some of the fastest currents. The final category (eq. 2.5) are regions where differences in Turner angle are within error of these different categories and account for 22% of the ocean analyzed.

2.7 CONCLUSIONS

Profiling float observations compared to a one-dimensional model of the ocean ML suggest that parameterizations ignoring lateral processes underestimate upper ocean springtime stratification for 75±25% of the world's oceans. Relationships between the large-scale horizontal TS and local vertical TS are used to identify regions where lateral gradients are transformed into vertical stratification. This analysis indicates that lateral slumping is most likely responsible for 40±25% of the increased stratification not captured by the models, therefore influencing 30±20% of the world's oceans. Patterns of lateral slumping (larger W_{NT}) mimic patterns of parameterized MLE (high Q_{MLE}), with 60±10% of regions with $W_{NT} > 0.05$ having an associated Q_{MLE} flux > 40 W m^{-2} (Fig. 2.2c). This correspondence suggests that MLEs have an important role in stratifying the upper ocean during the transition into spring. Specifically, regions of high W_{NT} tend to have strong lateral density gradients and moderate mixed layer depths, with a small distribution of W_{NT} in high latitude regions of the NA and Southern Ocean with deep MLs.

Fox-Kemper et al. (2011) parameterized MLEs into global circulation models using (eq. 2.1) with $\Psi = \frac{\Delta s}{L_f}\Psi_o$. Including this parameterization shallows the MLD in the North Pacific extending east of Japan, in the Gulf of Mexico, in basins extending both east and west from Australia, and in the Southern Ocean, which are all consistent with patterns of W_{NT} found here. However, patterns of high W_{NT} in the shallow ML regions of the subtropics found here are not in agreement with (Fox-Kemper et al. 2011); this may reveal the limitations of eq. 2.1 to capture MLEs in shallow MLs or may be attributed to the importance of other stratifying processes in the subtropics.

Despite evidence from observations and models that indicate the importance of wind stress on frontal stratification via the Ekman buoyancy flux, the large-scale patterns of EBF calculated here do not further improve the predictions of W_{NT}. This is most likely due to the inability of large-scale wind and gradient statistics to capture local dynamics. This study suggests the relative contributions of EBF to large-scale patterns of upper ocean stratification are not resolved by this analysis.

Although this study focuses on springtime stratification, the relationship between H and $\nabla_h b$ (Fig. 2.8) indicate that MLEs could limit the depth of the wintertime ML in regions with strong lateral gradients, with a typical restratification flux of O(100 W m^{-2}) This is consistent with studies showing heightened submesoscale activity in winter (Callies et al. 2015). Analogous to spring stratification, MLEs could also influence stratification during fall as surface forcing works to deepen mixed layers in the presence of strong summer lateral density gradients. The full seasonal implications of lateral slumping remain to be explored.

3 CHAPTER 2: A STRATIFYING SUBMESOSCALE FRONT, PART I - KINEMATICS

3.1 INTRODUCTION

Large-scale gradients of temperature (T) salinity (S), and therefore density (ρ) are not smooth and continuous, but contain a rich structure of smaller, sharper mesoscale O(10^2 km) and submesoscale O(10^{-1}–10^1 km) gradients. This continuum of features in the ocean implies a pathway for largescale energy input at the surface to move towards smaller scales. The pathway between large-scale and mesoscale currents and eddies can be described by the 2D, non-divergent framework of geostrophic turbulence (QG; Charney 1971) governed by interior potential vorticity (PV) dynamics. This framework experiences an inverse cascade of energy back into large scales and therefore falls short at describing a rich abundance of submesoscale features found to be ubiquitous in the upper ocean (Rudnick and Ferrari 1999; Hosegood et al. 2006; Mahadevan et al. 2012; Thompson et al. 2016).

The existence of submesoscales is more accurately represented by a surface quasigeostrophy (sQG) framework set by the buoyancy structure at the surface instead of interior PV. This allows gradients near the surface to be stirred by the energetic geostrophic field into sharp fronts and filaments that evolve on a timescale of days. This implies that submesoscale flows are associated with advective timescales with Rossby number ($Ro = \frac{\zeta}{f}$) O(1). This parameter space hosts a range of dynamics that interact with the front to further transfer energy and tracers to smaller scales in route to dissipation. One conduit for this energy is the conversion of available potential energy (APE) into kinetic energy (KE) by processes that adiabatically rearrange buoyancy at a front, and turning horizontal stratification into a vertical one. This work presents high-resolution data of a submesoscale surface intensified front that undergoes strong ageostrophic secondary circulations (ASC) associated with large vertical velocities that tilt the front over and stratify the mixed layer (ML) within one day.

Observing submesoscale processes is inherently difficult due to the crucial need to obtain high-resolution scalar and velocity fields (0.1–1 km) over a large spatial domain (10–100 km) on the order of days. Submesoscale flows share spatial and temporal scales with inertia-gravity waves (IGW). Shipboard mesoscale surveys are particularly designed to filter aliased IGW (i.e., Rudnick, 1996) and therefore risk not resolving the submesoscale variability. Conversely, surveys designed to focus on submesoscale temporal and spatial scales risk aliasing unresolved near inertial motions. Observations of the upper ocean reveal regions with many surface intensified sharp gradients populated over a small domain. These are easily evaluated in a statistical sense (e.g., Rudnick and Ferrari 1999; Hosegood, Gregg and Alford 2006; Mahadevan et al. 2012; Shcherbina et al. 2013; Thompson et al. 2016). This survey documents the superinertial/inertial evolution and along front variability of one single front. The data, collected as a part of the Assessing the Effects of Submesoscale Ocean Parameterizations program (AESOP) are particularly well suited for studying frontal processes that may be governed by submesoscale dynamics.

3.2 DATA COLLECTION

The data were collected in the California Current System (CCS) 4–5 August 2006, yearday (yd) 216–217. On 30 July 30 2006 (yd 212), northerly winds increased offshore from near zero to 0.5 N m^{-2} over the course of two days.

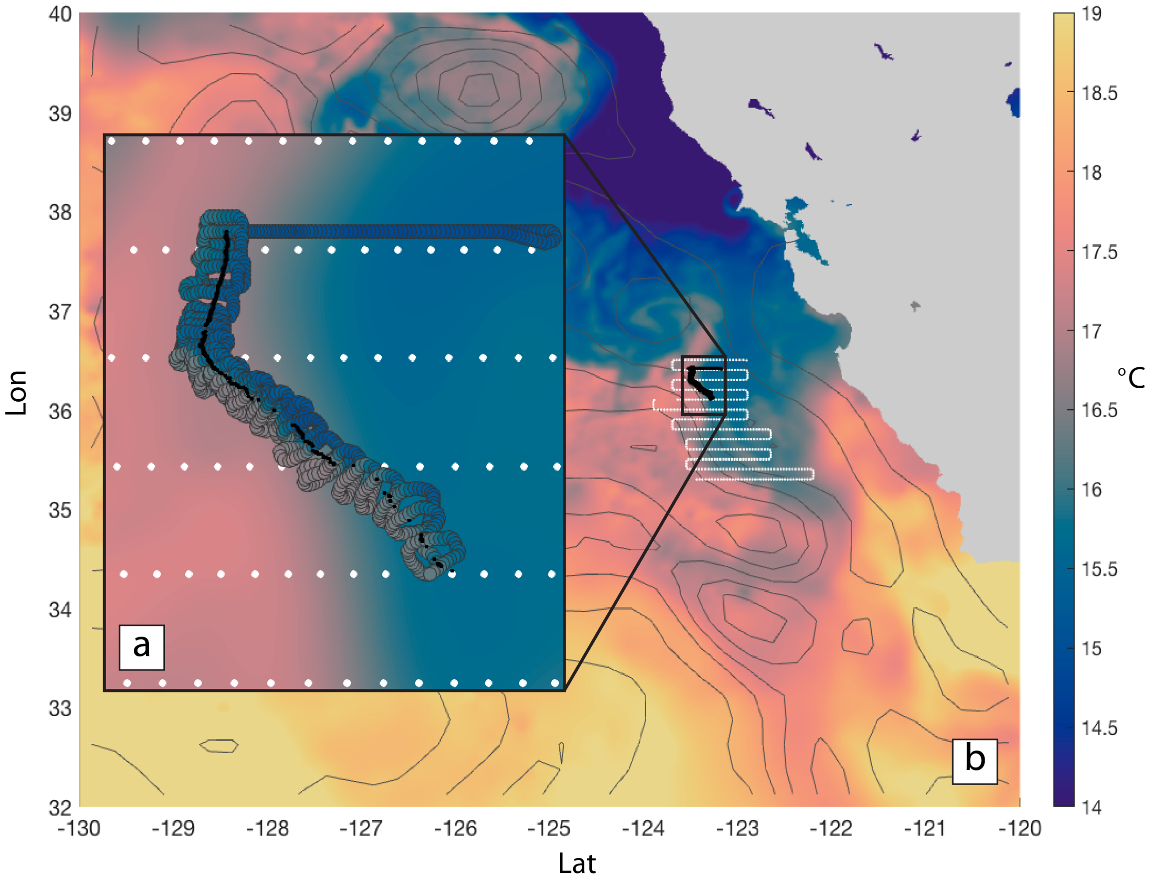

Fig. 3.1. a) Detail of sea surface temperature (SST) and mesoscale survey (white). Lagrangian float track (black dots) and ship track colored with ship underway temperature. b) SST off the California Coast on 4 August 2006 from the Group for High Resolution SST (GHRSST - https://podaac.jpl.nasa.gov). Contours are AVISO mean sea level anomaly. White dots outline the mesoscale survey ship track. Block dots outline the Lagrangian survey ship track. Both tracks are during the restratifying phase.

The along shore winds set up an Ekman transport offshore with an associated upwelling index of 150 (https://www.pfeg.noaa.gov/products/las.html), consistent with sea surface temperature (SST) revealing cold salty water upwelling from the deep along the coast (Fig. 3.1).

An energized mesoscale field associated with the southward California current stirred the upwelled waters with the warmer fresher surface waters offshore to create multiple smaller fronts and filaments. A front sitting at the edge of the upwelled waters became the target of coordinated surveys that captured different phases of the frontal evolution. The first phase was 1–3 August 2006 (yd 213–215) as northerly winds aligned downfront continuously homogenized the upper 30 m (not discussed here). The second phase, 4–5 August 2006 (yd 216–217), occurred as winds decreased rapidly and the upper 30 m stratified. This restratification phase is the focus of this study.

During each phase, the front was surveyed by two ships simultaneously. The R/V *Wecoma* performed a mesoscale survey of zonal transects set 11 km apart while towing a SeaSoar profiling vehicle between 16–350 m (i.e., mesoscale survey) (Fig. 3.1). Details of the mesoscale survey can be found at Pallàs-Sanz et al. (2010a,b) and Johnston et al. (2011), which characterize the vertical velocity and turbulence of the front on scales of 10–40 km. Starting 30 hr later, the R/V *Melville* surveyed around a drifting Lagrangian float (D'Asaro 2003) using a Triaxus profiler, thus conducting a Lagrangian survey on a scale of 5 km. Satellite SST was used to locate the front followed by an initial Triaxus transect that identified the cross frontal structure in depth (see section 3.4). The Lagrangian float was placed in the center of the front targeted for the 23.8 kg m^{-3} isopycnal. When neutrally buoyant, the float is designed to follow the average three-dimensional motion of the water immediately surrounding it. The float's position was tracked acoustically using a TrackPoint II USB system operating at 15 kHz as it was advected downstream by the frontal flow, allowing the ship to survey around the float while towing the Triaxus undulating profiler. The survey lasted 30 hr as the float traveled roughly 50 km along the front. During this time, the ship circled the float 31 times, taking about one hour to complete loops 3–5 km in diameter (Fig. 3.1).

The Lagrangian float was equipped with two Seabird sensors 1.4 m apart on the top and bottom of the hull that collected measurements of pressure (P), temperature (T), and salinity (S) every 30 s. The float was programed to estimate density (ρ) from an equation of state ρ(P,T,S) and adjust its volume to achieve neutral buoyancy $b = -\frac{g\rho}{\rho_o}$, where g is gravity and ρ_o is a reference density of 1024 kg m^{-3}.

The shipboard flow through system collected T and S at ~5-m depth every 30 s providing a horizontal resolution of roughly 100 m. Shipboard meteorological measurements were used to estimate air–sea fluxes based on the COARE 3.5 bulk formula. Shipboard mounted RDI ADCPs included 50-kHz and 150-kHz sonars.

Triaxus was equipped with temperature and conductivity sensors, chlorophyll fluorometer, transmissometer, dissolved oxygen sensor, as well as 300-kHz (down-looking) and 1200-kHz (up-looking) RDI ADCPs. Triaxus profiled between 4 and 140 m depth with a vertical speed of 1 m s^{-1} and horizontal speed of roughly 3 m s^{-1}, providing horizontal resolution of 800 m near the top and bottom of the profiles and 400 m in the middle of the profiles. Shear from the Triaxus ADCPs was estimated via a technique similar to the inverse method for processing measurements collected with lowered ADCPs (Visbeck 2002). Shipboard ADCP near the surface was affected by instrument noise. Therefore, Triaxus shear is essential for capturing the near surface (4–30 m) velocity, where the majority of this analysis takes place.

The circular sampling pattern is well suited for calculating means and first derivatives of tracers and vector fields. The objective of the data processing is to project the frontal structure from Triaxus onto a transect traced by the float trajectory. Tracer and velocity data were averaged into 4-m vertical bins. Cross frontal sections were defined by density extrema (dense - east and light - west) for a total of 62 cross front transects. Loops were defined by two consecutive sections, and each section was included in two loops for a total of 61 loops. This was designed to average out fluctuations resulting from loop definition (see Fig. 3.2).

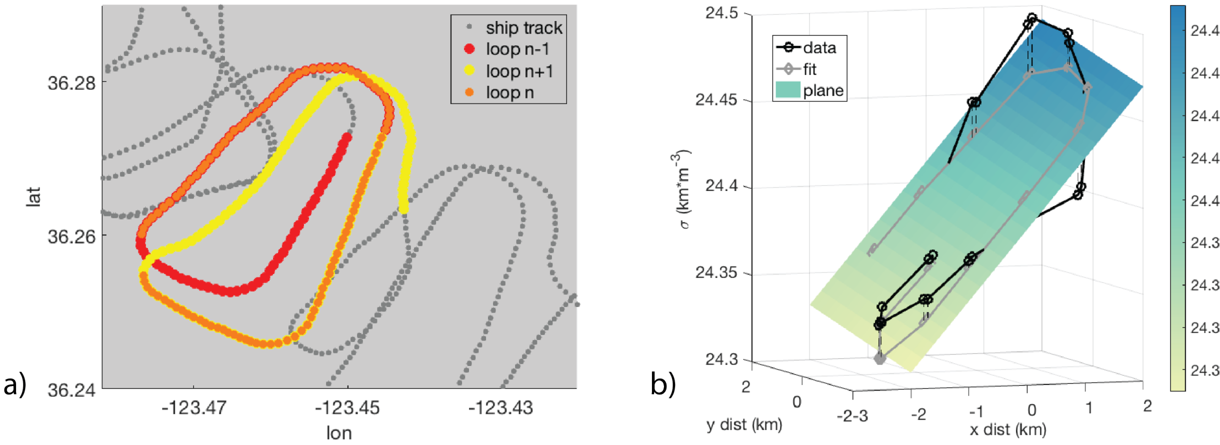

Fig. 3.2. a) Example of loops from underway data. A plane is fit to each loop, e.g. n–1, n, and n+1. Results from each loop are averaged together to form a single value for n. b) Example plane fit.

Data in each loop and each vertical level were applied to a plane-fit, z = Ax + By + C using a least squares estimate

$$\mathbf{F} = (\mathbf{X'X})^{-1}\,\mathbf{X'y} \qquad (3.1)$$

where **X** denotes position, **y** is the variable to be fit, and **F** contains the gradients (A, B) and averages (C). A 95% confidence interval (ϵ) associated with the least squares estimation is

$$\epsilon = c\sqrt{(\mathbf{X'X})^{-1}\left(\frac{1}{n}\sum_{i=1}^{n}(\mathrm{y}_i - \mathbf{x}_i\mathrm{F}_i)^2\right)} \qquad (3.2)$$

where *n* is the number of data points and *c* is the critical value determined from a Student's t-test. An example of σ for one loop, and associated F (Fig. 3.2b) shows a clear slope in the density field that is captured by the least squares plane fit. The results are smoothed further by averaging gradients and means with loops before and after (a total of 3) (Fig. 3.2a).

Gradients and means are used to calculate ζ, divergence, $\delta = u_x + v_y$, and strain $\alpha, = \sqrt{(u_x - v_y)^2 + (v_x + u_y)^2}$ (along with propagated errors), which are essential for characterizing the submesoscale. The result is a depth vs time (or along front distance) view of the water underneath the float as it is advected by the frontal flow. At times, it's more convenient to present results referenced to the frontal orientation. In this case, gradients and means are rotated locally based on direction of ∇b at 4 m, where positive implies along front (af) and down gradient (cross front, xf).

The survey pattern was also objectively mapped (Le Traon 1990; Bretherton et al. 1976) using correlation length scales Lx = Ly = 5 km (based on the approximate loop size) and a Gaussian covariance filter. Note that at times, particularly near the curve, a 5-km swath may contain up to five hours of data, highlighting the potential influence of time–space aliasing inherent in spatially smoothing such rapidly evolving fronts. Nonetheless, objective maps reveal essential qualitative information about the frontal structure. Throughout this thesis, results are presented primarily using the loop method outlined above, unless specified otherwise.

The float-following reference frame allows for a Lagrangian analysis of the front, where advective terms can be ignored and time changes are nearly $\frac{\mathrm{D}}{\mathrm{Dt}}$. This is only strictly true in layers that move in the advective frame of the float, an assumption that may not be valid as the front evolves. This can be assessed at each depth by integrating shear in depth from the location of the float, and in time, such that the cross front distance from the float is estimated dxf =

$\int_{t_o}^{t_i}\int_{z_j}^{z_o}\frac{\partial u_{xf}}{\partial z}\,dt\,dz$ (Fig. 3.3), where t_o is the beginning of the survey (yd 216.0) and z_o is the upper bin of triaxus data (4m) .

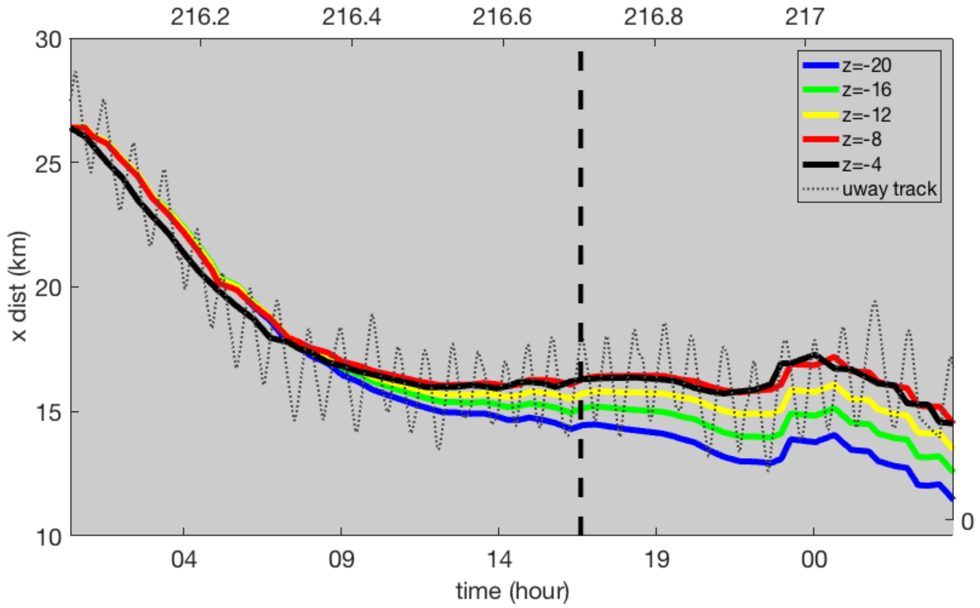

Fig. 3.3. Lagrangian analysis at depth. x distance is the cross frontal distance in the reference frame of the float trajectory toward the end of the survey (i.e., after the turn). Dashed line is the ship track, where each zigzag in time represents one loop. Colored lines are dxf integrated with shear from Triaxus. At yd=216.7 dxf implies that flow at 20 m is no longer true to the Lagrangian reference set at the beginning of the survey.

When dxf extends beyond the survey, the Lagrangian interpretation becomes obscured. For example, this happens at yd = 216.7 at 20 m. After this time, that layer of the survey cannot be interpreted as Lagrangian and advective terms may not be ignored. Flows near the surface (i.e., <12 m) are Lagrangian throughout most of the survey.

3.3 SCALE RESOLUTION

The submesoscale transition is energized near the surface (Callies and Ferrari 2013; Lapeyre and Klein 2006) and characterized by small sharp gradients of buoyancy and velocity with typical length scales of O(1–10 km) that evolve on an inertial timescale. Resolving these space and time fields presents an observational challenge. The significance of resolving different scales can be readily seen by comparing tracers, velocities, and their respective gradients resolved by AVISO, the mesoscale survey and the Lagrangian survey (Table 3.1).

Table 3.1. Values for scalars, velocities, and their gradients resolved at different observational scales

	AVISO	SEASOAR	TRAIXUS	FLOAT
SCALES	>100 km	12 km	5 km	1 m
δ	$0.001 f\,\mathrm{s}^{-1}$	$0.03 f\,\mathrm{s}^{-1}$	$0.7 f\,\mathrm{s}^{-1}$	-
ζ	$0.03 f\,\mathrm{s}^{-1}$	$0.15 f\,\mathrm{s}^{-1}$	$0.7 f\,\mathrm{s}^{-1}$	-
α	$0.10 f\,\mathrm{s}^{-1}$	$0.13 f\,\mathrm{s}^{-1}$	$1.2 f\,\mathrm{s}^{-1}$	-
$\nabla_h b$	-	0.32e–6 s^{-2}	1.4e–6 s^{-2}	-
KE	0.12 $\mathrm{m}^2\,\mathrm{s}^{-2}$	0.27 $\mathrm{m}^2\,\mathrm{s}^{-2}$	0.27 $\mathrm{m}^2\,\mathrm{s}^{-2}$	-
w	-	5 m s^{-1}	20 m s^{-1}	50–100 m s^{-1}

Objective maps of surface density from the mesoscale and Lagrangian surveys exhibit differences in intensity, structure, and position of the same front observed within 30 hours of each other (Fig. 3.4). The surveys align initially, with a similar cross frontal gradient and direction. This changes later in the survey as contours of the front between the two surveys diverge and wavelike meanders resolved by the Lagrangian survey are smoothed by the mesoscale survey.

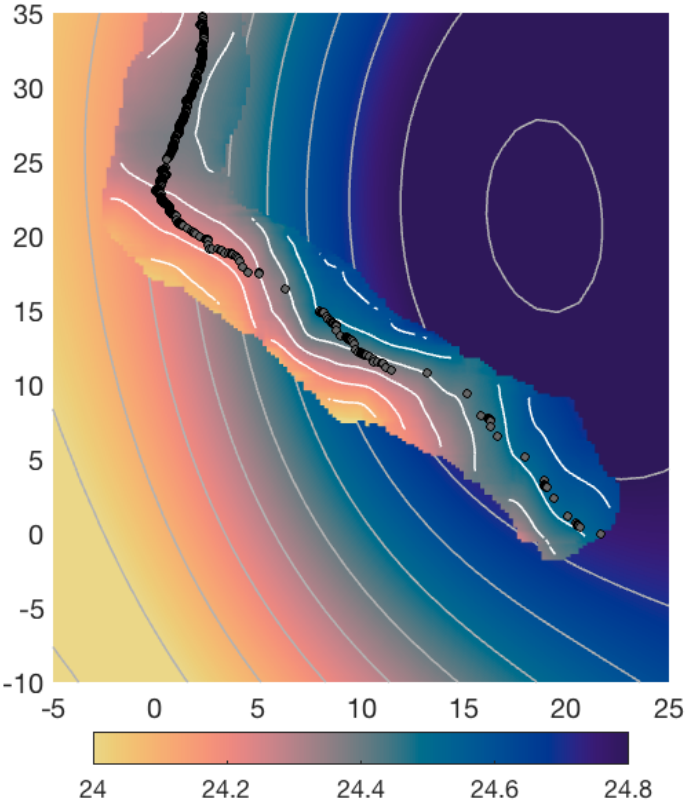

Fig. 3.4. Objective maps of near surface σ for mesoscale survey (16 m, background), and Lagrangian survey (4 m, foreground). Contours outline isopycnals every 0.1 kg m^{-3}. Grey dots track the float location. x-axis and y-axis are distance in km.

Note that one ~10-km wavelength meander was resolved in <10 hr in the Lagrangian survey, faster than the local inertial period, $T_i = \frac{2\pi}{f} = 20.3$ hr. This suggests the meanders are either small scale physical features or superinertial motions and not associated with aliased tides or inertial motions targeted to be filtered by objective map correlation length scales used for mesoscale surveys (Rudnick 1996; Pallàs-Sanz et al. 2010b).

Magnitudes of tracers and velocity gradients are largest in the Lagrangian survey, commensurate with higher spatial resolution (Table 3.1). This can be seen qualitatively as isopycnals in the Lagrangian survey squeeze together (Fig. 3.4) compared with the mesoscale survey. The sharper front in the Lagrangian survey is consistent with sharper gradients of velocity that induce ζ, δ, and α, of O(f). Higher resolution naturally allows for greater derivatives as the denominator decreases. But the implications here are not trivial as an increase in gradients and energy at smaller scales isn't predicted by a classic QG framework used to describe the mesoscale. Lower estimates of ζ, δ, and α at larger spatial scales are not simply a result of the smoothed submesoscale field, but are ultimately associated with different dynamics linked together. For example, α estimated from AVISO results from the mesoscale eddy field that acts to stir gradients at the surface and squeeze this front together, an essential ingredient for the submesoscale that is absent in classic QG. On top of this background flow is a submesoscale α implying local processes acting to strain the front (Fig. 11b). Finally, the deviation between the two surveys illustrate the time space aliasing challenges of observing the rapidly evolving submesoscale and need to be considered when interpreting the data.

The Lagrangian survey clearly illustrates the importance of resolving small scales. Highly localized gradients are an important feature of the submesoscale and begin to hint that processes associated with Ro O(1) dynamics may be acting at this front.

3.4 FRONTAL EVOLUTION

The initial Triaxus transect revealed the vertical structure of this surface intensified submesoscale front above a pycnocline of 30 m. The entire front was broad with horizontal changes in density of $\Delta\sigma = 0.9$ kg m^{-3} over 20 km, with evidence of sloping isopycnals deep into the interior down to 150 m. Imbedded in the broad buoyancy gradient is a sharper front with $\Delta\sigma$ of 0.21 kg m^{-3} over 2 km between the 24–24.4 kg m^{-3} isopycnals (Fig. 3.5) with a $\nabla_h b = 1\times10^{-6} s^{-2}$.

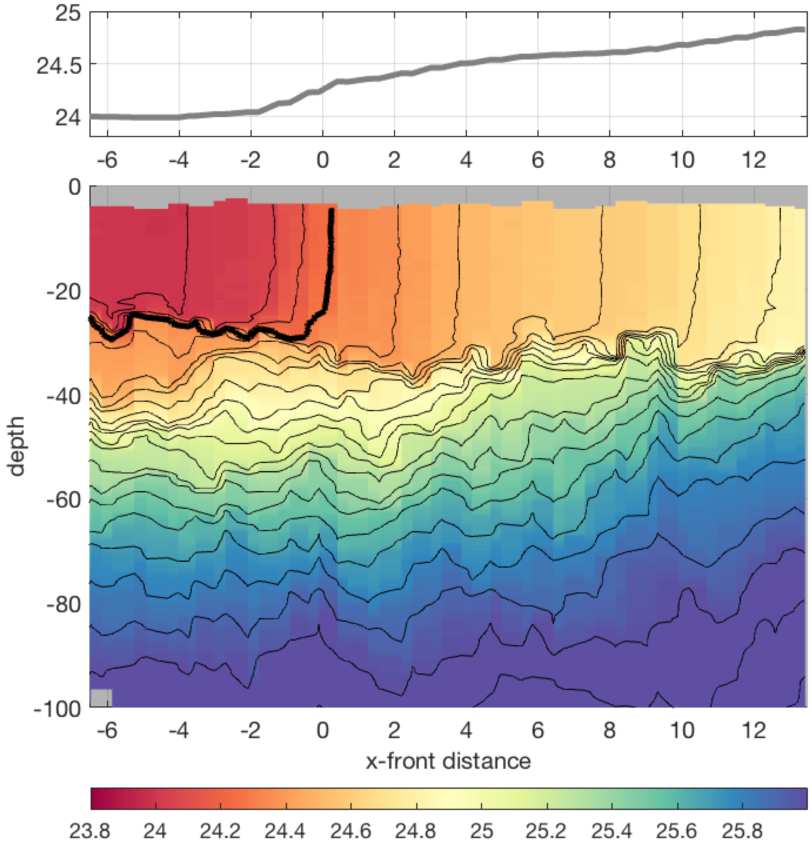

Fig. 3.5. Initial transect used to identity the front before placement of the float. Top: cross frontal σ [kg m^{-3}] from the ship flow through system. Bottom, cross frontal σ [kg m^{-3}] from Triaxus. Black lines are contours of σ= 0.1 kg m^{-3} and the dark black line is σ = 24.4 kg m^{-3}.

This sharper portion of the front became the target of the Lagrangian survey. Note the entire frontal extent is not captured by the 3–5-km loop sampling pattern aimed to focus on the sharpest part of the front. The frontal evolution can be divided into three stages. Stage 1: Downfront winds and turbulent mixing in the BL. Stage 2: Diurnal warming and frontal slumping. Stage 3: Nighttime surface forcing, rapid near surface stratification, three dimensionality, and float subduction (Fig. 3.6).

Stage 1 (yd 216–216.3): Northerly winds that began five days prior had peaked at 0.5 N m^{-2} 18 hr before the start of the survey. Stage 1 began with a 0.23 N m^{-2} down front wind stress that decreased to 0.04 N m^{-2} within 6 hr. The float was placed slightly dense (east) of the front at the 24.3 kg m^{-3} isopycnal and began traveling west towards the light side of the front. During this time, the sharpest part of the front was only partially resolved. Isopycnals in the upper 30 m, (hereinafter referred to as the ML for simplicity), are steep as the upper ocean was vertically homogenous with strong horizontal gradients of buoyancy (Fig. 3.7).

Stage 2 (yd 216.3-216.8): The heat flux changed from cooling to warming and the wind remained between 0–0.02 N m^{-2}. The float was trapped between 1–2 m such that the float's antennae was just below the surface, suggesting a cessation of turbulent mixing (Fig. 3.6). The float trajectory slowed down and began to veer shoreward (east) (e.g., Fig. 3.4). At this time, and for the remainder of the survey, the float and shipboard survey began to resolve the sharpest part of the front between 24–24.2 kg m^{-3}. During this stage, horizontal isopycnals that define the front squeezed closer together as the front intensified (e.g., Fig. 3.4, section 3.4c), sped up, and simultaneously began to tilt and stratify the waters above the pycnocline (Fig. 3.4, Fig. 3.5, Fig. 3.7, section 3.4b).

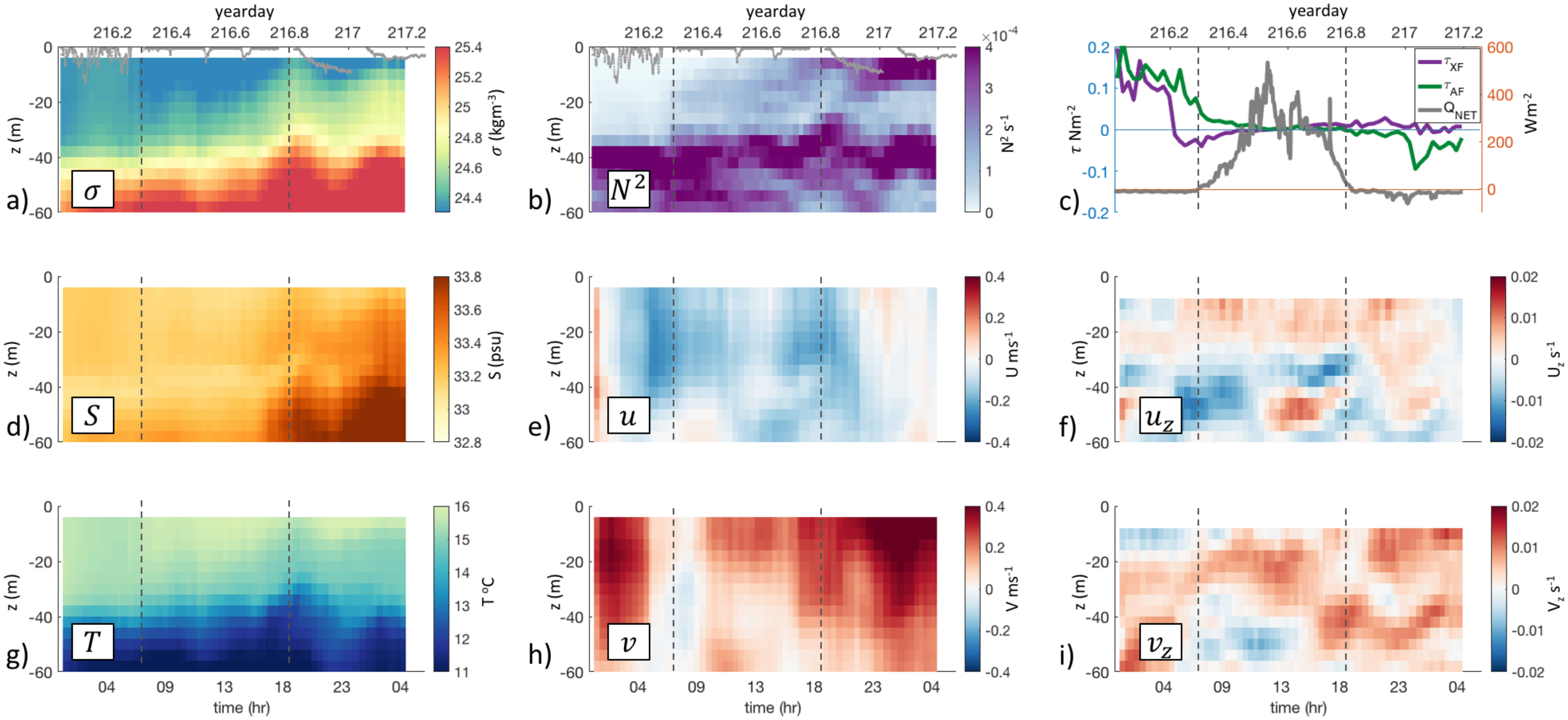

Fig. 3.6. – Scalars and velocity of the front underneath the float throughout the Lagrangian survey. a) σ and float depth (grey dots); b) N^2; c) along front wind stress (green) and across front wind stress (purple), Q_{NET} (grey); d) salinity; e) *u* velocity; f) shear u_z; g) temperature; h) *v* velocity; and i) shear v_z. Dashed grey lines denote the three stages outlined in section 3.4.

Stage 3 (yd 216.8–217.3): The heat flux changed from net warming to cooling, and wind speed increased to 0.09 N m^{-2} and rotated to an upfront orientation (Fig. 3.6). Along front wavelike meanders appeared in the survey and the float downwelled along isopycnals. In the classic 1D view, nighttime cooling and winds would erode the daytime stratification (Price et al. 1986). Here, stratification in the near surface layer strengthened as warm fresh water slid over the cold salty side of the front (Fig. 3.6 Fig. 3.7, and section 3.4c).

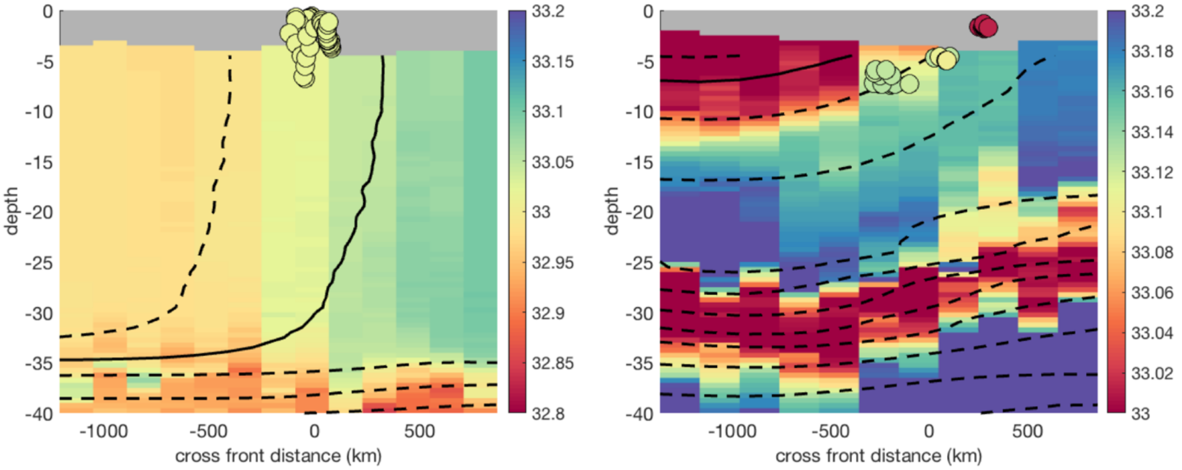

Fig. 3.7. Raw Triaxus data salinity during a) stage 1, yd 216.1 and b) stage 3, yd 216.8. Black dashed lines are 0.1 σ contours and solid line marks the 24.3-kg m^{-3} contour. Circles denote the position of the float within ±15 min of the transect and are colored in average salinity of the float sensors.

The remainder of this thesis aims to detail the frontal evolution. It is shown that ageostrophic circulation contributes to ML stratification and a downscale of energy.

3.4.1 *Vertical shear and thermal wind (im)blanace*

Thermal wind balance requires

$$\frac{\partial u_g}{\partial z} = -f\frac{\partial b}{\partial y} \quad (3.3)$$

Ageostrophic shears are largest in the mixed layer and are a similar magnitude as geostrophic shear (Fig. 3.8). During stage 1, strong upfront shear was prominent throughout the ML and acted against the geostrophic shear such that total shear was near zero. Near the surface, the upfront ageostrophic shear attenuated gradually throughout the survey, suggesting the front may have been close to a state of thermal wind balance by the end of the survey. In the middle of the ML, along front shear approached geostrophic shear as turbulent mixing subsided.

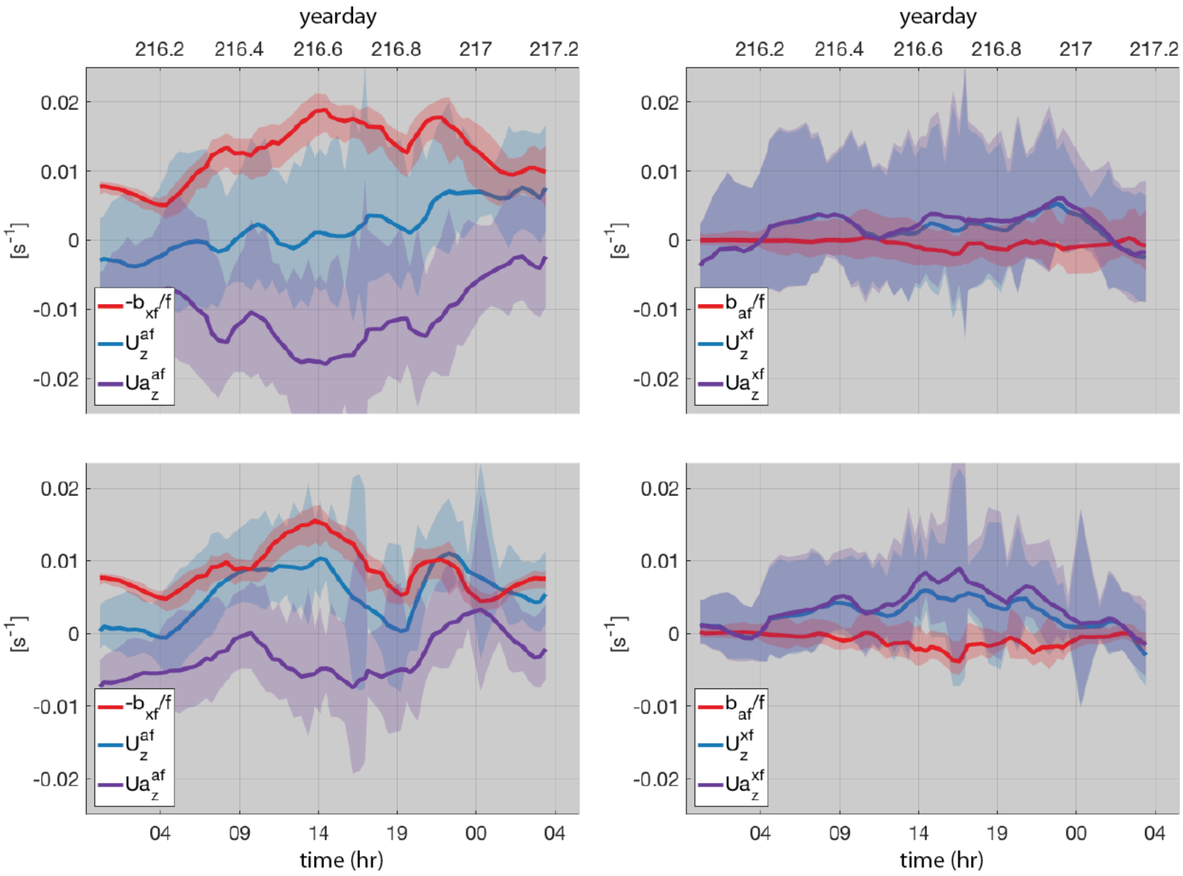

Fig. 3.8. Geostrophic shear, ageostrophic shear, and total shear for a) u_{af} at 8 m, b) u_{xf} at 8 m, c) u_{af} at 16 m, d) u_{xf} at 16 m. All terms have been rotated to align with ∇b at 4 m (section 3.2). Shaded regions are error (ϵ).

Ageostrophic xf shear was near zero during stage 1 suggesting uniform momentum throughout the ML. During stage 2, an ageostrophic circulation developed as xf shear increased gradually and then decreased towards zero towards the end of the survey. It is shown this is instrumental at differentially advecting buoyancy across the front.

3.4.2 *Stratification*

The evolution and distribution of stratification throughout the mixed layer points to the importance of lateral processes. This is seen in the different cross frontal structures of salinity between the beginning and end of the the survey (Fig. 3.7) and the horizontal spreading of the 24.4 isopycnals at different depths as the front tilts over (Fig. 3.9). The distribution of the stratification was not uniform as deeper layers began to stratify earlier than the surface layers (Fig. 3.7, Fig. 3.9).

Differential advection by vertical shear creates stratification. The rate can be approximated as

$$\frac{\mathrm{D}C_z}{\mathrm{D}t} = -C_x u_z - C_y v_z \qquad (3.4)$$

for C representing tracers T, S, b. This was calculated at 8 m, where the survey was considered Lagrangian and where shear could be estimated by center-finite-difference (Fig. 3.10). The ability of the cross front shear to predict vertical gradients signifies that most of the changes in N^2, $\partial \mathrm{T_z}$, and $\partial \mathrm{S_z}$ can be attributed to processes that differentially advect tracers across the front. This analysis holds at 16 m while that depth is Lagrangian in the survey (not shown).

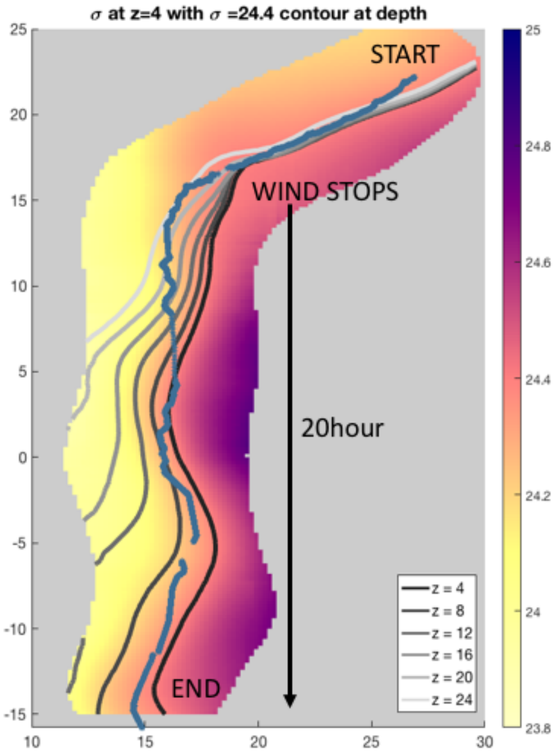

Fig. 3.9. Objective map of σ at 4 m. Map has been rotated to follow the float trajectory (blue dots) during stages 2 and 3. The grey scale lines denote the 24.4 contour at different depths.

Radiative heat fluxes can also influence temperature near the surface and hence stratification. Contributions of horizontal (frontal slumping) and vertical (solar warming) processes on N^2 can be represented in terms of changes in T and S assuming a linear equation of state, $\rho = \rho_o g\left(-\alpha(T - T_o) + \beta(S - S_o)\right)$, such that

$$N^2 \approx g\left[\alpha \frac{\partial T_v}{\partial z} + \alpha \frac{\partial T_h}{\partial z} - \beta \frac{\partial S_h}{\partial z}\right] \qquad (3.5)$$

where $\alpha = 2.0\times10^{-4}\mathrm{K}^{-1}$ is the thermal expansion coefficient for seawater and $\beta = 7.5\times10^{-4}\mathrm{psu}^{-1}$ is the haline contraction coefficient for seawater.

Vertical changes in T due to radiative heating, $\frac{\partial T_v}{\partial z}$, are difficult to estimate without a knowledge of the background mixing. Yet, one may be able to estimate vertical changes in *T* due horizontal slumping on ($\frac{\partial T_h}{\partial z}$) using knowledge of the horizontal density structure. This is done using a density ratio that captures the relative influence of *T* and *S* on changes in density.

$$R = \frac{\alpha \Delta T}{\beta \Delta S}. \qquad (3.6)$$

During adiabatic slumping of isopycnals, horizontal changes in *T* and *S* (R_H) are converted into vertical ones (R_V). Assuming that *S* is a passive tracer (therefore $\frac{\partial S_h}{\partial z}$ is observed entirely) and *R* is conserved during this process (i.e., $R_H = R_V$), then (Fig. 3.10b)

$$\frac{\partial T_h}{\partial z} = \frac{\beta}{\alpha} R_H \frac{\partial S}{\partial z} \qquad (3.7)$$

where $R_H = \frac{\alpha \nabla T}{\beta \nabla S}$. At 8 m, 80% of the vertical changes in *T* can be explained by $\frac{\partial T_h}{\partial z}$ and can be attributed to frontal tilting. From this, one can estimate N^2 due to $\frac{\partial T_h}{\partial z}$ and $\frac{\partial S_h}{\partial z}$ using 3.5 (Fig. 3.10a). N^2 estimated from eq. 3.4 and using the horizontal terms in eq. 3.5 both suggest that the increasing stratification at this front was due to lateral advection and is a major result of this study.

The horizontal tilting of isopycnals induced a vertical stratification that may be used to estimate an equivalent vertical flux of buoyancy,

$$(w'b') = \frac{d}{dt} \iint_{-H}^{0} N^2 \partial z \partial z \qquad (3.8)$$

Integrating N^2 from $H = 30$ m gives $w'b' = 9.8\text{x}10^{-7}$ m^2 s^{-3} and a heat flux equivalent, $Q_{eq} = \frac{c_p \rho}{g \alpha}(w'b')$, of $Q_{EQ} \sim 2000$ Wm^{-2}. This is an order of magnitude larger than the average heat flux onto the ocean surface during this stratification $Q_{avg} \sim 100$ Wm^{-2}.

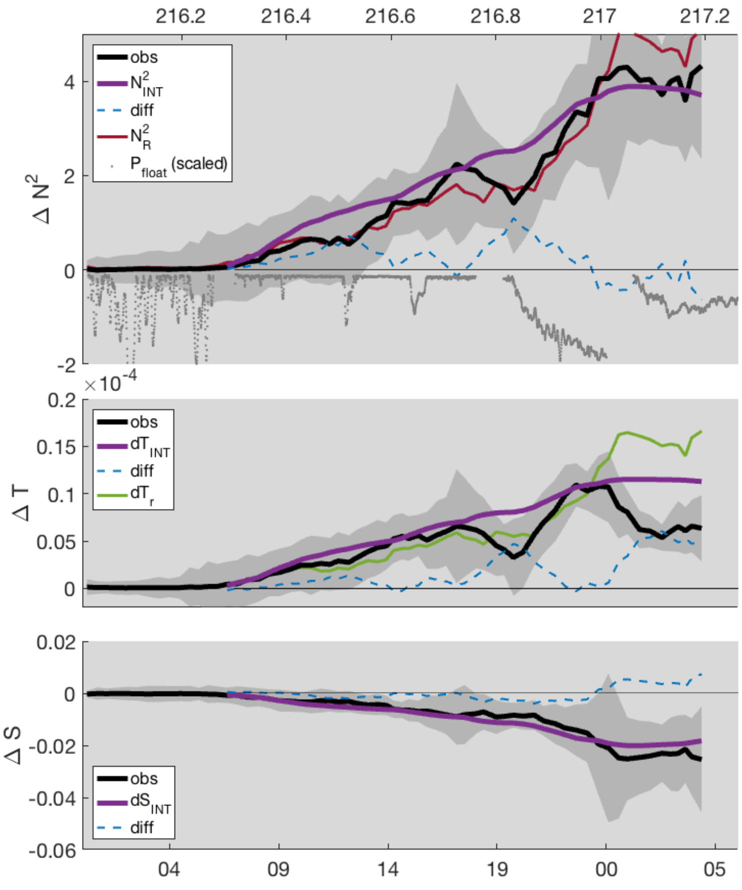

Fig. 3.10. From top to bottom: a) N^2, b) ΔT, c) ΔS at 8 m. Black lines are observations, purple lines are integrated values from eq. 3.4. Blue dashed lines are the difference between the observations and integrated values. Purple line in a) is N^2 from eq. 3.5 using $\frac{\partial T_h}{\partial z}$ and $\frac{\partial S_h}{\partial z}$. Green line in b) is $\frac{\partial T_h}{\partial z}$. Scaled float depth is included in a) for reference. Shaded regions are error (ϵ).

3.4.3 *Horizontal buoyancy gradient, strain, vorticity, and divergence*

Estimates of ∇b using the loop method outlined in section 3.2 were largest near the surface and decay with depth by a factor of 0.4 over 20 m (Fig. 3.11d).

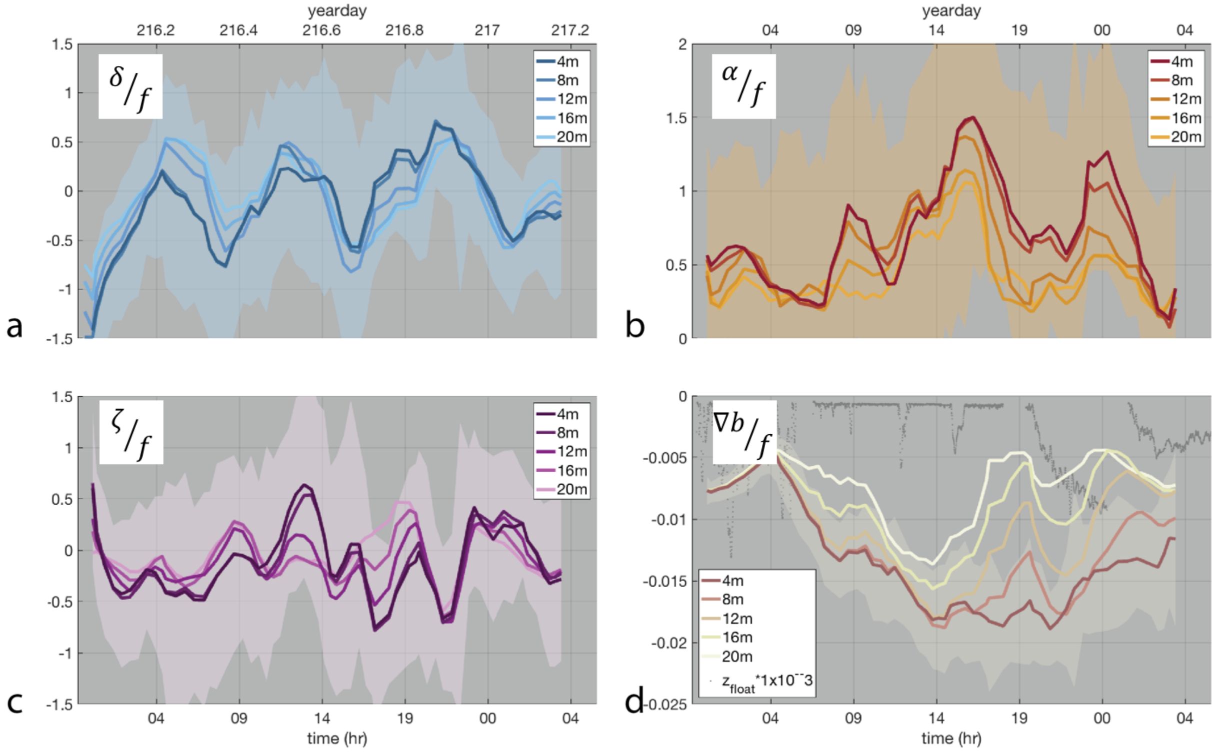

Fig. 3.11. (a) δ/f, (b) α/f, (c) ζ/f , and (d) $\nabla_h b$ plotted against time at depths 8–20 m. Float depth scaled by x10^{-3}. (b) Included to provide reference for frontal evolution. Shaded regions are error (ϵ).

Near the surface, this can be estimated at higher resolution from the ship underway system assuming $\nabla b_s = \left|\frac{\Delta b_s}{\Delta s}\right|$, where Δb_s and Δs are changes in the along shiptrack direction (Fig. 3.12). Along track estimates were greater by a factor of 1.7, as gradients revealed by the flow through system (Δs~100 m) were not fully resolved by Triaxus (Δs ~800 m).

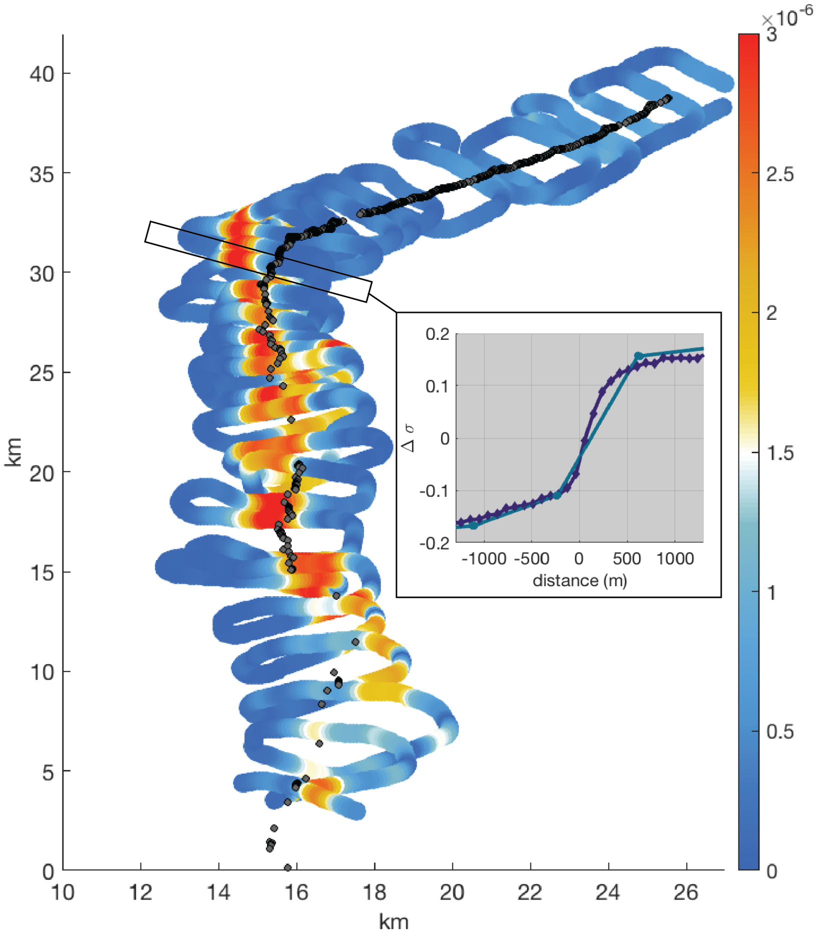

Fig. 3.12. a) ∇b_s calculated along track from the ship underway. b) example of a cross front transect of σ resolved by the underway (purple) and Triaxus at 4 m (blue).

Recall the survey only partially resolved the sharpest part of the front during stage 1. At the onset of stage 2, the front was fully resolved thus this analysis begins at the start of stage 2. The float was trapped at the surface, implying a decrease in turbulent mixing. The front continued to strengthen by a factor of 2 reaching $>2\text{x}10^{-6}\text{s}^{-2}$ at the surface (underway along track) within 12 hr. Throughout stages 2 and 3, the frontal structure fluctuated from a tight and organized front to a broad, sometimes fragmented front with multiple jumps in buoyancy gradient (Fig. 3.12). Never throughout the survey did the front become sub-resolution (i.e., smaller than 100 m), and generally maintained a frontal width of 600 m, smaller than the deformation radius $L_D = \frac{NH}{|f|}$ of 5 km.

Vorticity, ζ, and divergence, δ, both approach O(*f*). Similar to strain, α, and $\nabla_h b$, values were greatest near the surface and decayed with depth. During stage 1, ζ changed throughout the mixed layer, approaching –*f* at z = –4, then increased with depth by about 0.5*f* over 20 m. This is in contrast with ∇b, which suggests a homogenization of tracers. ζ was negative during the transition into stage 2 despite the fact that the float took a cyclonic turn in the observations. This presents a discrepancy between the apparent spatial direction of the flow and the local horizontal shear. From stage 2, ζ was uniform throughout the mixed layer and oscillated between +/– 0.5*f*. These oscillations can be tied to frontal meanders (e.g., Fig. 3.4). δ during stage 1 was consistently negative throughout the ML. During stage 2, δ became surface intensified and oscillated between strong convergences and divergences.

The horizontal buoyancy gradient was tied to α and therefore ζ and δ. A background strain field estimated from the mesoscale survey to be 0.3*f* (Pallàs-Sanz et al. 2010b) was attributed to eddies in the surrounding mesoscale field. On top of this background strain, O(*f*) strain was resolved by the Lagrangian survey (Fig. 3.12) that was particular to the local dynamics around the front, and was not captured by the mesoscale survey or AVISO. The relationship between α and ∇b can be seen in the advective terms of the frontogenetic tendency equation (Fig. 3.13)

$$F = \frac{D|\nabla_h b|^2}{Dt} = \left(-b_x \nabla_h u - b_y \nabla_h v\right) \cdot \nabla_h b \qquad (3.9)$$

The advective component of *F* was near zero during stage 1, but began to fluctuate as the front evolved. The low value of *F* during stage 1 can be attributed to the survey not completely resolving the front during that time. During stages 2 and 3, increases in *F* are consistent with a strengthening of $\nabla_h b$ (Fig. 3.11, Fig. 3.12, Fig. 3.13) accompanied by a tilting of isopycnals and deterioration of the frontal integrity near the surface.

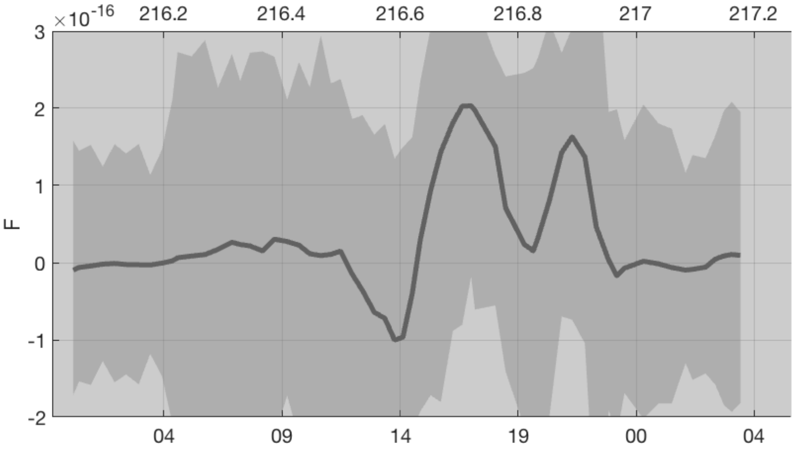

Fig. 3.13. Frontogenetic tendency as a function of time F at z = 8. Shaded regions are error (ϵ).

Additionally, this evolution was associated with a local strain field with large divergences. Combined these imply highly localized, non-QG dynamics were acting on this front and contributed a downscale of tracers and energy to smaller scales.

3.4.4 *Vertical velocity*

The float measured P every 30 s, allowing for direct measurements of vertical velocity. To minimize high-frequency motions from the float, a line was fit to 30 min of data, such that the slope provided an estimate $w = \frac{-dP}{dt}$. During stages 1 and 2 the float was ballasted buoyant and adjusted again before stage 3. This becomes relevant in interpreting the float behavior.

During stage 1, the float traversed the upper ~10 m of the ML reaching w=7x10^{-3} m s^{-1}. During the 6-hr period of mixing the float measured increasingly dense, cool, and salty water, despite the fact that it moved towards the light side of the front. This may be consistent with symmetric instability dynamics (Thomas et al. 2016) and is not addressed here.

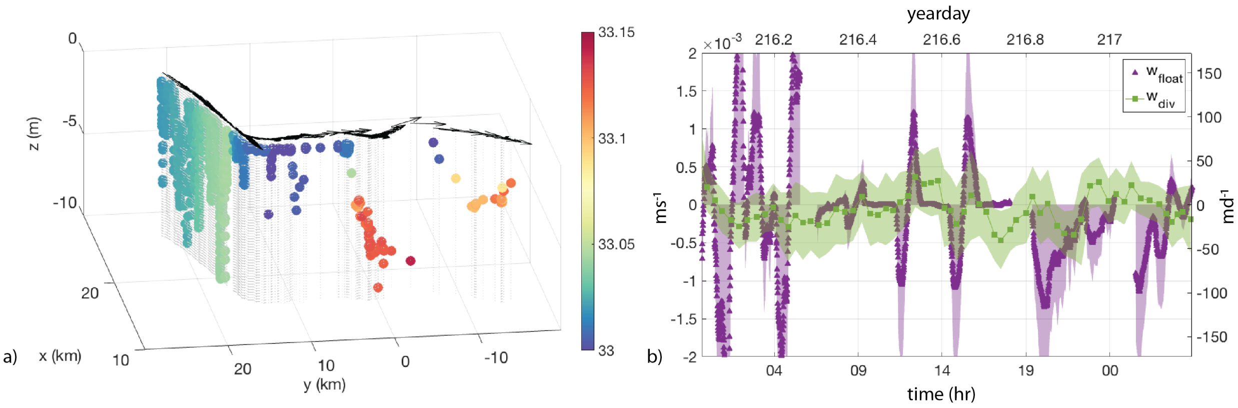

Fig. 3.14. a) Circles denote float location and are color coded in salinity. Arrows at surface are float velocity vectors. Each float location and velocity vector is connected by a thin grey line. b) vertical velocity estimated directly from float (purple) and from Triaxus (green).

During stages 2 and 3, the float observed four downwelling events (I–IV on Fig. 3.14). In all cases, the float mixed diabatically (seen as changes in *S* in Fig. 14a) as it downwelled under the light side of the front (Fig. 3.15). I and II (stage 2) occurred after the float completed the turn and while heat flux was warming (positive). The shallow extent of the downwelling events (4–6 m) may be attributed to the float programmed buoyant. Before stage 3, the float was reprogrammed, allowing it to obtain a deeper extent of downwelling to ~10 m. During events III and IV, the float became isopycnal below 4 m as it continued to be advected adiabatically by the frontal circulation. The largest of these events was III and is discussed in detail.

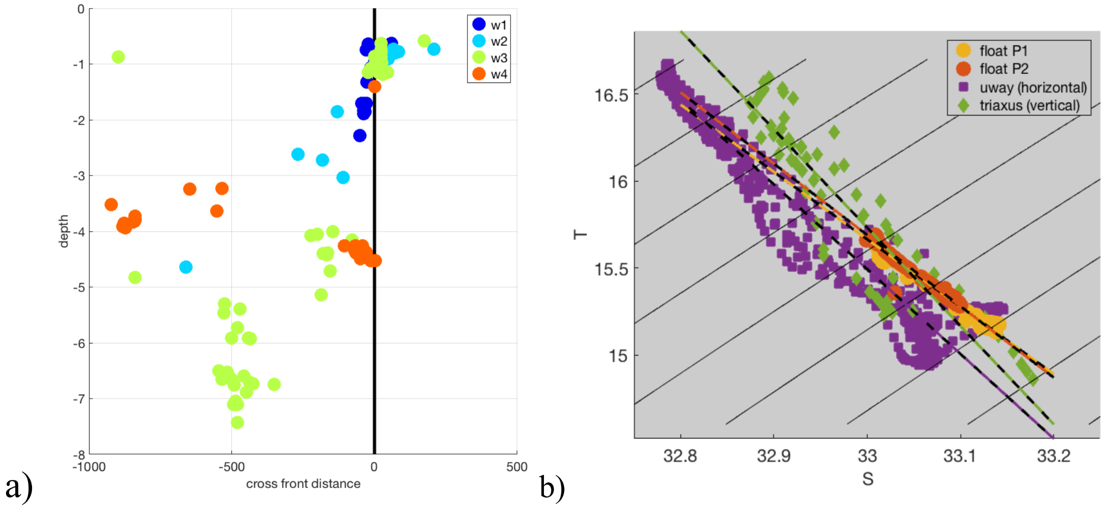

Fig. 3.15. a) Cross frontal distance of float as it downwelled under the front during I–IV. b) TS diagram during downwelling events III. Float and Triaxus represent the TS of the vertical stratification, while the ship underway provides TS of the horizontal stratification.

At yd 216.8 the float approached the trough of a cyclonic meander. The float's horizontal velocity slowed down as the float sank at 1.3 m s^{-1} (120 m d^{-1}) across and under the warm side of the front (Fig. 3.15a, Fig. 3.7b). This occurred as the heat flux changed to cooling. In a turbulent boundary layer (BL), the float would traverse the BL with N^2~0, similar to stage 1. Here, the float's density changed simultaneously (became denser) and stratification increased (diapycnal) as the float travelled through vertical changes in both temperature and salinity. (Fig. 3.14a, Fig. 3.7b). The stratification measured by the float during this downwelling event shared a TS space with the horizontal stratification estimated from the ship flow through (Fig. 3.15b). This is strong evidence that vertical stratification was a result of tilting isopycnals and not solely from solar forcing, consistent with budgets in section 3.4b.

Below 4 m, the float's density remained constant as it continued to downwell at w=0.7x10^{-3} m s^{-1} (~60 m d^{-1}). During this time, the float was caught in the flow of an anticyclonic meander crest as it wrapped westward (Fig. 3.14a). Throughout the meander, the float's vertical velocity slows, nearing zero. At yd 217 the float is automatically set to profile and is ejected from the secondary circulation cell.

The downwelled float in III occurred on the upstream side of a meander trough (Fig. 3.14a, Fig. 3.4), consistent with a transition to cyclonic flow, $\zeta > 0$, associated with $\delta < 0$. This geometry of downwelling with respect to frontal meanders was consistent with previous examples observed in a larger frontal system (e.g., Bower and Rossby 1989; Thomas and Joyce 2010). Here, ζ and δ are O(*f*) suggesting a departure from the non-divergent framework usually adopted for larger frontal systems.

Vertical velocity at fronts is generally estimated through a PV framework in the form of an omega equation. This is particularly well suited for larger surveys where divergence estimates are smaller than error in velocity measurements. The relatively small width of the survey pattern is sufficient for single derivatives, but not for the double derivatives needed to invert the omega equation. Instead, the small extent of the survey allowed for resolution of δ O(*f*), which can be used to estimate vertical velocity (assuming a rigid lid w=0)

$$w_\delta = \int_{z=-8m}^{z=0m} \delta dz \qquad (3.10)$$

During III, w_δ predicted downwelling, but greatly underestimated the vertical velocities experienced by the float (Fig. 3.14b). This suggests a highly localized region of downwelling at the front that could not be resolved by the 5 km distances through which δ estimates are calculated. This highly localized vertical velocity is reminiscent of the increase in $\zeta, \alpha,$ and δ presented in Table 3.1, which are features of the submesoscale in general.

3.4.5 *Potential vorticity*

Ertel potential vorticity (PV) captures the projection of vorticity on buoyancy surfaces, defined as

$$q = \omega \cdot \nabla b, \qquad (3.11)$$

where $\omega = (f\hat{\mathbf{z}} + \nabla \times u)$. It is a dynamically relevant tracer and is conserved following fluid parcels unless subject to external forcing, such that

$$\frac{Dq}{Dt} = 0 \qquad (3.12)$$

In the absence of forcing and horizontal density gradients, PV conservation is balanced by terms in the vertical component of PV

$$q_V = (f + \zeta)\mathrm{N}^2. \qquad (3.13)$$

Near fronts the horizontal (or baroclinic) terms are leading order and become important contributors to a fluid parcels PV. Neglecting derivatives in vertical velocity, the baroclinic term can be written in along front and across front components

$$q_H = u_{af} b_{xf} - v_{xf} b_{af}. \qquad (3.14)$$

If the shear is purely geostrophic, then the baroclinic term becomes

$$q_{HG} = \frac{-\,{b_{xf}}^2}{f} \qquad (3.15)$$

a negative definite quantity in the Northern Hemisphere that acts to oppose q_V. The presence of ageostrophic shears and surface forcing, which are often crucial to momentum and buoyancy budgets in the ML, can influence both q_V and q_H.

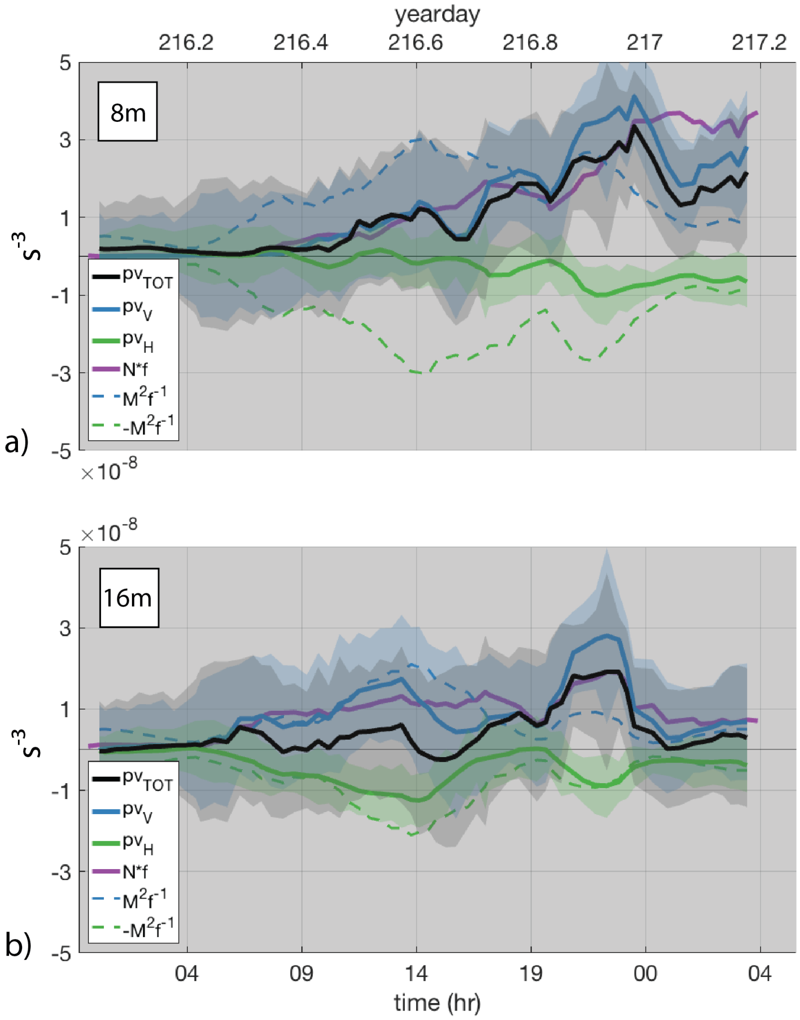

Fig. 3.16. Potential vorticity (black line) and its components (vertical – blue, horizontal – red) for a) 4 m and b)16 m. Both plots also include planetary PV (purple) and thermal wind balance (black dashed lines). Shaded regions are error (ϵ).

Here, the evolution of PV (Fig. 3.16) exhibits two different stories: a deeper layer (16 m) where PV is conserved near zero lying underneath a surface layer of increasing PV (4 m). The components of PV are used to describe this evolution. (Thomas 2008) laid out three conditions under which PV at fronts can have near zero PV;

i) Vertically mixed momentum and buoyancy to create N^2=0 and v_z=0;

ii) Vortically low PV as $\zeta \rightarrow f$

iii) Baroclinically low PV

In the beginning of the survey, BL turbulence homogenized tracers and momentum throughout the ML. This caused a lack of shear and stratification that resulted in close to zero q_V and q_H as in (i). Both terms were smaller than the value associated with geostrophic balance and consistent with large ageostrophic shears (Fig. 3.9, section 3.4a).

At the start of stage 2, the surface and deep PV evolved differently. Deeper in the ML (16 m), isopycnals began to tilt, causing the once homogeneous ML to stratify and q_V to increase. The tilting of isopycnals (e.g., Fig. 3.8) was accompanied by an increase in both horizontal buoyancy gradient and vertical shear such that q_H compensates q_V as in (iii). This resulted in near zero PV as long as the flow was Lagrangian (yd 216.7) after which advective terms may become important and interpretation is elusive (see section 3.2, Fig. 3.3). Changes in q_V and q_H tracked M^4/f, demonstrating the balanced state of the front during this time.

The near surface layer did not experience the same PV conservation. During stage 2, q_V increased with stratification. During stage 3 q_V remained level and decreased slightly as the increase in stratification at the end of the survey was offset by a decrease in ζ as in (ii) and consistent with the anticyclonic meander. Unlike the middle of the ML, changes in q_V were not balanced by q_H. Horizontal buoyancy gradient increased, yet strong upfront shear inhibited development of q_H. Furthermore, the presence of ageostrophic cross front shear encouraged frontal tilting (Fig. 3.9) and increased stratification. This cross front shear did not contribute to q_H because $\nabla_h b$ along front is, by definition, zero. This reveals the importance of ageostrophic shear in modulating PV in the BL.

3.5 BUOYANCY FLUX SCALINGS

Processes thought to be leading order at enhancing stratification at submesoscale fronts are often represented as a vertical flux of buoyancy $w'b'$ which can be directly linked to the energetics of the system and the stratification.

Table 3.2. Description of processes that may influence stratification at a front.

Name	$w'b'$	Description	Reference
Geostrophic Stress	$0.05\frac{\nabla_h b^2 H^2}{f}$	Circulation response to turbulence at front	Wenegrat et al. 2018
Mixed Layer Eddies	$0.06\frac{\nabla_h b^2 H^2}{f}$	Baroclinic instability of mixed layer front	Fox Kemper et al. 2008
Ekman Buoyancy Flux	$\frac{\tau\times\nabla_h b^2}{\rho f}$	Ekman induced transport across the front	Thomas and Lee 2005
Near Inertial Oscillation	$U_{NIO}\nabla_h b$	Near inertial transport across front	Savelyev et al. 2017
Heat Flux	$Q\frac{\alpha\rho}{c_p g}$	Vertical input of heat at surface	N/A

These $w'b'$ scalings are derived from a combination of theory and idealized modeling, and are usually presented in observationally accessible state variables. This allows the restratifying/destratifying effects of these processes to be compared with each other and with surface radiative heating/cooling. A brief description of several processes and their associated *w'b'* scaling are included in Table 3.2. A more in depth discussion can be found in McWilliams (2016) and references in Table 3.2.

These scalings are calculated using $\nabla_h b, \tau,$ from the observations (i.e., Fig. 3.6), an H = 30 and ρ_o =1024. U_{NIO} is calculated similar to Savlyev using observed winds (Fig. 3.17).

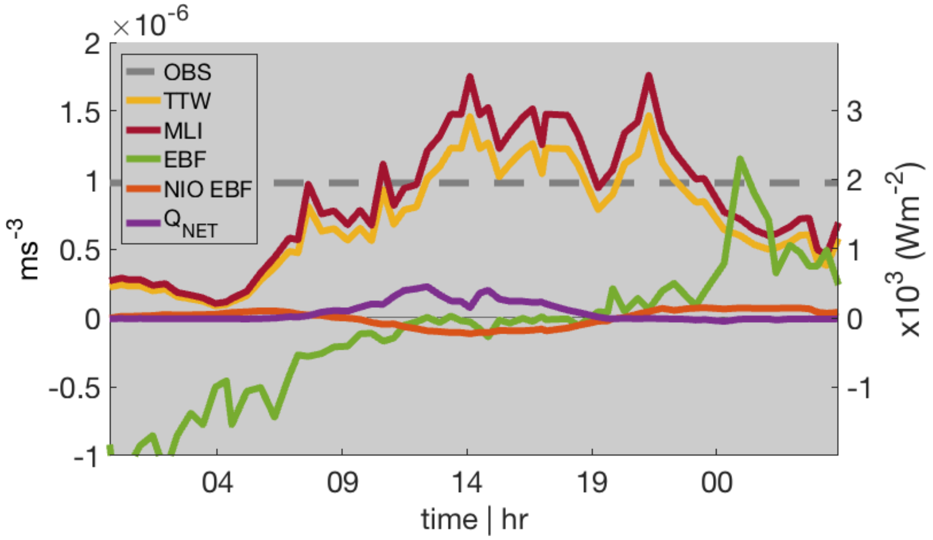

Fig. 3.17 *w'b'* scalings estimated from observationally derived parameters.

MLE and TTW are practically identical with values reaching 3000 W m^{-2}. Wind driven near inertial oscillation transport and surface heat flux are orders of magnitude less at ~100Wm^{-2}. EBF suggests the importance of down front winds in the beginning of the survey and upfront winds towards the end. Observed *w'b'* from lie in between at ~650 W m^{-2}. These values conveniently put this front in context of other documented fronts, yet it is unclear they provide information about the likeliness of these dynamics occurring here. These scalings are associated with processes with different time and spatial scales that may not be appropriate for the localized nature of the observations and the rapid, superinertial evolution of stratification. For example, EBF and turbulent thermal wind (TTW) assume steady state solutions of Ekman transport along the front, which would require an inertial period to develop. Near inertial oscillations (NIOs) describes the transport of a near inertial layer over a front, but does not necessarily capture the differential shear within the ML that would tilt this front over. MLE is an average over many fronts and is better utilized in a statistical sense (e.g., Mahadevan et al. 2012; Thompson et al. 2016). Nonetheless, there are fingerprints that these processes may be acting at this front and are explored in the following chapter.

3.6 CONCLUSIONS

Presented here are an account of a shallow surface intensified front as it tilts over and stratifies the ML within one day. The survey pattern allowed for reliable calculation in a Lagrangian framework and showed that most of the vertical gradients in b, T, and S can be explained by differential advection of horizontal gradients by vertical shear.

The front exhibited surface intensified horizontal gradients in buoyancy and velocity, associated with O($0.7f$) $\zeta, \alpha,$ and δ. These strong gradients were absent in larger smoothed fields derived from the mesoscale survey and AVISO, as well as deeper in the ML. The survey also documented strong vertical velocities that are likely localized to regions of strong gradients ~600 m in width. The major downwelling event (III) was consistent with squeezing of the front by the 3-D frontal flow associated with wavelike meanders towards the end of the survey. The large horizontal gradients and vertical velocities associated with this surface intensified front suggest submesoscale dynamics distinct from 2D non-divergent flows.

The observations also capture PV conservation in the middle of the ML as the front slumped isopycnals over. Here, the tilting of isopycnals increased the vertical component of PV, which was balanced by a decrease in the horizontal component of PV due to increases in $\nabla_h b$ and along front shear. Near the surface, PV was not conserved as the ageostrophic shear impeded the growth of the baroclinic component of PV while the vertical component of PV increased with stratification. The results presented here point to the importance of near surface dynamics and frontal instabilities. These are explored in the next chapter combining the observations with idealized models.

4 CHAPTER 3: A STRATIFYING SUBMESOSCALE FRONT, PART II - DYNAMICS

4.1 INTRODUCTION

In regions of strong lateral density contrasts, sharp density fronts can slump, transforming horizontal buoyancy gradients into vertical stratification on timescales that compete with surface forcing (Boccaletti et al. 2007; Thomas et al. 2008). The surface ocean is populated with fronts ranging in size from mesoscale O (10–100 km) to submesoscale O (100 m–10 km) (Rudnick and Ferrari 1999; Hosegood et al. 2006; Mahadevan et al. 2012; Thompson et al. 2016), which have cumulative impacts on basin-scale stratification, surface PV and the distribution of heat, salt, and biogeochemical tracers within the upper ocean. A global analysis suggests that frontal processes are responsible for enhanced stratification in 30±20% of the oceans during the transition into spring (Johnson et al. 2016, Chapter 1). Yet the dominant dynamical processes responsible for the rearrangement of buoyancy at fronts remains elusive due to the dearth of direct observations of frontal slumping.

The set of observations reported in the previous chapter describe a stratifying submesoscale front in a Lagrangian framework. The frontal evolution can be divided into three stages as follows: Stage 1, downfront winds and turbulent mixing in the BL. Stage 2, diurnal warming and frontal slumping. Stage 3, nighttime surface cooling and winds, rapid near surface stratification, three dimensionality, and float subduction.

A common approach to assessing the relative importance of specific submesoscale phenomena is to compare the theoretical scalings of vertical buoyancy flux $w'b'$. As discussed in the previous chapter, this approach is not appropriate for the super inertial timescale and limited spatial scale of this survey. Nonetheless, fingerprints of submesoscale dynamics are imbedded in the observations that suggest these processes may be acting at this front, including strong ageostrophic shears, meanders, high vertical velocities, and large horizontal derivatives of tracers and velocity. The focus in this paper is to examine the possible mechanisms behind the differential advection of buoyancy that results in the slumped front and mixed layer (ML) stratification.

Here, the observations outlined in the previous chapter are combined with idealized models to isolate the possible dynamics. This is done sequentially. First a 1D model (1DPWP, Price et al. 1986) highlights the importance of top down effects from momentum and buoyancy input at the surface. Second, the MITgcm (Marshall et al. 1997) is used to simulate an idealized 2D front (2D) to explore the frontal response to unsteady wind forcing including frictional stress and modulation of turbulence. Finally, the observations alone will be used to discuss the presence of along front variability and implications for the frontal evolution.

4.2 MODEL SET-UP

1DPWP and 2D were initialized and forced with observations. Both models were initialized at yd 210 and run for 7.2 days. The model began ~6 days before the survey, at the onset of winds, which allowed for a comprehensive study of unsteady wind forcing on the front. The initial cross front temperature (T) and salinity (S) structure used in 2D is idealized from the SeaSoar mesoscale survey (Pallàs-Sanz et al. 2010b) by fitting a tanh hyperbolic function to the mesoscale SeaSoar transect. Density (ρ) in 2D was calculated using a linear equation of state. The 2D front was assumed to have an east–west orientation such that northerly winds are exactly downfront and does not take into account the curvature of the front, which ultimately modifies the orientation between wind stress and horizontal buoyancy gradient compared to observations (OBS).

The MITgcm was run in hydrostatic mode for a horizontally periodic domain extending 191 km across front, 600 m in the along front direction, and from –1.5 m to –148.5 m in vertical. The grid resolution was 300 m in the horizontal and 3 m in the vertical. Vertical mixing was parameterized with KPP. 1DPWP is initialized with the cross front average of the 2D initial state. Density in 1DPWP was calculated from the Gibbs seawater toolbox (McDougall and Barker 2011) and run with a time step of 1 hr and vertical resolution of 1 m.

4.3 1D: SURFACE BUOYANCY AND MOMENTUM

In the absence of horizontal stratification, the upper ocean buoyancy budget can evolve as a response to momentum and buoyancy fluxes at the surface. The observations spanned 30 hr, capturing a diurnal cycle of nighttime mixing that bracketed daytime warming. This diurnal forcing imprinted its buoyancy forcing and momentum in the near surface layers. Although the model was initiated ~6 days prior to the survey, only results coinciding with the observations are discussed here (Fig. 4.1).

In 1DPWP, onset of daytime warming along with the decreased winds (stage 2) shoaled the once well mixed layer that had been persistent for several days of strong winds (i.e., during stage 1). During stage 2, this upper, shallow mixed layer warmed, building stratification in the upper 3 m. The onset of wind and nighttime cooling (stage 3) simultaneously eroded the diurnal stratification and pushed it deeper into the water column, much like other models of the diurnal cycle (Price et al. 1986). The trajectory of the float followed a similar behavior to the predicted 1DPWP ML depth (Fig. 4.1b), but the distribution of stratification deviates from the simple model. Instead, the observations revealed stratification increasing at depth and throughout the water column.

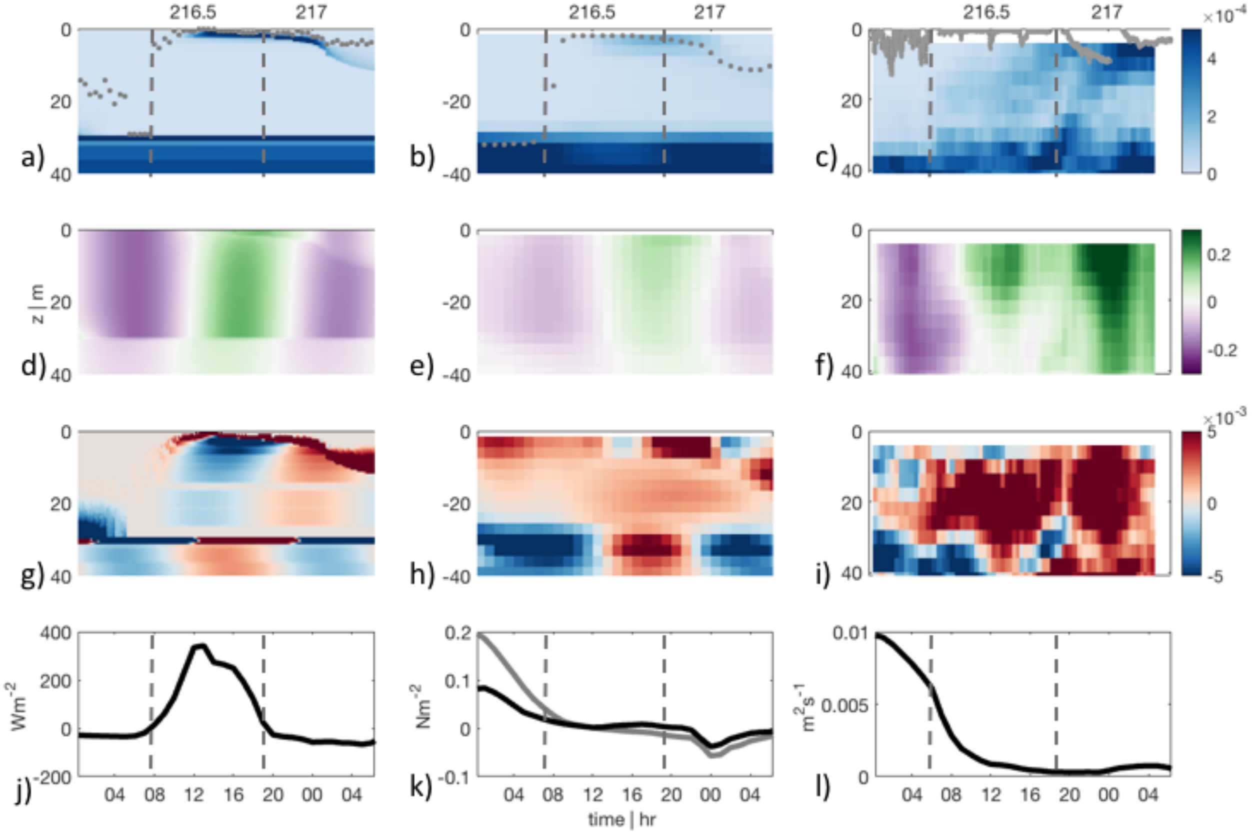

Fig. 4.1. a) 1DPWP N^2. Grey dots are PWP ML. b) 2D N^2. Grey dots are KPP boundary layer depth. c) OBS N^2. Grey dots are float depth. d) 1DPWP U, e) 2D U, f) OBS U, g) 1DPWP U_z, h) 2D U^z, i) OBS U_z, j) Q_{NET}, k) along front wind stress (grey) and cross front wind stress (black), l) KPP viscosity κ_v. Dashed lines in a, b, c, j, k, and l separate the three stages.

Variations in T and S in the observations vs. the 1DPWP highlight the importance of horizontal and vertical variability. Vertical gradients of T, S, and σ from the observations were calculated from Triaxus (see Ch. 3 for details) and from the float. During diurnal warming, the float was trapped at 2 m and therefore provided information near the surface too shallow for Triaxus. (Fig. 4.2)

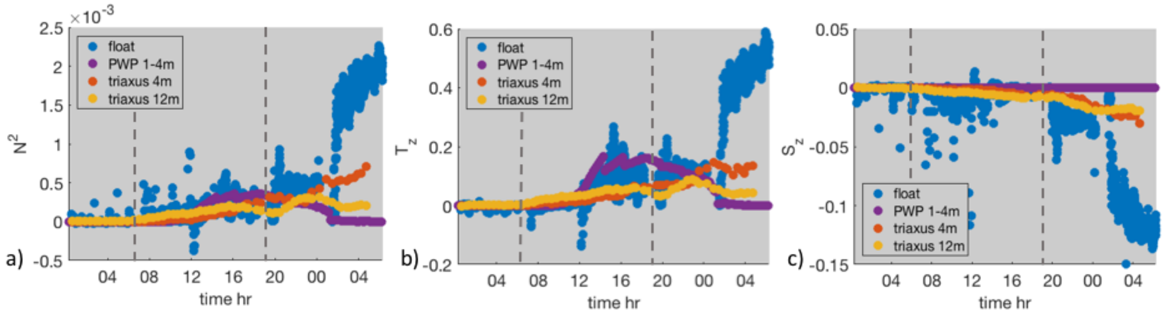

Fig. 4.2. Vertical gradients of *b* (a), T (b), and S (c) calculated from 1DPWP (purple), the float (blue), and Triaxus at 4 m (orange) and 12 m (yellow).

In this near surface layer, the float captured diurnal changes in N_2 and T_z similar to 1DPWP, yet there is evidence of lateral processes in float observations of S_z that was were captured by the 1D simulation. Deeper in the ML, N^2 in Triaxus is x0.5 the magnitude as the surface N^2, and is completely absent in 1DPWP. This is evidence of warm fresh water sliding over the cold salty upwelled waters defining the front. The largest difference occurred at the onset of stage 3 along with surface cooling and increased winds (yd 216.8) that erode the daytime stratification in 1DPWP. In OBS, the near surface layer continued to stratify, resisting the tendency of surface forcing to erode the daytime stratification. This is where the differences in the observed stratification, with its large gradients in both T and S, reveal the importance of lateral stratification on the upper ocean buoyancy budget.

While PWP had some skill at capturing a thin diurnal warm layer observed by the float, it failed to capture the evolution of stratification deeper in the ML as well as the enhanced stratification during stage 3. In these cases, salinity structure clearly displayed the key role of horizontal advection. The rest of this study considers lateral processes.

4.4 2D: FRICTION, INERTIAL MOTIONS, TURBULENT MIXING

The 2D model aimed to isolate the frontal response to unsteady winds in differentially advecting buoyancy at the front. The frontal response to the winds is apparent in Fig. 4.3b, showing the front moving towards the light side by Ekman transport from downfront winds (Fig. 4.3a). As the winds dissipated, the front oscillated back and forth.

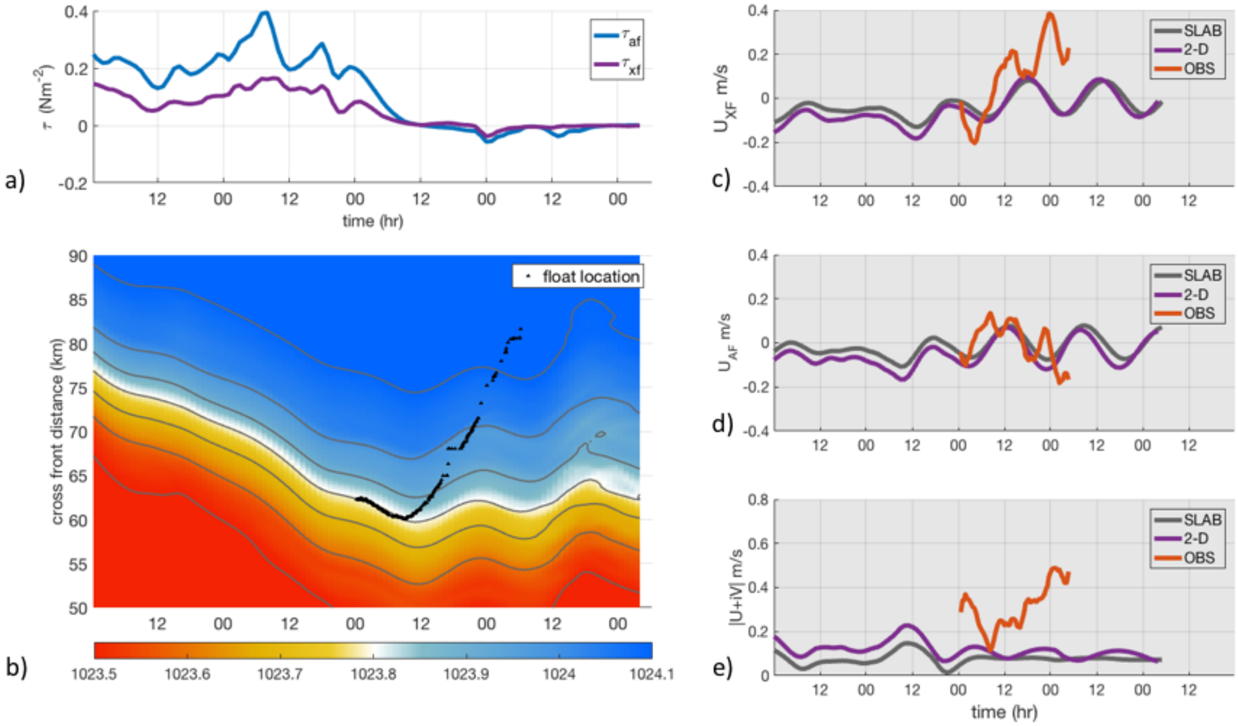

Fig. 4.3. a) Along front (blue) and cross front (purple) winds stress. b) Plan view Hovmöller plot of surface ρ in 2D, grey lines are isopycnals, black dots are cross front distance of the float trajectory overlay for reference. c-e) Velocity components for 2D, solution to eq. 4.1, eq. 4.22, and OBS.

The oscillations in the 2D model can be described by an inertial response to wind forcing averaged throughout the ML (Pollard and Millard 1970)

$$\frac{du}{dt} - fv = \frac{\tau_x}{\rho_o H} \qquad (4.1)$$

$$\frac{dv}{dt} + fu = \frac{\tau_y}{\rho_o H} \qquad (4.2)$$

This was solved for the entire length of the model runs, initialized when τ~0, and assuming u_i=v_i=0, and H=30 m (Fig. 4.3c–e). The solution agrees well with 2D, suggesting this wavelike pattern after the winds dissipate were wind driven inertial motions. This signal is obscured in the observations. As the winds decrease, the float slows (Fig. 4.3b, e) and turns eastwards (Fig. 4.3b, c), albeit at a pace faster than the 2D model. This may be attributed to an external large-scale response to wind. The observations also exhibit high frequency oscillations faster than the NIO, suggesting along front variability associated with meanders along the front.

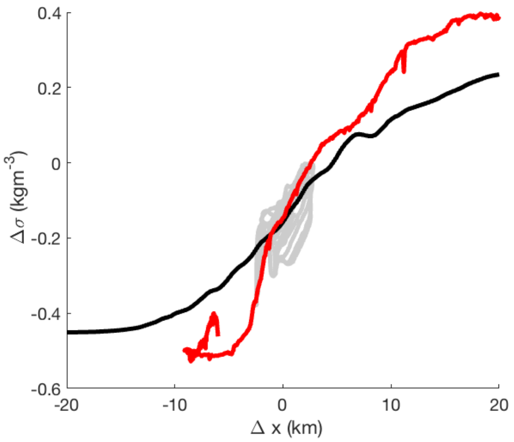

Fig. 4.4. Cross front density structure in ship underway (red) during the initial frontal transect, and in 2D (black) at yd 217. Density from ship underway during the first 4 hr of the survey (grey).

The persistent winds diffused the front in the model such that the modeled front is weaker than observed. (Fig. 4.4). The difference may be due to the lack of external strain in the 2D model compared to OBS (Ch. 3, Table 3.1 and Fig. 3.12).

However, the low mode agreement between the observations and model suggest the importance of NIO motions. Eq. 4.1 and eq. 4.2 are appropriate for a slab ML, but cannot capture the response of shear within this ML. Therefore, a different set of equations must be used to capture the time dependent response to the wind forced front.

4.4.1 *Compare 2D and 1D+*

The hydrostatic primitive equation for horizontal momentum can be written

$$\frac{D\mathbf{u}_h}{Dt} = -f\hat{z}\times\mathbf{u}_h - \frac{1}{\rho_o}\nabla p + \frac{\partial}{\partial z}\left(\kappa_v \frac{\partial \mathbf{u}_h}{\partial z}\right) \qquad (4.3)$$

where f is the Coriolis parameter, κ_v the vertical diffusivity associated with the boundary layer, and p the pressure normalized by a reference density (ρ_o).

To focus on shear, take the vertical derivative of eq. 4.3 and ignore the advective terms, yielding

$$\frac{\partial}{\partial t}\left(\frac{\partial u}{\partial z}\right) = fv - \frac{\partial b}{\partial x} + \frac{\partial^2}{\partial z^2}\left(\kappa_v \frac{\partial u}{\partial z}\right) \qquad (4.4)$$

$$\frac{\partial}{\partial t}\left(\frac{\partial v}{\partial z}\right) = -fu - \frac{\partial b}{\partial y} + \frac{\partial^2}{\partial z^2}\left(\kappa_v \frac{\partial v}{\partial z}\right) \qquad (4.5)$$

where the pressure term has been replaced with density using the hydrostatic approximation $\frac{\partial p}{\partial z} = -\rho g$ and buoyancy $b = -g\frac{\rho}{\rho_o}$. This system of equations can be combined into one in complex form assuming $Y = \frac{\partial u}{\partial z} + i\frac{\partial v}{\partial z}$ and $M = \frac{\partial b}{\partial x} + i\frac{\partial b}{\partial y}$:

$$\frac{\partial}{\partial t}Y = -i\omega Y - M + \frac{\partial^2}{\partial z^2}(\kappa_v Y) \qquad (4.6)$$

(I) (II) (III) (IV)

The boundary conditions are

$$\kappa_v Y = \frac{1}{\rho}T \quad \text{at } z = 0, \qquad \kappa_v Y = 0 \quad \text{at } z = -H. \qquad (4.7)$$

where $T = \tau^x + i\tau^y$ is the complex wind stress at the surface.

Dauhajre (submitted) used eq. 4.3 to characterize the modulation of the diurnal cycle on a front forced with constant winds. The results suggest a transition between two phases. Nighttime winds and cooling induce turbulent mixing and a TTW overturning circulation. The onset of solar warming shuts off turbulent fluxes, leaving a front out of thermal wind balance. The result is an inertial response akin to the low level jets developed in the atmosphere (Van de Wiel et al. 2010). The reversal back to nighttime cooling transitions back into the diffusive regime that damps the inertial oscillation. The regime here is slightly different in that there was a rapid decrease in convective and wind driven turbulence. This, in a sense, is a modified adjustment problem with turbulence, or turbulent adjustment.

Note the combination of balances encapsulated in eq. 4.6. I, II, III capture internal waves with frequency set as the earth's rotation. The evolution of I, II, and III were explored by Tandon and Garrett (1994, TG94) in an idealized frontal adjustment of nearly vertical isopycnals at rest. I, II, IV is analogous to the slab ML model of wind driven inertial motions (eq. 4.1 and eq. 4.2). II, III is thermal wind balance, and adding (IV) explores the effects of flux divergence on TTW. It will be shown that each of these balances alone are insufficient, yet when combined, work to create a shear tendency capable of tilting isopycnals and enhancing stratification in the ML comparable to the model and observations.

Eq. 4.6 was solved numerically using a Crank–Nicolson time stepping regime (1DCN), an implicit method for solving stiff ordinary differential equations (ODEs) (LeVeque 2007). Boundary conditions (eq. 4.7) were included in the discretized operator in IV. A solution was calculated for every grid point across the front. The IDCN model was initialized with a profile of Y, κ_v, and M from 2D at the time the observed float gets trapped in the BL (yd 216.3, stage 2). Profiles of κ_v and M were set constant in time. The solution was then integrated in z to obtain values for u and v assuming no motion at the bottom. Solutions here are considered 1D in the sense that they are decoupled from neighboring grid points.

The agreement between the 1DCN and 2D is shown in Fig. 4.5. Features of eq. 4.6 are manifested in the evolution of u_z and v_z. An oscillatory behavior exists deeper that is indicative of an inertial oscillation (I, II) and the contribution from friction (IV) can be seen near the surface and throughout the ML. These terms worked in concert to evolve the shear.

The contribution of the terms in eq. 4.6 are highlighted by solving 1DCN with specific terms: I, II, III with Y_i (Fig. 4.5c, g.) and I, II, III, IV with no Y_i (Fig. 4.5d, h). Fig. 4.5 c, g is similar to inviscid adjustment, where the time dependent solution includes inertial oscillations. Here the solution was modified by the thermal wind imbalance set by the initial shear Y_i and resulted in sheared patterns tilted in the vertical. Note that there are no damping terms in I, II, III, and therefore these oscillations would continue for all time.

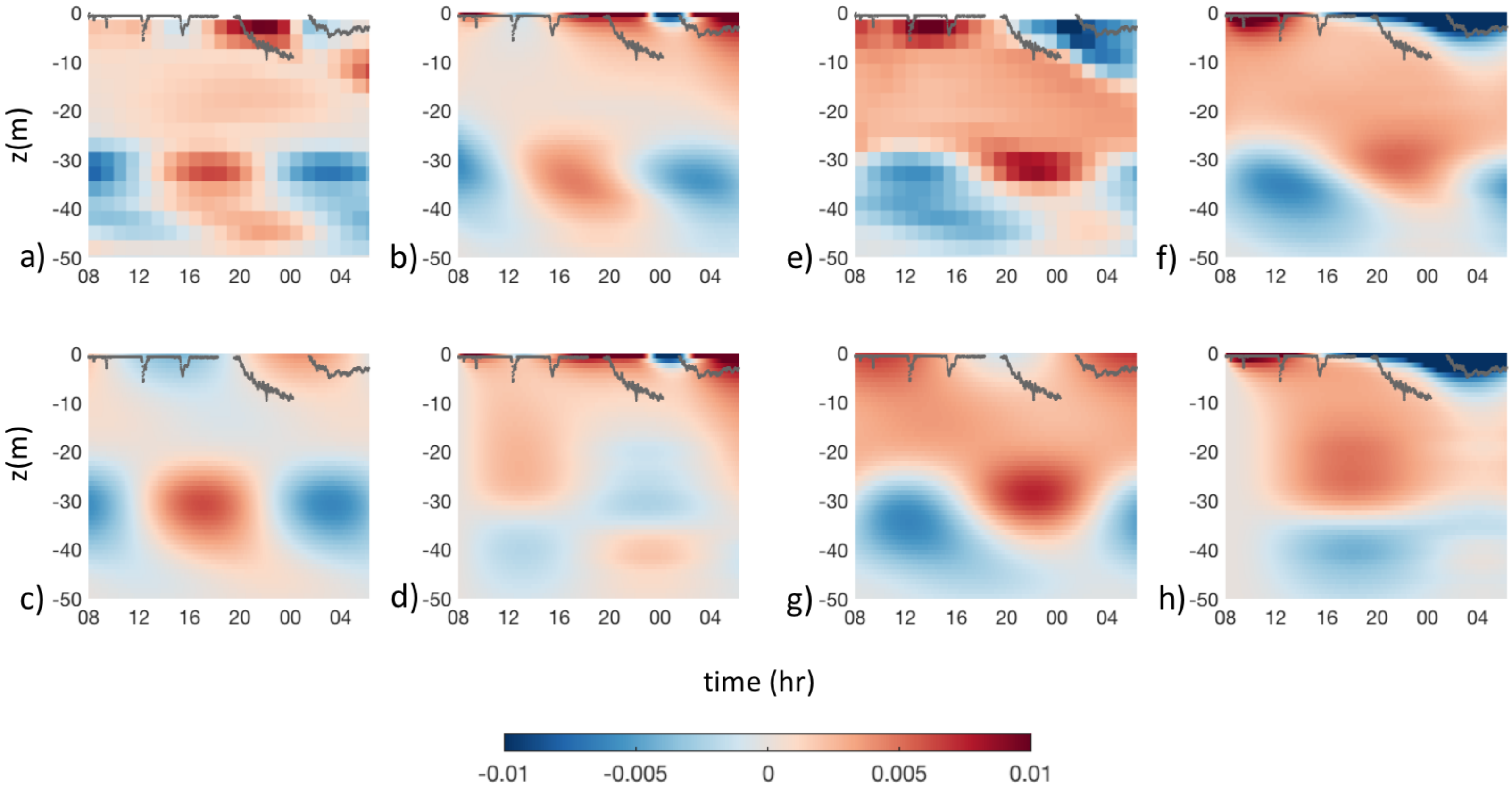

Fig. 4.5. (a–d) Cross front u_z. (e-h) Along front u_z. (a, e) 2D, (b, f) 1DCN, (c, g) IDCN with no κ_v, (d, h) IDCN with no Y_i. Grey lines denote float location in OBS for reference.

This is not the case when considering IV and friction (Fig. 4.5 d,h). Momentum input from the surface combined with the redistribution of momentum by IV simultaneously damped the NIO and introduced an external source of shear. The simplicity of 1DCN highlights the importance of the transient response of the front to unsteady forcing, thermal wind imbalance, and the vertical momentum flux divergence, κ_v.

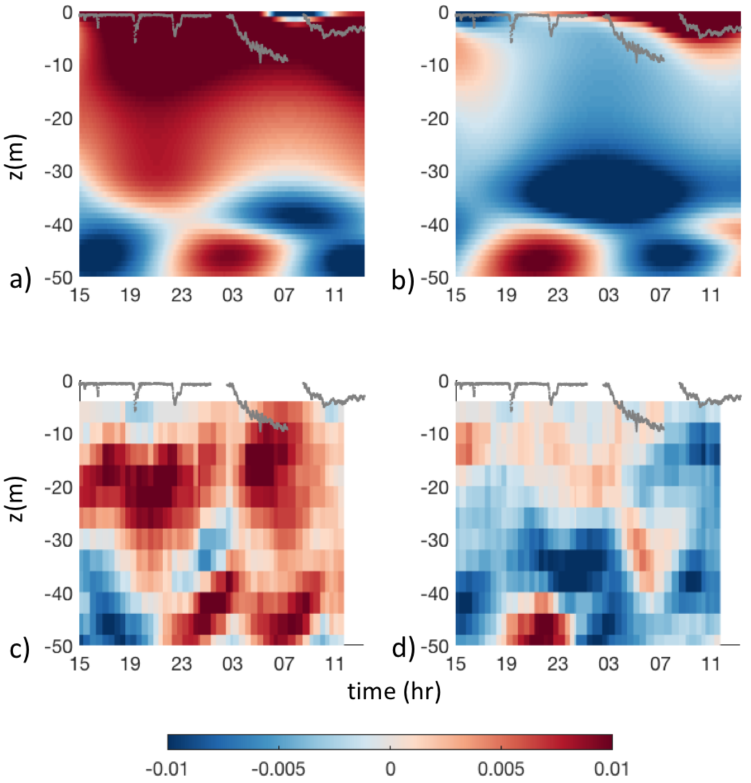

Fig. 4.6. (a) IDCN u_z initialized with OBS, (b) IDCN v_z initialized with OBS, (c) u_z from OBS, and (d) v_z from OBS

1DCN was also solved with initial conditions set by OBS. Triaxus data at yd 216.3 are smoothed to provide Y_i and M, while κ_v is taken as the cross front averaged profile from 2D. The agreement between the 1D solution and OBS is inferior as the 2D (Fig. 4.6). This may be due to along front variability and curvature that influences M, as well as the semi Lagrangian interpretation of the observations at depth (see Ch. 3.). Within the pycnocline (50 m), the solution and observations exhibit similar oscillatory behavior, confirming that oscillations in the observations (that also appear in 2D) can be attributed to NIOs trapped below the ML. Yet near the surface, the solution and observations deviate.

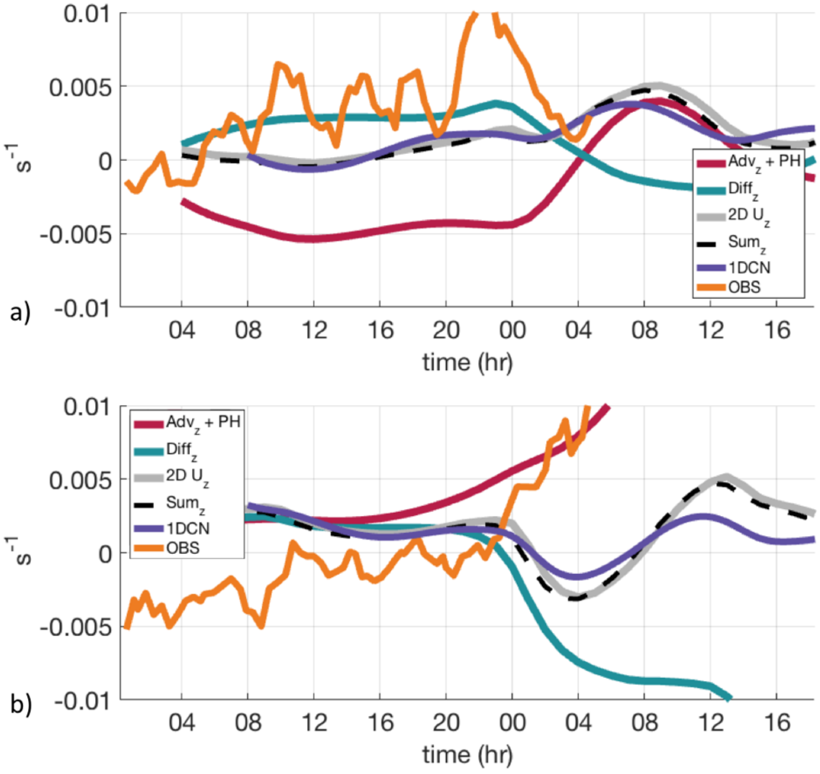

Fig. 4.7. (a) u_z. (b) v_z, rotated such that along front shear is positive (i.e., $-v_z$ in OBS). Each plot includes shear from 2D (grey), 2D ADV (red), 2D DIFF (teal), 1DCN (purple), and OBS (orange).

Contributions from viscosity and the inertial response are reaffirmed in the budgets provided by the MITgcm (Fig. 4.7). Here, the vertical derivatives of the momentum tendency terms were integrated in time. This showed that the evolution of shear in 2D could be described by the diffusive terms (DIFF; i.e., IV) and the sum of the advective and pressure terms (ADV; i.e., II + III). During stage 2, DIFF had a tendency to increase the downgradient cross frontal shear and along front shear, while ADV had a tendency to decrease the downgradient shear and reinforce the along front shear. During stage 3, winds rotated to the upfront position and input shear against the geostrophic shear and up-gradient, as the advective terms continually act to increase shear. The evolution of shear in 2D is matched by the 1DCN solution, though deviations towards the end are expected as time varying viscosity and higher order terms in 2D become important (Dauhajre, submitted; Wenegrat and McPhaden 2016). The agreement with these idealized models and the OBS is less clear. During stages 2 and 3, the front was in a curved orientation and both components of shear contain contributions from thermal wind balance. Nonetheless, there was some agreement between OBS and 2D that suggests DIFF was contributing to cross frontal shear. This is not the case in along front shear where DIFF was opposite of OBS. Instead, OBS was in better agreement with ADV. During stage 3, the model eroded the daytime near surface stratification while the OBS continued to stratify. This may explain part of the discrepancy between the shear in 2D and OBS.

It is also helpful to look at hodographs from the 1DCN solutions, 2D, and OBS. (Fig. 4.8) In the turbulent ML, inertial oscillations in 1DCN, 2D were clockwise and became smaller with time (Fig. 4.8a), revealing the damping of the NIO by κ_v. The observed shear does not have the same type of pattern, which was counterclockwise before turning to a clockwise trajectory in the last ~11 hr of survey. Part of this difference can be linked to the meanders along the front. The hodograph deeper clearly revealed an anticyclonic inertial motion at 40–50 m that is in agreement among 1D, 2D, and OBS.

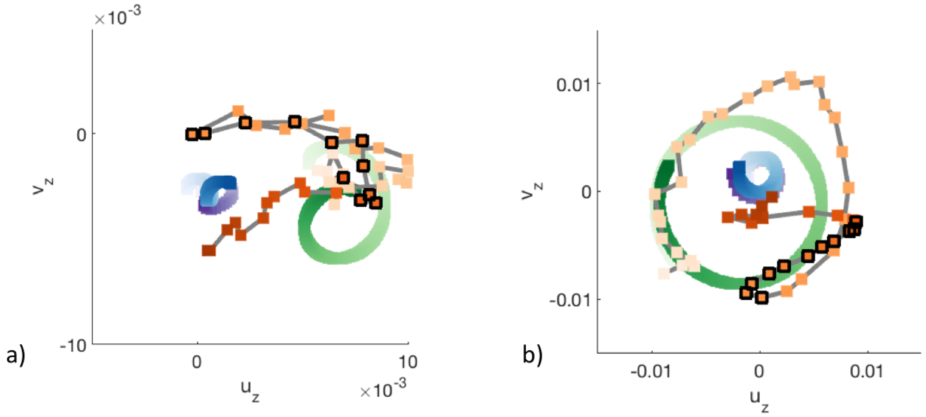

Fig. 4.8. Hodographs of shear at (a) 15–25 m, and (b) 40–50 m. 2D (purple), $1DCN_{2D}$ (blue), OBS (orange), and $1DCN_{OBS}$ (green). Shading represents time, beginning at onset of stage 2 (light shade) until the end of stage 3 (dark shade). Black borders represent time that float subducts in OBS.

Eqs. 4.4 and 4.5 are a simple, reduced set of coupled equations to explain the evolution of shear at this wind forced front and appear to have some skill at reproducing the shear in the 2D model. Furthermore, Fig. 4.5–Fig. 4.8 all exhibit a positive cross front shear. It will be shown that this cross front shear is able to differentially advect buoyancy across the front to enhance stratification comparable to the observations.

4.4.2 *Effects on stratification*

The modified adjustment induces a shear that can differentially advect buoyancy across the front and modify vertical stratification. This was estimated in the 1DCN and 2D models using

$$N_{INT}^2 = \int_{t_o}^{t_i} -b_x u_z - b_y v_z \, dt \tag{4.8}$$

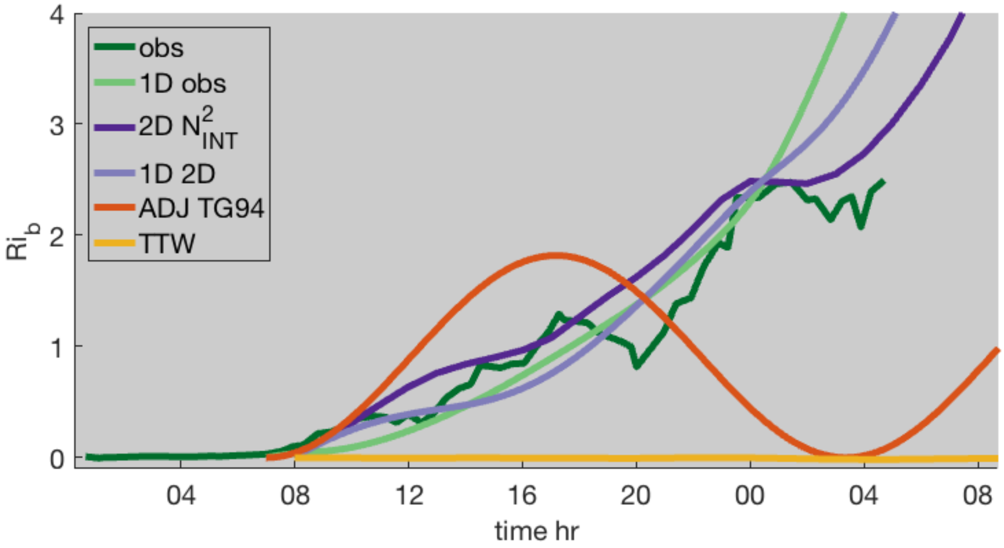

Fig. 4.9. N^2 normalized to Ri_B. N^2 for the OBS (dark green). N_{INT}^2 in 2D (dark purple), and for the IDCN solutions to the OBS (light green) and 2D (light purple). Solutions to ADJ (orange) and TTW (yellow).

Eq. 4.8 was solved in section 3.3 (Fig. 3.10) to show that most of the stratification at the front could be attributed to differential advection of horizontal gradients. Here, it was solved for 1DCN with corresponding initial M, and for 2D at each grid point. Eq. 4.8 was also solved for the solution to TTW (i.e., II, III, IV) at every grid point and for ADJ (i.e., I, II, III) using an arbitrary M and Y_i=0. Results are presented in terms of balanced Richardson number $Ri_b = \frac{N^2 f^2}{M^4}$. This normalizes for the effects of M^2 (which is about x10 larger in OBS than 2D) and allows the solutions to be compared with a state of thermal wind balance (i.e., Ri_b=1).

N_{INT}^2 from 2D, and the IDCN solutions increased at rates similar to N^2_{OBS}, suggesting cross front shear predicted by these idealized models was capable of reproducing the observed tilting of the front. If the evolution depended solely on I, II, III as in TG94, shear would tilt isopycnals over and re-tilt them back to vertical in an NIO for all time. Conversely, if this was a case of steady state TTW, the steady state Ekman transport and TTW circulation would stratify weakly at a rate unrelated to the tendency in the model and observations.

Here, the combination of DIFF and ADV suggest that transient, super inertial frictional effects are responsible for differentially advecting horizontal stratification across the front. Without an external source of friction at the boundary, the ML shear due to ADJ would damp out as momentum is distributed evenly throughout the water column through IV. The surface boundary condition modified this by providing an external input of shear. The instantaneous magnitude and direction of friction at the surface was rotated as it was distributed throughout the turbulent boundary layer by IV via Ekman dynamics. This highlights the importance of friction and transience, both of which were needed to produce a persistent flattening of isopycnals. This differentiates this simple 1D model and the observations from traditional adjustment, NIOs, or steady state EBF.

4.4.3 *Frontogenetic tendency*

Fronts in the upper ocean are subject to a range of external forcing that can disturb thermal wind balance. This is captured in the frontal tendency equation

$$F = \frac{1}{2}\frac{D\|\nabla_h b\|^2}{Dt} = F_{sg} + F_{sa} + F_{kv} + F_w, \qquad (4.9)$$

$$F_{sg,sa} = -b_x \nabla_h u_{g,a} - b_y \nabla_h v_{g,a}, \qquad (4.10)$$

$$F_{kv} = \nabla_h \left[\frac{\partial}{\partial z}\left(\kappa_v \frac{\partial b}{\partial z}\right)\right] \cdot \nabla_h b, \qquad (4.11)$$

$$F_w = -\frac{\partial b}{\partial z} \nabla_h w \cdot \nabla_h b, \qquad (4.12)$$

F_{sg} and F_{sa} constitute the advective tendency of the flow to squeeze or spread isopycnals apart. The sum of these terms for OBS is plotted (Fig. 3.13) because they are inseparable. In the 2D model, all advective terms were zero except the divergent component of the ageostrophic flow, F_{sa}. F_{kv} captures the ability for IV to disturb thermal wind balance (i.e., TTW). These terms are shown in Fig. 4.10.

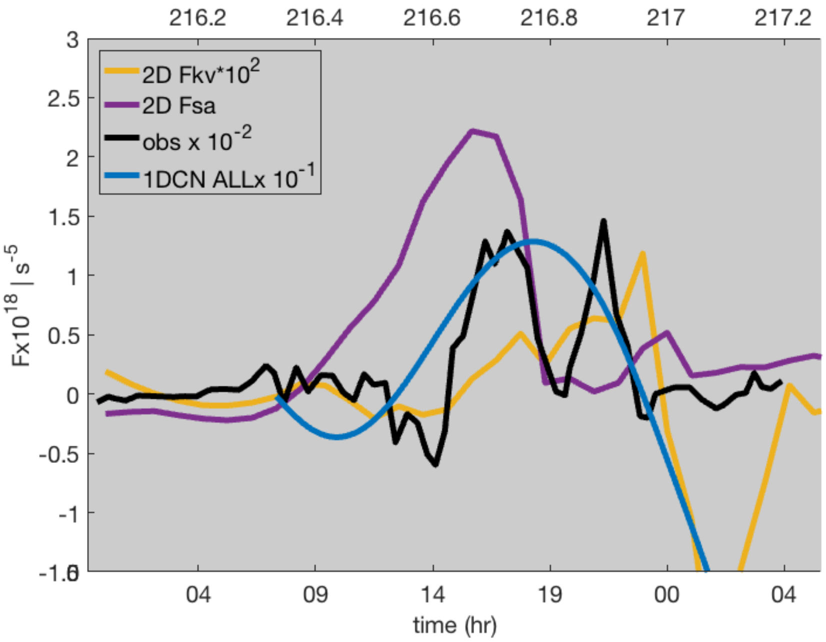

Fig. 4.10. Frontogenetic tendency terms calculated from the OBS (Ch. 3.), 2D F_{sa} (purple) and F_{kv} (yellow), and for 1DCN$_{2D}$ (blue).

F_{sa} was the largest term. It builds as turbulence lessens and therefore may be associated with the same ageostrophic velocity field acting to tilt isopycnals. The cross front variability in Y_i, M, κ_v imply dephasing of the inertial response that can cause isopycnals to squeeze or spread apart as they tilt over at different rates. F_{sa} in 1DCN was calculated from the u and v fields and constant initial M. The inertial oscillations de-phase immediately such that they cause isopycnals to spread (frontolytic) and then squeeze (frontogenetic) peaking at yd = 216.7.

This very simple set of equations is not complete nor coupled and therefore not a diagnostic for frontogenesis. Yet the agreement between this simple approximation and the full 2D model suggests they may provide some skill in isolating potential dominant processes acting to differentially advect buoyancy, and that this may occur at non-uniform rates across the front to squeeze the front together therefore contributing to smaller scales.

4.4.4 *Potential vorticity*

The role of different processes in setting the stratification can be seen through Ertel's form of potential vorticity (PV)

$$q = \boldsymbol{\omega}_a \cdot \nabla b, \qquad (4.13)$$

Neglecting the contribution from vertical velocity, this can be written as a sum of the vertical and horizontal (i.e., baroclinic) components

$$q_V = (f + \zeta)\mathrm{N}^2 \qquad (4.14)$$

$$q_H = u_{af} b_{xf} - v_{xf} b_{af}. \qquad (4.15)$$

Ch. 3 evaluated q_V and q_H in OBS and found that changes in these terms balanced each other in the middle of the ML (16 m), illustrating PV conservation. This was not the case near the surface (4 m) where q follows q_V as the upper layer stratifies, while the contribution from q_H remains near zero. This lack of balance was evidence of PV injection at the surface.

PV conservation states (Marshall and Nurser 1992) that changes in – may arise from the divergence of the PV flux (J),

$$\frac{Dq}{Dt} = -\nabla \cdot \boldsymbol{J} \qquad (4.16)$$

$$\mathrm{J} = q\mathbf{u} + \nabla b \times F - D\boldsymbol{\omega}_a \qquad (4.17)$$

$$\mathrm{D} = \frac{\partial b}{\partial t} + \mathbf{u} \cdot \nabla b \qquad (4.18)$$

$$\mathrm{F} = \frac{\partial u}{\partial t} + \mathbf{u} \cdot \nabla u + \frac{1}{\rho} p + fk \times \mathbf{u} \qquad (4.19)$$

Winds and radiative forcing impart a vertical divergence of J at the surface. For example, heat flux can influence PV through the diabatic terms in eq. 4.18. Because the OBS suggest stratification results from the advection of buoyancy across the front, the focus is on PV changes as a result of shear.

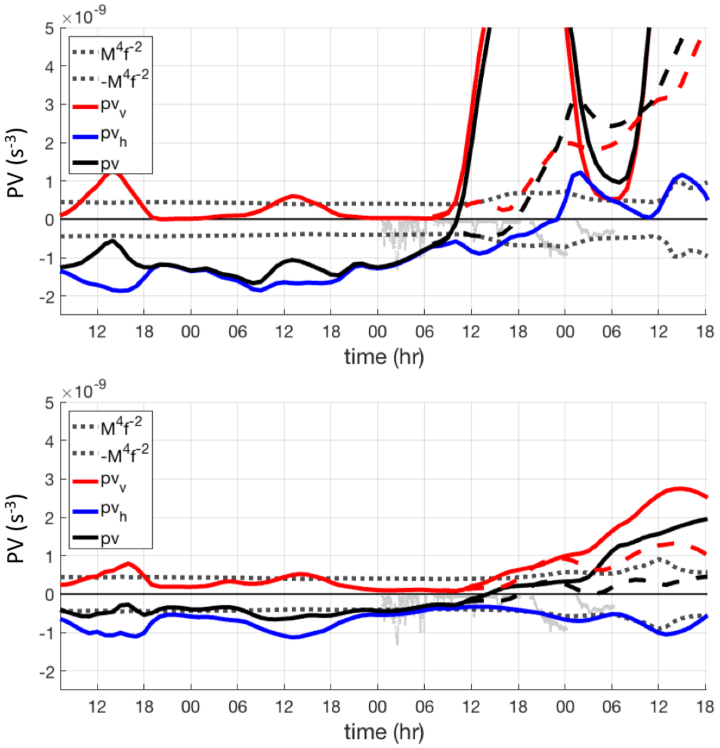

Fig. 4.11. PV and its components from 2D at 4 m (a) and 16 m(b). q_V (red), q_H (blue), and q (black). N^2_{INT} is used to estimate the advective contribution to q_V (red dash) and q_H (black dash). Thermal wind balance, M^4f^{-2}, (small black dash) and float depth (scaled x10^{-9}) are added for reference.

Eqs. 4.18 and 4.19 imply that shear introduced into the system can impact PV in two ways. Along front shear can influence *J* through the baroclinic terms via *F*. For example, upfront shear injects PV working against the geostrophic shear, while downfront winds remove PV by increasing the baroclinicity. This, on its own, does not increase stratification. Stratification can occur as shear input at the surface is redistributed and rotated through IV via Ekman dynamics to a cross front shear that advects buoyancy and therefore N^2.

In 2D, PV and its components were calculated at 4 m and 16 m (similar to OBS in Ch. 3). q and q_V were also calculated using N^2_{INT}, because the relative contribution of Q_{NET} on N^2 in 2D was larger than the OBS. This view of q in 2D paints a similar picture to OBS where PV conservation (in terms of advective components, N^2_{INT}) and thermal wind balance is evident at 16 m, yet not at 4 m. However, the pattern of q_H at 4 m differs between 2D and OBS due to the along front shear (also in Fig. 4.7 and Fig. 4.8), possibly the result of an overestimation of DIFF in 2D compared to OBS during stage 3.

In an idealized model of adjustment (i.e., I–III; TG94), the effects of shear on q_V and q_H exactly cancel such that PV is conserved for all time. This is modified by the addition of friction at the boundary redistributed by IV, therefore this modified adjustment is non-PV conserving.

This section brought together a simple reduced model of turbulent adjustment with an idealized 2D numerical simulation to highlight the role of unsteady wind forcing on the evolution of a shallow ML front. Yet difference in the strength of ∇b between the OBS and 2D suggest the importance of external circulation and along front variability, which, by definition, are excluded in these idealized representations of the front and may play an important role on the frontal structure.

4.5 ALONG FRONT VARIABILITY

A particularly interesting outcome from Ch. 3 was the increased structure and magnitude of horizontal velocity gradients at smaller scales. For example, an external strain field induced by the mesoscale circulation is documented by the SeaSoar survey and AVSIO. This larger scale strain field is augmented by an internal strain field that modulated with the meandering buoyancy field. This along front variability is apparent throughout the observations and suggested by satellite SST (Fig. 3.1) that reveals wavelike structures along the front. Wavelike patterns have been studied in many high resolution numerical simulations as being associated with frontal instabilities (e.g., Capet et al. 2008b). These meanders are captured by the Triaxus survey (Fig. 3.4) and imprinted throughout fields of velocity, strain, vorticity, isopycnals depth and frontal tendency ($F_{sa} + F_{sg}$; Fig. 3.13).

This along front variability is a particular feature of growing baroclinic waves. In the ML, surface intensified fronts exist in an environment of low stratification and high Rossby number. This makes them susceptible to a type of ageostrophic baroclinic instability (BCI) (Stone 1966; Boccaletti et al. 2007). Using this linear theory, it is assumed this front would develop baroclinic waves with a lengthscale of ~20 km that would evolve on a timescale of days. These waves grow into large eddies MLEs that reach finite amplitude as the nonlinear terms become important and stratification ensues. The rate of stratification from MLE has been parameterized as an overturning streamfunction for course resolution models (Fox-Kemper et al. 2008)

$$\Psi_o = C_e \frac{\nabla_h b H^2 \times \mathbf{z}}{|f|} \mu(z)\,, \qquad (4.20)$$

$$\mu(z) = \left[1 - \left(\frac{2z}{H} + 1\right)^2\right]\left[1 + \frac{5}{21}\left(\frac{2z}{H} + 1\right)^2\right] \qquad (4.21)$$

$$\frac{dN^2}{dt} = -C_e \frac{\nabla_h b^2 H^2}{|f|} \frac{\partial^2 \mu(z)}{\partial z^2} \qquad (4.22)$$

A compelling feature of this parameterization is the vertical structure of overturning streamfunction $\mu(z)$, analogous to that predicted by Eady (1949), that captures the near surface intensification of MLE induced stratification. (Fig. 4.12).

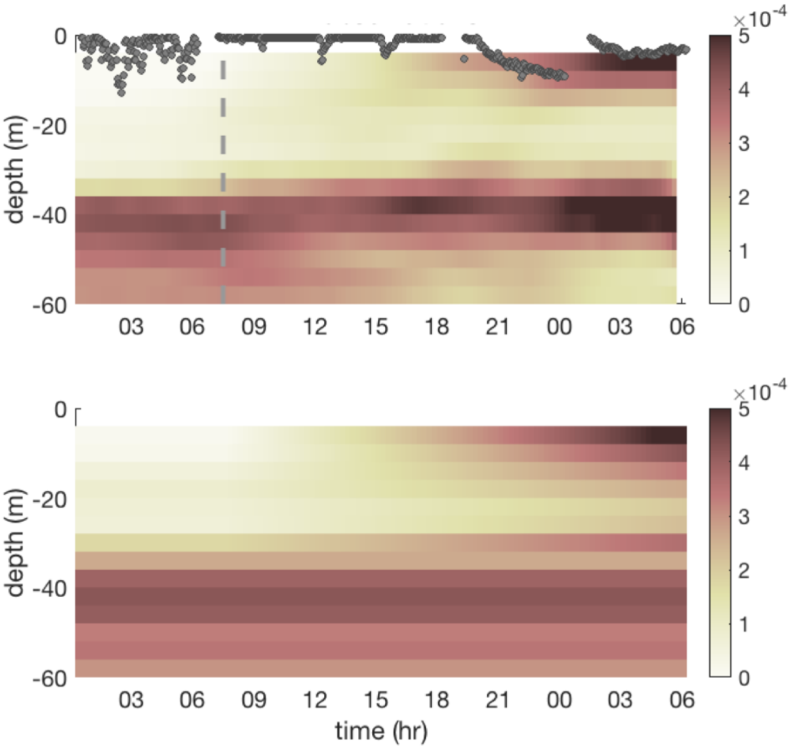

Fig. 4.12. Top: N^2 from OBS. Bottom: N^2 from eq. 4.20

N^2 predicted by this parameterization develops a strikingly similar profile as the observations. Yet this parameterization is meant to represent the along front and across front averages within an idealized model, and not any instantaneous profile along the front. The OBS are capturing 5 km by 5 km averages of a 1-km wide front (Fig. 3.1). It is unclear that this survey is averaging over a domain of vigorous eddies. Furthermore, the parameterization as represented here does not account for the external strain field or surface forcing, both of which modify the BCI and frontal structure. While SST and in situ data suggest frontal instability may be occurring at this front, it is unclear that MLE is the dominant source for the vertical structure of stratification.

4.6 VERTICAL STRUCTURE OF STRATIFICATION

The external strain field is essential for strengthening ∇b and therefore the amount of N^2 by differential advection. This is evident when comparing the evolution of N^2 during stage 3 between OBS and 2D. The daytime N^2 in 2D is an order of magnitude less than OBS, and thus is not strong enough to resist erosion by nighttime mixing and convection. This is precisely when N^2 in OBS increases the most.

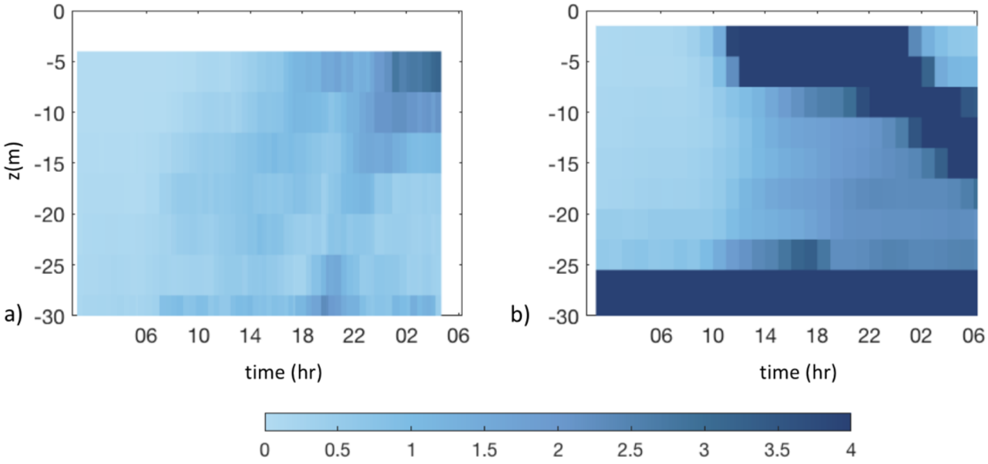

Fig. 4.13. Ri_b for OBS (a) and 2D (b).

The absence of nighttime mixing in OBS during stage 3 highlights the importance of horizontal processes on the upper ocean buoyancy budget and reinforces the role of external and internal strain at influencing the strength of the front and therefore the magnitude of N^2.

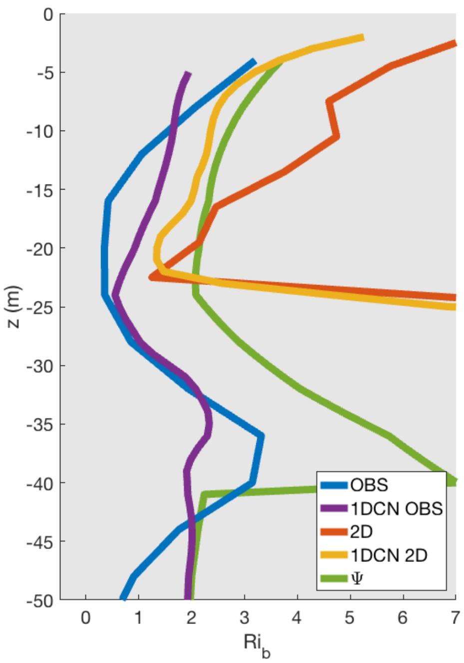

Fig. 4.14 Vertical structure of N^2 in terms of Ri_b.

The observed stratification has a unique vertical structure that is enhanced near the surface (Fig. 4.13, Fig. 4.14). This vertical structure can be replicated by N^2_{INT} from 2D and IDCN, suggesting these idealized models are capturing differential advection by boundary layer turbulence that is enhanced near the surface. This structure of stratification is also inherent in the MLE parameterization (eq. 4.22), which shares the same behavior near the surface. The shared habit of stratification between these observations, theories, and models demonstrates the complicated nature of teasing apart these processes in shallow ML. Additionally, the agreement in the structure of stratification would be different in very deep ML, where MLE would dominate at depth, while frictional dynamics operate near the boundary.

4.7 CONCLUSION

Detailed observations combined with idealized models show the importance of horizontal advection in stratifying the upper ocean. Specifically, an idealized 2D model combined with a simple reduced model were able to give insight into the role of turbulent adjustment that can rapidly stratify the ML on superinertial timescales and compete with surface forcing. Additionally, images of SST and along front variability captured in the observations suggest possible mixed layer instabilities, which grow on a relatively longer timescale, suggesting that this rapid stratification may be dominated by turbulent adjustment.

The vertical structure of stratification reveals the importance of boundary layer dynamics on shallow ML fronts. Traditionally, attention has been given to the importance of fronts in deep MLs, as they have stored potential energy available to grow instabilities. Turbulent adjustment is a rapid mechanism that can be dominant in shallow MLs and act to decrease the available potential energy at a front before instabilities can grow. This suggests the potential importance of shallow MLs on the upper ocean buoyancy budget (Ch. 2).

None of the current scalings or parameterizations capture this rapid stratification (Fig. 3.17). EBF_{NIO} (Savelyev et al. 2017) has been used to explain the integrated Ekman transport of NIO over the deeper Gulf Stream, but does not provide information on shear within the boundary layer, which is responsible for the stratification in OBS and 2D. EBF (Thomas and Lee 2005) and TTW (McWilliams et al. 2015, Wenegrat submitted) demonstrate the importance of friction and viscosity on thermal wind balance, but assume a steady state solution that would require at least an inertial period to develop. In other words, the time dependent NIO is missing friction, and the friction scalings are missing time dependence. It has been shown here that both are important at this front.

Furthermore, the surface stratification by differential advection converts horizontal changes of salinity and temperature into vertical ones on a timescale that competes with surface forcing. If these slumped gradients are subject to repeated mixing, they undergo a process of nonlinear diffusion (Young 1994) that leads to horizontal density compensation often observed in the ML (Ferrari and Rudnick 2000). This might provide a mechanism to homogenize the cold salty, recently upwelled waters with the warmer, fresher surface waters offshore, and therefore an important part in the mixing of tracers in the California Current System upwelling regime.

5 CONCLUSIONS

This dissertation highlights the importance of small scale fronts on the upper ocean buoyancy budget on timescales that compete with surface forcing.

Chapter 2 takes a global approach to assess the importance of frontal slumping on springtime restratification. Observations are contrasted with a 1D mixed layer model to assess where lateral processes influence mixed layer evolution. Relationships between the large scale horizontal TS and local vertical TS are used to identify regions where lateral gradients are transformed into vertical stratification. This analysis indicates that lateral slumping may be responsible for ~40±25% of the increased stratification not captured by 1D models. Enhanced stratification from frontal tilting occurs in regions of strong horizontal density gradients, with a small fraction in regions of deep mixed layers.

Chapters 3 and 4 present a highly detailed process study of one surface intensified submesoscale front in the California Current System. The observations provide an unprecedented account of a front as it tilts over and stratifies the ML in one day. Observed vertical gradients of b, T, and S could be explained by advection of horizontal gradients by the vertical shear. This suggested that ageostrophic cross frontal shear was acting to differentially advect buoyancy and enhance stratification at this front and is a major result of this study. This increase in stratification is associated with a decrease in the available potential energy at the front with a restratifying effect equivalent to 600 W m^{-2}.

Idealized models were employed to investigate the contribution of boundary layer dynamics at setting the ageostrophic shear acting to tilt the front. A simple reduced model of turbulent adjustment was combined with a MITgcm in an idealized 2D configuration of the front. Together these pointed to the contribution of a transient response to the front's thermal wind imbalance combined with viscous effects within the turbulent boundary layer and friction input at the surface. Turbulent adjustment provided a mechanism to rapidly stratify the ML on superinertial timescales that compete with surface forcing.

In addition to the 2D dynamics captured in the idealized models, the front clearly showed the existence of along front variability. This along front structure is associated with O(0.7*f*) vorticity, divergence, and strain along with large, highly localized vertical velocities. These suggest submesoscale processes at this front that are distinct from 2D non-divergent flows assumed in the classical QG framework. The along front variability was consistent with wave like structures found in images of SST and suggests the existence of mixed layer frontal instabilities that can tap into the frontal APE and stratify the upper ocean. Despite this, the relatively longer timescale of mixed layer instability growth suggests that this rapid stratification may be dominated by turbulent adjustment.

The observations and 2D model also capture PV conservation in the middle of the ML as the front slumps isopycnals over. Here, the tilting of isopycnals increased the q_V, which was balanced by a decrease in q_H due to increased ∇b and along front shear. Near the surface, PV is not conserved because the ageostrophic shear impedes the growth of q_H while q_V and q increases with N^2. This suggests the importance of wind and boundary layer friction on the upper ocean potential vorticity budget.

A common theme arising from these different studies is the importance of shallow MLs at modulating stratification in the upper ocean. Traditionally, attention had been on the importance of fronts in deep MLs, as they have stored potential energy available to grow instabilities. Chapter 1 suggests that frontal slumping dominates upper ocean stratification in regions of strong gradients and shallow ML. This brings attention to the importance of processes at shallow ML fronts, such as the observations detailed in Ch. 3 and Ch. 4. BL turbulence could play a dominant role as the extent of the BL and depth of the ML front become comparable in length scale. The rapid restratifying effects of turbulent adjustment could provide a mechanism to extract potential energy from a front faster than other processes such as baroclinic instability.

BIBLIOGRAPHY

Belcher, S. E., and Coauthors, 2012: A global perspective on Langmuir turbulence in the ocean surface boundary layer. *Geophys. Res. Lett.*, **39**, 1–9, doi:10.1029/2012GL052932. http://doi.wiley.com/10.1029/2012GL052932.

Boccaletti, G., R. Ferrari, and B. Fox-Kemper, 2007: Mixed Layer Instabilities and Restratification. *J. Phys. Oceanogr.*, **37**, 2228–2250, doi:10.1175/JPO3101.1.

Bower, A. S., and T. Rossby, 1989: Evidence of Cross-Frontal Exchange Processes in the Gulf Stream Based on Isopycnal RAFOS Float Data. *J. Phys. Oceanogr.*, **19**, 1177–1190, doi:10.1175/1520-0485(1989)019<1177:EOCFEP>2.0.CO;2.

Bretherton, F. P., R. E. Davis, and C. B. Fandry, 1976: A technique for objective analysis and design of oceanographic experiments applied to MODE-73. *Deep Sea Res. Oceanogr. Abstr.*, **23**, 559–582, doi:10.1016/0011-7471(76)90001-2.

Callies, J., and R. Ferrari, 2013: Interpreting Energy and Tracer Spectra of Upper-Ocean Turbulence in the Submesoscale Range (1–200 km). *J. Phys. Oceanogr.*, **43**, 2456–2474, doi:10.1175/JPO-D-13-063.1. http://journals.ametsoc.org/doi/abs/10.1175/JPO-D-13-063.1.

——, ——, J. M. Klymak, and J. Gula, 2015: Seasonality in submesoscale turbulence. *Nat. Commun.*, **6**, 1–8, doi:10.1038/ncomms7862.

Capet, X., J. C. McWilliams, M. J. Molemaker, and A. F. Shchepetkin, 2008a: Mesoscale to Submesoscale Transition in the California Current System. Part I: Flow Structure, Eddy Flux, and Observational Tests. *J. Phys. Oceanogr.*, **38**, 29–43, doi:10.1175/2007JPO3671.1. http://journals.ametsoc.org/doi/abs/10.1175/2007JPO3671.1.

——, ——, ——, and ——, 2008b: Mesoscale to Submesoscale Transition in the California Current System. Part II: Frontal Processes. *J. Phys. Oceanogr.*, **38**, 44–64, doi:10.1175/2007JPO3672.1. http://journals.ametsoc.org/doi/abs/10.1175/2007JPO3672.1.

Charney, J. G., 1971: Geostrophic turbulence. *J. Atmos. Sci.*, **28**, 1087–1095.

D'Asaro, E., C. Lee, L. Rainville, R. Harcourt, and L. Thomas, 2011: Enhanced Turbulence and Energy Dissipation at Ocean Fronts. *Science (80-.).*, **332**, 318–322, doi:10.1126/science.1201515. http://www.sciencemag.org/cgi/doi/10.1126/science.1201515.

D'Asaro, E. A., 2003: Performance of autonomous Lagrangian floats. *J. Atmos. Ocean. Technol.*, **20**, 896–911, doi:10.1175/1520-0426(2003)020<0896:POALF>2.0.CO;2.

Danabasoglu, G., S. G. Yeager, Y.-O. Kwon, J. J. Tribbia, A. S. Phillips, and J. W. Hurrell, 2012: Variability of the Atlantic Meridional Overturning Circulation in CCSM4. *J. Clim.*, **25**, 5153–5172, doi:10.1175/JCLI-D-11-00463.1. http://journals.ametsoc.org/doi/abs/10.1175/JCLI-D-11-00463.1.

Dunne, J. P., and Coauthors, 2012: GFDL's ESM2 Global Coupled Climate–Carbon Earth System Models. Part I: Physical Formulation and Baseline Simulation Characteristics. *J. Clim.*, **25**, 6646–6665, doi:10.1175/JCLI-D-11-00560.1. http://journals.ametsoc.org/doi/abs/10.1175/JCLI-D-11-00560.1.

Eady, E. T., 1949: Long Waves and Cyclone Waves. *Tellus*, **1**, 33–52, doi:10.3402/tellusa.v1i3.8507. https://www.tandfonline.com/doi/full/10.3402/tellusa.v1i3.8507.

Emerson, S., and C. Stump, 2010: Net biological oxygen production in the ocean-II: Remote in situ measurements of O2and N2in subarctic pacific surface waters. *Deep. Res. Part I Oceanogr. Res. Pap.*, **57**, 1255–1265, doi:10.1016/j.dsr.2010.06.001. http://dx.doi.org/10.1016/j.dsr.2010.06.001.

Ferrari, R., and D. L. Rudnick, 2000: Thermohaline variability in the upper ocean. *J. Geophys. Res.*, **105**, 16857, doi:10.1029/2000JC900057.

——, and C. Wunsch, 2009: Ocean Circulation Kinetic Energy : Reservoirs , Sources , and Sinks. doi:10.1146/annurev.fluid.40.111406.102139.

Fox-Kemper, B., and R. Ferrari, 2008: Parameterization of Mixed Layer Eddies. Part II: Prognosis and Impact. *J. Phys. Oceanogr.*, **38**, 1166–1179, doi:10.1175/2007JPO3788.1. http://journals.ametsoc.org/doi/abs/10.1175/2007JPO3788.1.

——, ——, and R. Hallberg, 2008: Parameterization of Mixed Layer Eddies. Part I: Theory and Diagnosis. *J. Phys. Oceanogr.*, **38**, 1145–1165, doi:10.1175/2007JPO3792.1. http://journals.ametsoc.org/doi/abs/10.1175/2007JPO3792.1.

Fox-Kemper, B., and Coauthors, 2011: Parameterization of mixed layer eddies. III: Implementation and impact in global ocean climate simulations. *Ocean Model.*, **39**, 61–78, doi:10.1016/j.ocemod.2010.09.002.

Gill, A. E., and P. P. Niller, 1973: The theory of the seasonal variability in the ocean. *Deep. Res. Oceanogr. Abstr.*, **20**, 141–177, doi:10.1016/0011-7471(73)90049-1.

Haney, S., and Coauthors, 2012: Hurricane wake restratification rates of one-, two- and three-dimensional processes. *J. Mar. Res.*, **70**, 824–850, doi:10.1357/002224012806770937.

http://openurl.ingenta.com/content/xref?genre=article&issn=0022-2402&volume=70&issue=6&spage=824.

Hosegood, P., M. C. Gregg, and M. H. Alford, 2006: Sub-mesoscale lateral density structure in the oceanic surface mixed layer. *Geophys. Res. Lett.*, **33**, L22604, doi:10.1029/2006GL026797. http://doi.wiley.com/10.1029/2006GL026797 (Accessed January 31, 2015).

Hosegood, P. J., M. C. Gregg, and M. H. Alford, 2008: Restratification of the Surface Mixed Layer with Submesoscale Lateral Density Gradients: Diagnosing the Importance of the Horizontal Dimension. *J. Phys. Oceanogr.*, **38**, 2438–2460, doi:10.1175/2008JPO3843.1. http://journals.ametsoc.org/doi/abs/10.1175/2008JPO3843.1.

Hoskins, B. J., and F. P. Bretherton, 1972: Atmospheric Frontogenesis Models: Mathematical Formulation and Solution. *J. Atmos. Sci.*, **29**, 11–37, doi:10.1175/1520-0469(1972)029<0011:AFMMFA>2.0.CO;2. http://journals.ametsoc.org/doi/abs/10.1175/1520-0469%281972%29029%3C0011%3AAFMMFA%3E2.0.CO%3B2.

Johnson, G. C., S. Schmidtko, and J. M. Lyman, 2012: Relative contributions of temperature and salinity to seasonal mixed layer density changes and horizontal density gradients. *J. Geophys. Res. C Ocean.*, **117**, C04015, doi:10.1029/2011JC007651. http://doi.wiley.com/10.1029/2011JC007651 (Accessed July 11, 2014).

Johnson, L., C. M. Lee, and E. A. D'Asaro, 2016: Global Estimates of Lateral Springtime Restratification. *J. Phys. Oceanogr.*, **46**, 1555–1573, doi:10.1175/JPO-D-15-0163.1. http://journals.ametsoc.org/doi/10.1175/JPO-D-15-0163.1.

Johnston, T. M. S., D. L. Rudnick, and E. Pallàs-Sanz, 2011: Elevated mixing at a front. *J.*

Geophys. Res. Ocean., **116**, 1–14, doi:10.1029/2011JC007192.

Kraus, E. B., and J. S. Turner, 1967: A one-dimensional model of the seasonal thermocline II. The general theory and its consequences. *Tellus*, **19**, 98–106, doi:10.3402/tellusa.v19i1.9753. https://doi.org/10.3402/tellusa.v19i1.9753.

Lapeyre, G., and P. Klein, 2006: Dynamics of the Upper Oceanic Layers in Terms of Surface Quasigeostrophy Theory. *J. Phys. Oceanogr.*, **36**, 165–176.

Large, W. G., J. C. McWilliams, and S. C. Doney, 1994: Oceanic vertical mixing: A review and a model with a nonlocal boundary layer parameterization. *Rev. Geophys.*, **32**, 363.

LeVeque, R. J., 2007: *Finite Difference Methods for Ordinary and Partial Differential Equations, Steady State and Time Dependent Problems*. SIAM, Philadelphia,.

Mahadevan, a., a. Tandon, and R. Ferrari, 2010: Rapid changes in mixed layer stratification driven by submesoscale instabilities and winds. *J. Geophys. Res. C Ocean.*, **115**, C03017, doi:10.1029/2008JC005203. http://doi.wiley.com/10.1029/2008JC005203 (Accessed July 16, 2014).

——, E. D'Asaro, C. Lee, and M. J. Perry, 2012: Eddy-Driven Stratification Initiates North Atlantic Spring Phytoplankton Blooms. *Science (80-.).*, **337**, 54–58.

Marshall, J., A. Adcroft, C. Hill, L. Perelman, and C. Heisey, 1997: A finite-volume, incompressible navier stokes model for, studies of the ocean on parallel computers. *J. Geophys. Res. C Ocean.*, **102**, 5753–5766, doi:10.1029/96JC02775.

Marshall, J. C., and a J. G. Nurser, 1992: Fluid Dynamics of Oceanic Thermocline Ventilation. *J. Phys. Oceanogr.*, **22**, 583–595, doi:10.1175/1520-0485(1992)022<0583:FDOOTV>2.0.CO;2. http://dx.doi.org/10.1175/1520-0485(1992)022%3C0583:FDOOTV%3E2.0.CO%5Cn2.

McDougall, Trevor J. ; Barker, P. M., 2011: *Getting started with TEOS-10 and the Gibbs Seawater (GSW) Oceanographic Toolbox*. 28 pp. http://www.teos-10.org/pubs/Getting_Started.pdf.

McWilliams, J. C., 2016: Submesoscale currents in the ocean. *Proc. R. Soc. A Math. Phys. Eng. Sci.*, **472**, 20160117, doi:10.1098/rspa.2016.0117. http://rspa.royalsocietypublishing.org/lookup/doi/10.1098/rspa.2016.0117.

——, J. Gula, M. J. Molemaker, L. Renault, and A. F. Shchepetkin, 2015: Filament Frontogenesis by Boundary Layer Turbulence. *J. Phys. Oceanogr.*, **45**, 1988–2005, doi:10.1175/JPO-D-14-0211.1. http://journals.ametsoc.org/doi/10.1175/JPO-D-14-0211.1.

Pallàs-Sanz, E., T. M. S. Johnston, and D. L. Rudnick, 2010a: Frontal dynamics in a California Current System shallow front: 2. Mesoscale vertical velocity. *J. Geophys. Res. Ocean.*, **115**, doi:10.1029/2010JC006474.

——, ——, and ——, 2010b: Frontal dynamics in a California Current System shallow front: 1. Frontal processes and tracer structure. *J. Geophys. Res. Ocean.*, **115**, doi:10.1029/2009JC006032.

Pollard, R. T., and R. C. Millard, 1970: Comparison between observed and simulated wind-generated inertial oscillations. *Deep. Res. Oceanogr. Abstr.*, **17**, doi:10.1016/0011-7471(70)90043-4.

Price, J. F., R. a. Weller, and R. Pinkel, 1986: Diurnal cycling: Observations and models of the upper ocean response to diurnal heating, cooling, and wind mixing. *J. Geophys. Res.*, **91**, 8411.

Roemmich, D., S. Riser, R. Davis, and Y. Desaubies, 2004: Autonomous Profiling Floats: Workhorse for Broad-scale Ocean Observations. *Mar. Technol. Soc. J.*, **38**, 21–29, doi:10.4031/002533204787522802.

Rudnick, D. L., 1996: Intensive surveys of the Azores Front: 2. Inferring the geostrophic and vertical velocity fields. *J. Geophys. Res. Ocean.*, **101**, 16291–16303, doi:10.1029/96JC01144. http://link.springer.com/10.1007/s10298-010-0572-7.

——, and R. Ferrari, 1999: Compensation of Horizontal Temperature and Salinity Gradients in the Ocean Mixed Layer. *Science (80-.).*, **283**, 526–529, doi:10.1126/science.283.5401.526. http://www.sciencemag.org/cgi/doi/10.1126/science.283.5401.526 (Accessed July 27, 2014).

Schmidtko, S., G. C. Johnson, and J. M. Lyman, 2012: Monthly Isopycnal/Mixed-layer Ocean Climatology (MIMOC). *J. Geophys. Res. - Ocean.*, 1–44.

Shcherbina, A. Y., M. C. Gregg, M. H. Alford, and R. R. Harcourt, 2009: Characterizing Thermohaline Intrusions in the North Pacific Subtropical Frontal Zone. *J. Phys. Oceanogr.*, **39**, 2735–2756, doi:10.1175/2009JPO4190.1. http://journals.ametsoc.org/doi/abs/10.1175/2010JPO4373.1.

——, E. a. D'Asaro, C. M. Lee, J. M. Klymak, M. J. Molemaker, and J. C. McWilliams, 2013: Statistics of vertical vorticity, divergence, and strain in a developed submesoscale turbulence field. *Geophys. Res. Lett.*, **40**, 4706–4711, doi:10.1002/grl.50919. http://doi.wiley.com/10.1002/grl.50919 (Accessed July 16, 2014).

Stone, P. H., 1966: On Non-Geostrophic Baroclinic Stability. *J. Atmos. Sci.*, **23**, 390–400, doi:10.1175/1520-0469(1966)023<0390:ONGBS>2.0.CO;2. http://journals.ametsoc.org/doi/abs/10.1175/1520-0469%281966%29023%3C0390%3AONGBS%3E2.0.CO%3B2.

Sutherland, G., G. Reverdin, L. Marié, and B. Ward, 2014: Mixed and mixing layer depths in the ocean surface boundary. *Geophys. Res. Lett.*, **41**, 8469–8476, doi:10.1002/2014GL061939.A.

Sverdrup, H., 1953: On conditions for the Vernal Blooming of Phytoplankton. *J. du Cons. Int. pour l'Exploration la Mer*, **18**, 287–295.

Tandon, A., and C. Garrett, 1994: Mixed Layer Restratification Due to a Horizontal Density Gradient. *J. Phys. Oceanogr.*, **24**, 1419–1424, doi:10.1175/1520-0485(1994)024<1419:MLRDTA>2.0.CO;2. http://journals.ametsoc.org/doi/abs/10.1175/1520-0485%281994%29024%3C1419%3AMLRDTA%3E2.0.CO%3B2.

Taylor, J. R., and R. Ferrari, 2010: Buoyancy and Wind-Driven Convection at Mixed Layer Density Fronts. *J. Phys. Oceanogr.*, **40**, 1222–1242, doi:10.1175/2010JPO4365.1. http://journals.ametsoc.org/doi/abs/10.1175/2010JPO4365.1.

Thomas, L., and R. Ferrari, 2008: Friction, Frontogenesis, and the Stratification of the Surface Mixed Layer. *J. Phys. Oceanogr.*, **38**, 2501–2518, doi:10.1175/2008JPO3797.1. http://journals.ametsoc.org/doi/abs/10.1175/2008JPO3797.1.

Thomas, L. N., 2008: Formation of intrathermocline eddies at ocean fronts by wind-driven destruction of potential vorticity. *Dyn. Atmos. Ocean.*, **45**, 252–273, doi:10.1016/j.dynatmoce.2008.02.002.

——, and C. M. Lee, 2005: Intensification of Ocean Fronts by Down-Front Winds. *J. Phys. Oceanogr.*, **35**, 1086–1102.

——, and T. M. Joyce, 2010: Subduction on the Northern and Southern Flanks of the Gulf Stream. *J. Phys. Oceanogr.*, **40**, 429–438, doi:10.1175/2009JPO4187.1. http://journals.ametsoc.org/doi/abs/10.1175/2009JPO4187.1.

Thomas, L. N., A. Tandon, and A. Mahadevan, 2008: Submesoscale Processes and Dynamics. *Ocean Model. an Eddying Regime*, 17–38. http://dx.doi.org/10.1029/177GM04.

Thomas, L. N., J. R. Taylor, E. A. D'Asaro, C. M. Lee, J. M. Klymak, and A. Shcherbina, 2016: Symmetric Instability, Inertial Oscillations, and Turbulence at the Gulf Stream Front. *J. Phys. Oceanogr.*, **46**, 197–217, doi:10.1175/JPO-D-15-0008.1. http://journals.ametsoc.org/doi/10.1175/JPO-D-15-0008.1.

Thompson, A. F., A. Lazar, C. Buckingham, A. C. Naveira Garabato, G. M. Damerell, and K. J. Heywood, 2016: Open-Ocean Submesoscale Motions: A Full Seasonal Cycle of Mixed Layer Instabilities from Gliders. *J. Phys. Oceanogr.*, **46**, 1285–1307, doi:10.1175/JPO-D-15-0170.1. http://journals.ametsoc.org/doi/10.1175/JPO-D-15-0170.1.

Le Traon, P. Y., 1990: A method for optimal analysis of fields with spatially variable mean. *J. Geophys. Res.*, **95**, 13543, doi:10.1029/JC095iC08p13543.

Visbeck, M., 2002: Deep velocity profiling using lowered acoustic Doppler current profilers: Bottom track and inverse solutions. *J. Atmos. Ocean. Technol.*, **19**, 794–807, doi:10.1175/1520-0426(2002)019<0794:DVPULA>2.0.CO;2.

Wenegrat, J. O., and M. J. McPhaden, 2016: Wind, Waves, and Fronts: Frictional Effects in a Generalized Ekman Model*. *J. Phys. Oceanogr.*, **46**, 371–394, doi:10.1175/JPO-D-15-0162.1. http://journals.ametsoc.org/doi/10.1175/JPO-D-15-0162.1.

Van de Wiel, B. J. H., A. F. Moene, G. J. Steeneveld, P. Baas, F. C. Bosveld, and A. A. M. Holtslag, 2010: A Conceptual View on Inertial Oscillations and Nocturnal Low-Level Jets. *J. Atmos. Sci.*, **67**, 2679–2689, doi:10.1175/2010JAS3289.1. http://journals.ametsoc.org/doi/abs/10.1175/2010JAS3289.1.

Worthington, L. V., 1958: The 18° water in the Sargasso Sea. *Deep Sea Res.*, **5**, 297–305, doi:10.1016/0146-6313(58)90026-1.

Young, W. R., 1994: The Subinertial Mixed Layer Approximation. *J. Phys. Oceanogr.*, **24**, 1812–1826, doi:10.1175/1520-0485(1994)024<1812:TSMLA>2.0.CO;2.